Title
Inertial Reorientation for Aerial and Terrestrial Legged Maneuverability

Permalink
https://escholarship.org/uc/item/04v8r0vb

Author
Libby, Thomas Mark

Publication Date
2017

Peer reviewed|Thesis/dissertation

Inertial Reorientation for Aerial and Terrestrial Legged Maneuverability

by

Thomas Mark Libby

A dissertation submitted in partial satisfaction of the
requirements for the degree of
Doctor of Philosophy

in

Engineering - Mechanical Engineering

in the

Graduate Division

of the

University of California, Berkeley

Committee in charge:

Professor S. Shankar Sastry, Chair
Professor Robert J. Full
Professor Dennis K. Lieu

Spring 2017

Inertial Reorientation for Aerial and Terrestrial Legged Maneuverability

Abstract

Inertial Reorientation for Aerial and Terrestrial Legged Maneuverability

by

Thomas Mark Libby

Doctor of Philosophy in Engineering - Mechanical Engineering

University of California, Berkeley

Professor S. Shankar Sastry, Chair

Maneuverability is among the most important aspects of mobility, and perhaps the most challenging. Steady, periodic locomotion affords parsimonious representation by models consisting of relatively simple neural and mechanical oscillators. Embodiment of these oscillators in low degree-of-freedom underactuated legged robots has produced fast, stable running, but has not recapitulated the remarkable locomotor performance of legged animals. The presence of a mobile, highly actuated spine is one feature of natural runners notably missing from both simple models of locomotion and extant high-performance legged machines. This dissertation takes the first steps toward understanding the locomotor function of such “core” actuation in the form of body bending and tail swinging through a set of experiments in animals and robots that quantify the benefits and drawbacks of an active spine in high-agility legged locomotion.

In Chapter 1, we develop a comparative framework for the design of actuated inertial appendages for planar, aerial reorientation. We first introduce the Inertial Reorientation Template, the simplest model of powered inertial reorientation behavior, and leverage its linear dynamics to reveal the design constraints linking a task with the body designs capable of completing it. We then examine three cases of more practicable inertial reorientation morphology – swinging tails, flailing limbs, and spinning wheels – and advance a notion of “anchoring” whereby a judicious choice of physical design in concert with an appropriate control policy yields a system whose closed loop dynamics are sufficiently captured by the template as to permit all further design to take place in its far simpler parameter space. This approach is effective and accurate over the diverse design spaces afforded by existing platforms, enabling performance comparison through the shared task space. We analyze examples from the literature and find advantages to each body type, but conclude that tails provide the highest potential performance for reasonable designs.

In Chapter 2, we bring the discussion back to earth, exploring whether grounded locomotion could benefit from inertial reorientation. We use a prey capture task to induce large, rapid turns in lizards and investigate the interaction between external (legged ground interaction) and internal (inertial body shape change) sources of mobility. We introduce a more detailed, horizontal plane IR tail anchor model and use it to estimate angular momentum during the animals’ maneuvers

and to predict maximum reorientation due to body shape change. We find evidence that powered inertial reorientation actively aids turning, leading to much higher reorientation performance than would be expected from a rigid-bodied animal. Inertial reorientation behavior may serve multiple functions during a large terrestrial turn, providing a dependable source of rotation independent of external ground reaction forces, and reducing the need for braking forces by stabilizing orientation in task space.

In Chapter 3, we examine the wider context of legged planar maneuvering in which the lizards' body flexibility plays a role. We use the same prey capture behavior to probe the potential benefits of the elongate, sprawled-posture body form of lizards in negotiating the task tradeoffs of a combined rotation and translation in the plane. We find evidence supporting the hypothesis that sprawled posture enhances maneuverability by permitting motion and force production in all directions without large postural shifts. We expect high-agility, maximal effort maneuvers to be constrained into stereotypy; instead, we find huge variability in gait and limb forces even as task behavior is relatively consistent. These features of lizard legged maneuverability align well with the inertial reorientation afforded by their elongate flexible bodies to provide incredible robustness to environmental perturbations.

to Dominica

Contents

List of Figures

List of Tables

Acknowledgments

I owe a huge debt to the faculty that have guided me and supported me through this process. Many thanks to my dissertation chair, Shankar Sastry, for welcoming me into his group despite my strong ties to the “wrong” side of campus. I also thank Dennis Lieu for serving on my qualifying exam and dissertation committees and Fai Ma for serving on my qualifying exam committee. Thanks to Oliver O’Reilly for taking an early interest in my career (without your help I may not have been admitted at all!), for serving as my thesis chair, and for his infectious love of dynamics and inspiring dedication to teaching. I am grateful to Mimi Koehl and Robert Dudley, not only for their insightful comments at our weekly seminar, but also for their patience while I kept the many plates of CiBER spinning in concert with my dissertation work. Special thanks to Dan Koditschek for leading our wonderful Berkeley-Penn collaboration, which culminated in the work that makes up Chapter 1. I have recently enjoyed many hours of exciting conversation and mentorship by Max Donelan – I look forward to returning to our collaboration now that this dissertation is done! Most of all, I offer my deepest gratitude to Bob Full. I was fantastically lucky to stumble upon IB32 and subsequently join your lab during my undergrad, and can honestly say it changed my life. Thank you for your committed mentorship and vision, I never would have done this without you.

My path toward this degree has been long and convoluted, but all the richer for it. Working as the technical director of the Center for Interdisciplinary Bio-inspiration in Education and Research in the years prior to my doctoral experience gave me the opportunity to meet and collaborate with several generations of exceptional students and postdocs. In particular, I want to acknowledge Kenneth Meijer, for getting me started in the lab many years ago during my first undergraduate research experience, and Noah Cowan, for his early mentorship and for planting the seed of the grad school idea in my mind. Thanks to Simon Sponberg and Jenny McGuire, for welcoming me (and Dominica!) into your home many times, and for your friendship and wisdom. I am particularly grateful to Aaron Johnson, for the rewarding collaboration that became the first chapter of this dissertation. Special thanks to Sam Burden, my former labmate and future postdoc adviser, for helping arrange the next step in this great adventure. Thanks so much to Kaushik Jayaram, Nate Hunt, Shai Revzen, Talia Moore, Jean-Michel Mongeau, Ardian Jusufi, Chris Dallmann, Judy Jinn, Zhongyuan Wang, Duncan Haldane, Erin Brandt, and Leeann Louis, for the many years of exciting discussion and camaraderie that made this experience infinitely more pleasurable. Last but not least, thanks to Evan Chang-Siu, for a fruitful collaboration spanning half a dozen papers and substantial contributions to the ideas in this dissertation, but more importantly for his big-hearted friendship.

I was fortunate to have funding support throughout my doctorate studies, thanks to the National Science Foundation and the Army Research Lab. I also benefited greatly from Berkeley’s wonderful campus community. The work in this dissertation would not have come together without the dedicated assistance of many fantastic undergraduate researchers and visiting scholars. Viktor Gudenus, whose development effort on the morphometric models of Chapter 2 and early experimentation was a critical contribution to the turning work. Sander Dobbenga, whose insightful brainstorming helped generate the ideas of Chapter 3. Thanks to Debbie Li, Katherine Wu, Joshua

Levy, M.J. Koh, Michael Hwang, Roshena MacPherson, and Seth Bergenholtz for their many hours of data collection and analysis.

None of this would have been possible without the love and support I draw from my family. My mother, who passed before I began my graduate studies, nevertheless has been an enduring source of strength and love. Her support and encouragement (and many hours spent at the library during the summers of my youth) fostered my life-long love of science (and of animals in particular). My father's spirit of adventure, mad "science," natural technical prowess, intellectual curiosity, and oddball sense of humor have inspired and enriched me since I was a child. My siblings, Erica and David, despite suffering me all their lives, continue to extend their friendship and sometimes let me beat them at Mario Kart. Molly has been warmly encouraging and has (mostly) kept Dad in one piece.

Most of all, my deepest appreciation to the love of my life, my best friend, my wife, Dominica. You've been the center of my universe for almost half my life now, and I cannot imagine who I would be without your wisdom, compassion, and affection. I dedicate this dissertation to you.

Chapter 1

Comparative Design for Inertial Reorientation

1.1 Publication information

The work presented in this chapter is reprinted, with permission, from Libby, T., Johnson, A.M., Chang-Siu, E., Full, R.J. and Koditschek, D.E., 2016. Comparative Design, Scaling, and Control of Appendages for Inertial Reorientation. IEEE Transactions on Robotics, September, 2016. © 2016 IEEE [5].

1.2 Introduction

Tails and tail-like appendages have shown promise to greatly enhance robot agility, enabling such feats as aerial reorientation [2, 6, 7], hairpin turns [8–10], and disturbance rejection [11–13]. These behaviors are examples of *Inertial Reorientation* (or *IR*), whereby internal configuration adjustments generate inertial forces that control the body's orientation. The stabilizing function of inertial appendages appears to be important to animals across a wide variety of behaviors and size scales, suggesting that this mechanism could be broadly useful for robotic systems such as the small, wheeled Tailbot [2], Fig. 1.1(a), or the larger, legged RHex [3, 4], Fig. 1.1(b). While tails may be the most conspicuous example of IR morphology, any internal movement of mass can induce rotation in a body. Animals also use the inertia of their legs [14, 15], wings [16], or spine [17] to accomplish similar behaviors, and engineered systems use radially symmetric wheels inside satellites or on terrestrial vehicles [18].

This paper presents a formal framework for the selection and comparison of robot bodies capable of a planar, aerial, inertial reorientation task. Design of morphology for a dynamic behavior like IR is a persistently challenging problem in robotics, since task completion must be enforced over the full design space through the execution of a hybrid and possibly nonlinear dynamical system. We propose a reductionist approach, collapsing the complexity of the variously possible body

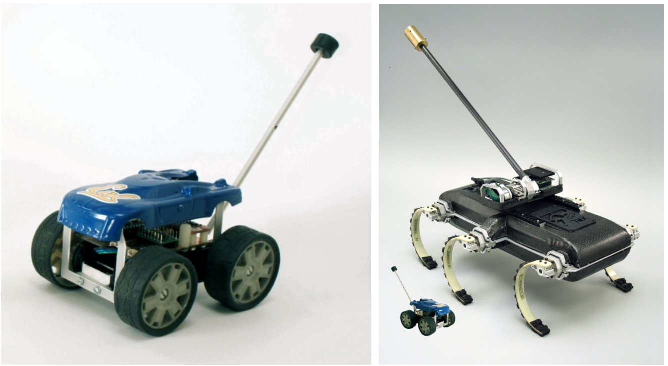
(a) (b)

Figure 1.1: (a) Tailbot [1, 2] (b) RHex [3, 4] with a new tail, and with approximately sized image of Tailbot inserted.

plans to a far simpler model whose dynamics we can solve. The task-feasible set of this simple model, together with its generic controller, is then pulled back through this "morphological reduction" to specify the more complex design. We use this framework to evaluate the merits of a range of possible morphologies, and to design a new tail for the RHex robot, Fig. 1.1(b), documenting its efficacy for recovery from otherwise injurious falls as illustrated in Figs. 1.7 and 1.9.

1.2.1 Prior Work

The study of inertial reorientation dates to the 19th century "falling cat problem" [17]. More recent studies show that by swinging their tails, lizards can self-right in less than a body length [19], reorient through zero net angular momentum IR maneuvers [20], and control their attitude in leaps [1]. To the authors' best knowledge, the first robot to utilize an inertial tail is the Uniroo, a one leg hopper that stabilized its body pitch in part with an actuated tail [21]. Other early robotic tails were passive or slowly actuated and used to maintain contact forces while climbing vertical surfaces [22, 23]. The idea of using a robot's existing limbs as tail-like appendages was first explored as a method of "legless locomotion" [24].

The effectiveness of the IR capabilities in lizards inspired the creation of Tailbot, Fig. 1.1(a), a robot with an active tail which enabled disturbance regulation [1], air-righting, and traversing rough terrain [2]. Since Tailbot, there has been an explosion in the number of robotic tails for reorientation [7–10, 25] and stabilization [11–13, 26, 27] in both aerial and terrestrial domains. Non-inertial tails have also seen continued interest with tails that affect the body through substrate interaction [28–30] and aerodynamics [31, 32]. Recently, other morphologies have also been explored including two degree of freedom tails that greatly expand the range of possible motions [13, 26, 33] and flailing limbs that reuse existing appendages [34]. Many of these robots draw their inspiration from a diverse variety of animals, including moths [25, 35], seahorses [36], kangaroos [13], cheetahs [10, 11, 27], and even dinosaurs [1, 37]. The growing interest in robotic IR appendages demonstrates the potential benefits of inertial forces and motivates the need for truly comparative design methodologies.

1.2.2 Paper Outline and Contributions

To instantiate the appendage design problem, in this work we consider an aerial IR self-righting task. For whereas while the machines examined in this paper are nominally terrestrial locomotors, their rapid, dynamic behavior includes leaps, falls, and other short aerial phases where their limbs cannot provide control authority through ground reaction forces. We will restrict motion in both the templates and anchors to a 2D plane, in the absence of external forces. The task is defined as a finite-time, zero angular momentum reorientation: a rotation of the body configuration θ_b from initial condition $\theta_b(0) = \dot{\theta}_b(0) = 0$, to rest at some final angle $\theta_{b,f}$ in a desired time t_f. That is,

$$\theta_b(t_f) - \theta_{b,f} = 0; \qquad \dot{\theta}_b(t_f) = 0. \tag{1.1}$$

Because any internal motion – whether a rotation of tails, wheels, limbs, or even body bending – must yield some inertial reorientation in flight, we need a method of directly comparing the performance and design merits of a diverse array of potential body structures. The simplicity of the shared underlying behavior is suggestive of a *template* [38], or simplest model, whose tractable dynamics yield a compact description of the relationship between morphology and task performance. We present the IR template (Section 1.3.1) and solve its simple dynamics (Section 1.3.2) relative to the task (1.1) (Section 1.3.3), revealing the constraints linking that task with the set of body designs capable of completing it. We then refine that set by reducing it to the instances where the control and gearing are optimal for the assigned task (Section 1.3.4).

The embodiment of this simple template in a more complex model of real morphology (an *anchor*, [38])[1] provides for a shared parametrization of IR efficacy. This is a new idea that enables the design and direct comparison of different candidate bodies through a generalized template–anchor relationship that we now briefly describe intuitively before charting its technical development in this paper and in Appendix 1.9.1. Whereas in this problem the template degrees of freedom typically embed naturally into those of the morphologies, the same is not true of their respective design parameters. Thus, our agenda of reusably "anchoring" a template design in a variety of bodies requires a new mapping between their parameter spaces. Beyond the specifics of the task, one of the central contributions of this paper is to articulate and formalize the role of this morphological reduction. As we detail in Section 1.4, mapping the design parameters (mass, length, and inertia, etc) of a detailed model down to the simpler template parameters, carries a pullback of the simple template controller back up to the anchor as well.

We define anchor models for tails (Section 1.4.1), reaction wheels (Section 1.4.2), and synchronized groups of limbs (hereafter termed "flails", Section 1.4.3), and propose morphological

---

[1] Here, there is no time-asymptotic specification, and therefore no attracting invariant set as achieved empirically, e.g. in [3, 39], and formally as well, e.g. in [40]. Instead, we observe that the anchors manifest a close approximation to the template over large, interesting regions of parameter spaces, Appendix 1.9.1.

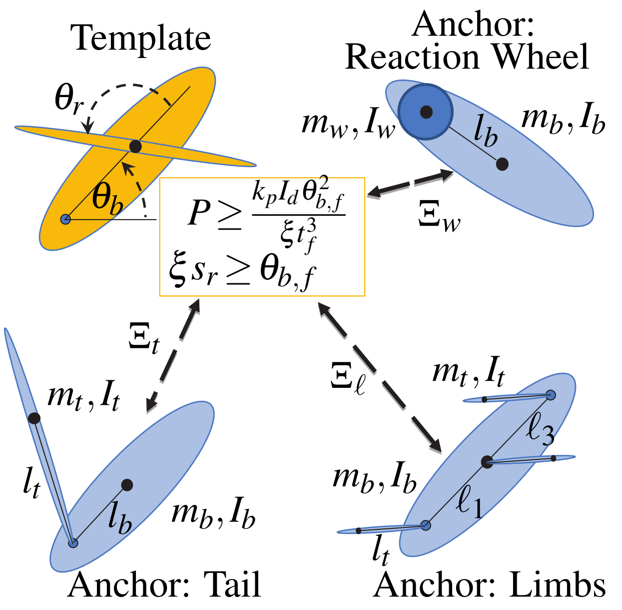

Figure 1.2: The Inertial Reorientation Template is a planar, two-link model parametrized in part by Power, P, Effectiveness, ξ, Appendage Stroke, s_r, and Driven Inertia, I_d; designs satisfying the constraints are feasible with respect to the task, (1.1). More complex IR bodies (anchors) may be designed or compared through the template by mapping their physical parameters to those of the template, using a Morphological Reduction, Ξ_i, as summarized in Table 1.2.

reductions from their respective parameter spaces to the parameter space of the template (summarized in Fig. 1.2 and Table 1.2). We use these morphological reductions to find evidence of similar template–anchor relationships in design examples from a dozen different platforms (Section 1.5.1), which exhibit close (or in some cases exact) kinematic and dynamic approximations (depicted in Fig. 1.5). The reductions afford a performance comparison of each morphology (Section 1.5.2), and a more general comparative scaling analysis (Section 1.5.3).

We assess anecdotally the utility of our design framework in three ways. First, we use our design specification to analyze the tail added to a RHex hexapedal robot [3] (specifically X-RHex Lite, XRL [4], Fig. 1.1(b) and Section 1.6.1). Second, we use the common IR template to compare the RHex tailed-body instantiation with a limbed-body instantiation using only RHex's legs (Section 1.6.1). Finally, we present empirical results (Section 1.6.2) that illustrate the manner in which IR behaviors can help robots perform high-performance, potentially injurious aerial reorientation using inertial limbs.

In the interest of space and clarity, we have omitted the more lengthy derivations required to reach some expressions in this paper; the full derivations can be found in the accompanying technical report, [41].

1.3 Template Behavior

This section develops the simplest Inertial Reorientation (IR) model and solves its dynamics explicitly in the context of the task specification. From this, we derive two constraints specifying the feasible portion of parameter space over which the robot design may be optimized (or – more practicably – "toleranced," as we exemplify in Section V) to best meet performance needs outside the reorientation task. To this end, we define the IR template (depicted in Fig. 1.2) as a planar system comprised of two rigid bodies – an "appendage" and a "body" pinned at their shared centers of mass (COMs). A motor applies a torque acting on θ_r, the internal angle between the bodies, and can steer θ_b, the orientation of the body, through the action of a controller. We will thus choose (θ_r, θ_b) as our generalized coordinates. The appendage moment of inertia (MOI), I_a and the template body MOI, I_d, specify the passive mechanics.

The template's behavior during the reorientation task is fully parametrized by a combination of its physical (body) parameters, powertrain and control parameters, and its task specification, defined throughout the rest of this section and summarized in Table 1.1 as,

$$\mathbf{p} = [\xi, I_d, s_r, P, \omega_m, t_s, \theta_{b,f}, t_f] \in \mathscr{P}. \tag{1.2}$$

Not all parameter sets $\mathbf{p}$ are self-consistent, as clearly only certain bodies are capable of completing a given task. The remainder of this section will be dedicated to finding a parametrization of the constraints defining the feasible subset of parameters, $\mathscr{R} \subset \mathscr{P}$. Any parameter set in $\mathscr{R}$ is "taskworthy" in the sense that its physical parameters enable completion of its task description. The "task-worthy" set will be used to solve two design problems:

P1 *Body Selection*: The task specification is fixed at the outset and the other parameters are chosen to satisfy its completion.

P2 *Performance Evaluation*: The physical parameters are fixed and a given t_f and $\theta_{b,f}$ are queried against a resulting feasible set.

We next derive the kinematics and dynamics of this IR template model, and then solve those dynamics in normalized form to reveal the feasible set $\mathscr{R}$.

1.3.1 Template Kinematics

For a planar, single degree of freedom IR system in free fall, the rotation available in the body's workspace is limited by the capacity for internal motion. To derive a functional relationship between the (internal) shape angular velocity and the (external) body orientation velocity, we will use the non-holonomic constraint resulting from conservation of the system's total angular momentum. From any point O, Euler's laws for a rigid body state that $\dot{\mathbf{H}}_\mathbf{O} = \mathbf{M}_\mathbf{O}$, where $\mathbf{H}_O$ is the total angular momentum about O, and $\mathbf{M}_\mathbf{O}$ is the net moment about O. For short aerial behaviors in robots larger than a few grams, we will assume that the external forces and torques (particularly aerodynamic torques) are negligible so that $\mathbf{M}_\mathbf{O} = 0$, and hence total angular momentum about O is conserved.

The template's angular momentum about the perpendicular axis ($\mathbf{E}_3$) of its COM,

$$H_O = (I_a + I_d)\dot{\theta}_b + I_a\dot{\theta}_r, \tag{1.3}$$

where $H_O\mathbf{E}_3 := \mathbf{H}_O$ and $\dot{\theta}_b$ and $\dot{\theta}_r$ are derivatives with respect to time t. Normalizing by the total MOI, $I_a + I_d$, and solving for body angular velocity reveals that the template kinematics are parametrized by a single dimensionless constant ξ, the *effectiveness* of the IR template[2],

$$\dot{\theta}_b = \widetilde{H}_O - \xi\dot{\theta}_r, \qquad \xi := \frac{I_a}{I_a + I_d}, \tag{1.4}$$

where $\widetilde{H}_O$ is the normalized system angular momentum. Hence the angular velocity of the body can be decomposed into two physically interesting components: a drift term influenced solely by external impulses, and the velocity induced by internal shape change that has been called the *local connection vector field* [42] (hereafter *connection field*, although note that in this transient setting there is no cyclic shape change). This equation directly governs performance in two distinct tasks: 1) orientation regulation after an impulse, where the task is to maintain a stable body angle ($\dot{\theta}_b = 0$), with a relative velocity $\dot{\theta}_r = \widetilde{H}_O/\xi$; and 2) zero angular momentum reorientation ($H_O = 0$), where the task is to change the body orientation to some angle $\theta_{b,f}$ in t_f seconds, (1.1), given the constraint of the connection field, $\dot{\theta}_b = -\xi\dot{\theta}_r$.

In the latter case, body rotation is directly a function of appendage rotation. Under the assumption that $\dot{\theta}_r$ is positive,

$$\dot{\theta}_b = \frac{d\theta_b}{dt} = \frac{\partial\theta_b}{\partial\theta_r}\frac{d\theta_r}{dt} = -\xi\dot{\theta}_r, \qquad \frac{\partial\theta_b}{\partial\theta_r} = -\xi, \tag{1.5}$$

expressing the 1-dimensional connection field that reveals the constant differential relationship between internal and external rotation.[3] For this template, the connection field is constant and equal to $-\xi$. The body stroke is directly proportional to appendage stroke, and hence a limit s_r on the range of motion of the appendage will limit the achievable body rotation.

1.3.2 Template Dynamics

A real terrestrial robot is constrained by the duration of its aerial phase (fall, leap, or other dynamic behavior) and this imposes a new set of requirements on the parameters that specify the actuation. This section characterizes the behavior of a conventionally power-limited actuation scheme, and defines a controller for that actuator.

---

[2] Note that this quantity differs from that of [6], wherein effectiveness ε was defined as the ratio of link velocities.

[3] In the anchor models this relationship may be nonlinear or non-monotonic.

Newtonian and Actuator Dynamics

As the template consists of two rigid bodies pinned through their concentric COMs, derivation of the equations of motion is trivial – the angular acceleration of body and tail are opposite in sign and equal to the motor torque normalized by each body's MOI. Since the tail angle is kinematically related to that of the body by (1.5), we will simply consider the body dynamics,

$$\ddot{\theta}_b = \frac{\tau}{I_d}, \tag{1.6}$$

where τ is the motor torque. The ratio of joint torque to body angular acceleration is equal to the body's MOI in the template, I_d, but is more complex in the anchors (coupling appendage masses, etc.); to avoid confusion with the inertia of the physical body segment in the anchor models, we will call this ratio the "driven" inertia.

To capture the essential limitation of any powertrain in a time-sensitive task – the rate at which it can change the mechanical energy of the driven system – we augment the template's dynamics with a simple, piecewise-linear actuator model in which torque falls linearly with increasing speed (we extend this to allow for current limits in Appendix 1.9.3). This model is not only a good approximation of a DC motor [43], but is general enough to capture to first order the effort-flow relationships of many other speed-dependent actuators including biological muscles [44]. The maximum available actuator torque depends on activation (terminal voltage, $V = \pm V_m$, for some maximum voltage V_m) and speed,

$$\tau(V, \dot{\theta}_r) = \begin{cases} \operatorname{sgn}(V)\ \tau_m \left(1 - \frac{|\dot{\theta}_r|}{\omega_m}\right) & : V\dot{\theta}_r < 0 \\ \operatorname{sgn}(V)\ \tau_m & : V\dot{\theta}_r \geq 0 \end{cases} \tag{1.7}$$

where τ_m is the stall torque and ω_m is the no-load speed of the motor after the gearbox (and hence the no-load speed of the appendage relative to the body).

Since we seek to specify the entire powertrain, we find it convenient to decouple the roles of the actuator and the transmission by parametrization with respect to peak mechanical power, $P = \tau_m \omega_m / 4$, (whose product form cancels the appearance of the gear ratio) and drivetrain no-load speed, ω_m (whose linear dependence upon the gear ratio makes it a useful surrogate for the transmission). The required gear ratio of a physical gearbox or other transmission is then the ratio of ω_m to the motor's actual no-load speed.

Controller Design

Notwithstanding the voluminous literature on time optimal control in mechatronics and robotics settings (e.g., along specified paths [45], and exposing actuator dynamics [46]) we have not been able to find a formal treatment of the robust minimum time problem for our simple hybrid motor model (1.7). Therefore we will take the naïve approach and embrace a single switch open loop bang-bang controller as offering the simplest and most paradigmatic expression of "fast repositioning" for a (back-EMF perturbed) double integrator [47]. We relax the bang-bang controller assumption in Appendix 1.9.2 and in particular show that a proportional-derivative (PD) feedback controller closely and robustly approximates (and given high enough gains, converges to) the open loop control policy. We further verify this in the empirical results, Section 1.6.2, which use a PD controller to approximate the bang-bang controller.

The bang-bang control strategy makes a single switch between the acceleration and braking dynamics at a time t_s, such that the body comes to a halt at the desired final orientation $\theta_{b,f}$. [4] During the single-switch reorientation from $\theta_b = 0$, the body will accelerate from rest and brake to the final angle $\theta_b = \theta_{b,f}$ with no overshoot, with $\dot{\theta}_b \geq 0$ and $\dot{\theta}_r \leq 0$ for the entire maneuver. Using (1.5), the torque can be rewritten to eliminate the dependence on θ_r. The hybrid dynamics are described by an acceleration phase and a braking phase,

$$\ddot{\theta}_b = \begin{cases} \frac{4P}{\omega_m I_d}\left(1 - \frac{\dot{\theta}_b}{\xi \omega_m}\right), & \text{for } 0 \leq t < t_s, \\ -\frac{4P}{\omega_m I_d}, & \text{for } t \geq t_s. \end{cases} \tag{1.8}$$

Behavior in reorientation task

Based on this template kinematics, dynamics, and controller structure, we now examine the resulting behavior of the system in this reorientation task. First, note that due to local integrability of the non-holonomic constraint, (1.5), the system has only a single degree of freedom after the initial conditions are chosen. We therefore choose to define the initial conditions as $\theta_r = \theta_b := 0$, and express the dynamics only in terms of θ_b. The system starts at rest, so that $\dot{\theta}_b = 0$. We can write the system behavior in closed form by integrating the linear, switched dynamics in (1.8) from this initial condition until the body again comes to a halt at a time t_h. See Appendix 1.9.4 for details on this integration. The halting time can be written as an explicit function of the template parameters, (1.2),

$$t_h = g_h(\mathbf{p}) := t_s + \frac{I_d \xi \omega_m^2}{4P}\left(1 - \exp\left(-\frac{4P}{I_d \xi \omega_m^2} t_s\right)\right), \tag{1.9}$$

along with the final angle, $\theta_b = \theta_h$,

$$\theta_h = g_\theta(\mathbf{p}) := \xi \omega_m t_s - \frac{I_d \xi^2 \omega_m^3}{8P}\left(1 - \exp\left(-\frac{8P}{I_d \xi \omega_m^2} t_s\right)\right). \tag{1.10}$$

1.3.3 Dynamical Task Encoding

The physical relationships derived in the previous two sections enable a straightforward representation of the task-feasible parameter subset $\mathscr{R}$ containing all self-consistent parameter sets. This restricted set can be written as a system of constraints to facilitate the two design problems identified at the beginning of this section: P1 *Body Selection*, in which the task specification (t_f and

---

[4] This may be replaced by an event-based guard condition $G(\theta_b, \dot{\theta}_b) = 0$, as derived in Appendix 1.9.7.

$\theta_{b,f}$) is fixed at the outset and $\mathscr{R}$ prescribes the corresponding feasible body designs, and P2 *Performance Evaluation*, where the achievable task set is identified, given a fixed body design (values of ξ, I_d, P, ω_m, s_r, and t_s).

The first constraint arises from the kinematic relation, (1.5), and ensures that the rotation by the task, $\theta_{b,f}$ falls within any physical constraints on rotation. If the design has a finite range of motion s_r (so that $\theta_r \in [0, s_r]$), then any design meeting the task specification (1.1) must satisfy,

$$\xi s_r \geq \theta_{b,f}; \tag{1.11}$$

obviously bodies with unlimited range of motion satisfy this constraint trivially. The second constraint ensures that the halting time, (1.9), falls within the task completion time, t_f. The third constraint ensures that the body, under the bang-bang controller (parametrized by t_s), (1.10), stops at the correct angle. Taken together, these constraints define $\mathscr{R}$,

$$\mathscr{R} := \left\{ \mathbf{p} \in \mathscr{P} \,\middle|\, \xi s_r \geq \theta_{b,f}, t_f \geq g_h(\mathbf{p}),\, \theta_{b,f} = g_\theta(\mathbf{p}) \right\}. \tag{1.12}$$

For the *Body Selection* problem, P1, any design, $\mathbf{p} \in \mathscr{R}$, satisfying these constraints is “task-worthy” in that its physical and controller parameters satisfy its task specification. The *Performance Evaluation* problem, P2, is also easily specified using this representation: fixing all parameters save t_f and $\theta_{b,f}$ specifies a two-dimensional subspace of achievable tasks (see Fig. 1.6 for a graphical example).[5]

Unfortunately, $\mathscr{R}$ still leaves many degrees of freedom for task-worthy designs for the *Body Selection* design problem. In the remainder of this section, we show that the gearing and control parameters (ω_m and t_s, respectively) can be eliminated through optimization, thereby enabling a more compact and considerably more prescriptive set.

Spatiotemporally-normalized template behavior

The isolation of the effect of gearing and control on $\mathscr{R}$ is complicated by their nonlinear interaction with the other dimensioned parameters in $\mathbf{p}$. To remove the effect of scale and expose these relationships, we will nondimensionalize the equations (1.9) and (1.10), seeking a spatiotemporal rescaling[6] parametrized by γ, such that,

$$\tilde{t}_s = \gamma t_s; \quad \tilde{t}_f = \gamma t_f; \quad \tilde{t}_h = \gamma t_h; \quad \tilde{\theta}_h = \frac{\theta_h}{\theta_{b,f}}. \tag{1.13}$$

where the $\tilde{\cdot}$ indicates dimensionless values. We find that choosing,

$$\gamma := \left(\frac{4P\xi}{I_d \theta_{b,f}^2} \right)^{\frac{1}{3}}, \tag{1.14}$$

---

[5] The largest task set will be found by allowing the switching time to vary with the task (i.e., using the third constraint in (1.12) to select t_s for each $\theta_{b,f}$.)

[6] This rescaling can also be seen as a nondimensionalization of the template dynamics resulting in a normalized hybrid system that simplifies the integration of the dynamics; see Appendix 1.9.4.

enables a particularly convenient reduction of g_h and g_θ, (1.9)–(1.10), written as a function of only two normalized parameters,

$$\tilde{t}_h = \tilde{g}_h(\tilde{\omega}_m, \tilde{t}_s) := \tilde{t}_s + \tilde{\omega}_m^2 \left(1 - \exp\left(\frac{-\tilde{t}_s}{\tilde{\omega}_m^2}\right)\right) \tag{1.15}$$

$$\tilde{\theta}_h = \tilde{g}_\theta(\tilde{\omega}_m, \tilde{t}_s) := \tilde{\omega}_m \tilde{t}_s - \frac{\tilde{\omega}_m^3}{2}\left(1 - \exp\left(\frac{-2\tilde{t}_s}{\tilde{\omega}_m^2}\right)\right), \tag{1.16}$$

where $\tilde{\omega}_m$ is a dimensionless actuator parameter that stands as a proxy for gearing,

$$\tilde{\omega}_m := \frac{\xi \omega_m}{\gamma \theta_{b,f}}. \tag{1.17}$$

In the rescaled coordinates, the reorientation task requires that the system halt at $\tilde{\theta}_h = 1$, constraining the normalized parameters to one degree of freedom. This freedom can be parametrized by $\tilde{\omega}_m$ through the implicit function specifying the “critical” switching time $\tilde{t}_c$, satisfying $\tilde{g}_\theta(\tilde{t}_s, \tilde{w}_m) = 1$ for a given choice of no-load speed,

$$\tilde{t}_c = \tilde{g}_c(\tilde{\omega}_m) := \inf\{\tilde{t}_s > 0 \mid \tilde{g}_\theta(\tilde{t}_s, \tilde{\omega}_m) = 1\}. \tag{1.18}$$

When the other system parameters are chosen, the designer can choose the controller that completes the task by setting

$$t_s = \gamma \tilde{g}_c\left(\frac{\xi \omega_m}{\gamma \theta_{b,f}}\right), \tag{1.19}$$

automatically satisfying (and therefore obviating the need for) the third constraint in (1.12). With this choice, the scaled halting time depends only on the scaled no-load speed,

$$\tilde{t}_h = \tilde{g}_h(\tilde{\omega}_m, \tilde{g}_c(\tilde{\omega}_m)). \tag{1.20}$$

The second constraint in (1.12) can now be written in a more useful form. The temporal demands of the task require that full template parameters, (1.2), be chosen so that the spatiotemporal rescaling meets the task specification. In particular, the value of γ, (1.14) (chosen through the selection of physical parameters) must ensure that the physical halting time meets the constraint,

$$t_f \geq t_h = \frac{1}{\gamma}\tilde{t}_h = \frac{1}{\gamma}\tilde{g}_h(\tilde{\omega}_m, \tilde{g}_c(\tilde{\omega}_m)). \tag{1.21}$$

Substituting the definition of γ and rearranging terms yields a more compact version of the time constraint in (1.12), predicated on critical switching time,

$$\frac{\xi P}{I_d} \geq k_p \frac{\theta_{b,f}^2}{t_f^3}, \tag{1.22}$$

where k_p is a function of dimensionless gear ratio defined as,

$$k_p := \frac{1}{4}\tilde{g}_h^3\left(\frac{\xi\,\omega_m}{\gamma\theta_{b,f}}, \tilde{g}_c\left(\frac{\xi\,\omega_m}{\gamma\theta_{b,f}}\right)\right). \tag{1.23}$$

For a fixed task specification with a given inertia, power and effectiveness trade off directly. The value of k_p increases the requirements on P and ξ, and thus k_p may be considered a performance "cost" imposed by suboptimal gearing. We will consider this cost when selecting an actuator design for RHex in Section 1.6.

Optimal Control and Gearing for the Template

The gearing that maximizes performance in the critically-switched task minimizes k_p, or equivalently, the dimensionless completion time t_h,

$$\underset{\tilde{\omega}_m}{\text{minimize}} \quad \tilde{t}_h = \tilde{g}_h(\tilde{\omega}_m, \tilde{g}_c(\tilde{\omega}_m)). \tag{1.24}$$

This problem has a (numerically determined) unique global minimum at,

$$\tilde{\omega}_m^* \approx 0.74, \tag{1.25}$$

corresponding to a minimal final dimensionless time, $\tilde{t}_h^* := \tilde{g}_h(\tilde{g}_c(\tilde{\omega}_m^*), \tilde{\omega}_m^*) \approx 2.14$ (Fig. 1.3, top). With this optimal $\tilde{\omega}_m^*$ we can find the minimal $k_p^* := \tilde{g}_h^3(\tilde{\omega}_m^*, \tilde{g}_c(\tilde{\omega}_m^*))/4 \approx 2.46$, corresponding to the minimal power requirement for (1.22). Similarly, the critical switching time at this optimum, (1.18), is a constant $k_t^* := \tilde{g}_c(\omega_m^*) \approx 1.62$. Finally, the optimal dimensioned no-load speed, ω_m, can be found from equations (1.21) and (1.17), $\omega_m = k_s\theta_{b,f}/\xi t_f$, for $k_s := \tilde{\omega}_m\,\tilde{g}_h(\tilde{\omega}_m, \tilde{g}_c(\tilde{\omega}_m))$ (where with these optimal values, $k_s^* \approx 1.58$).

This optimal bang-bang control can be expressed via the ratio $\tilde{t}_s/\tilde{t}_h$ (Fig. 1.3, bottom); the optimized maneuver consists of full positive voltage for 76% of the total time, followed by full negative voltage until the body comes to a halt (Fig. 1.4).

The designer seeking the optimally-geared body for a critically-switched reorientation task can then consider a refinement to $\mathscr{R}$, (1.12), that explicitly slaves two of the parameters (ω_m and t_s) to the others,

$$\mathscr{R}^* := \left\{\mathbf{p} \in \mathscr{P} \,\middle|\, \xi s_r \geq \theta_{b,f}, \quad \frac{\xi P}{I_d} \geq \frac{k_p^*\theta_{b,f}^2}{t_f^3}, \right. \tag{1.26}$$

$$\left. \omega_m = k_s^*\frac{\theta_{b,f}}{\xi t_f}, \quad t_s = k_t^*\left(\frac{4P\xi}{I_d\theta_{b,f}^2}\right)^{\frac{1}{3}} \right\}.$$

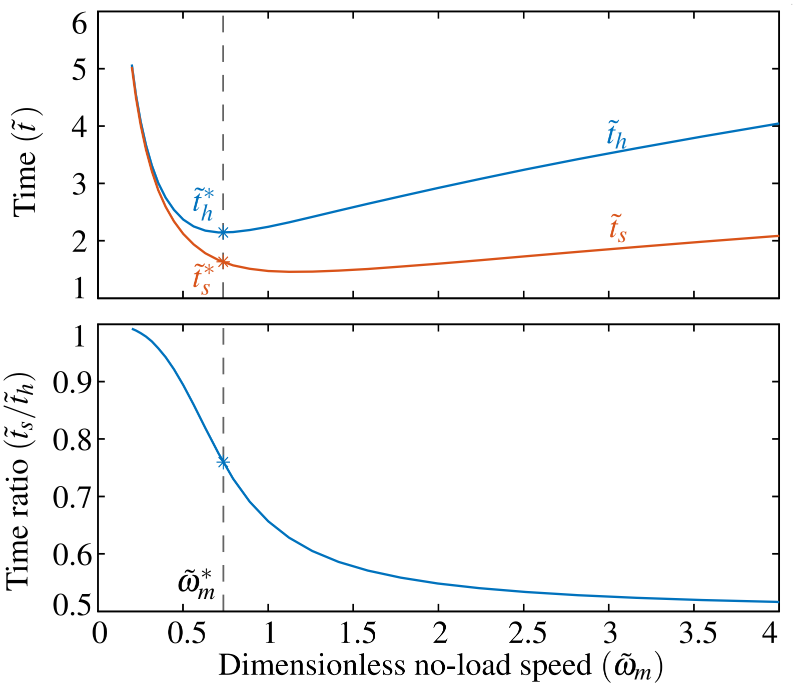

Figure 1.3: Dimensionless system dynamics. Final time is globally minimized by $\tilde{\omega}_m \approx 0.74$ (top). Bang-bang control depends on $\tilde{\omega}_m$; at minimum final time, voltage switches at $\approx 76\%$ of final time.

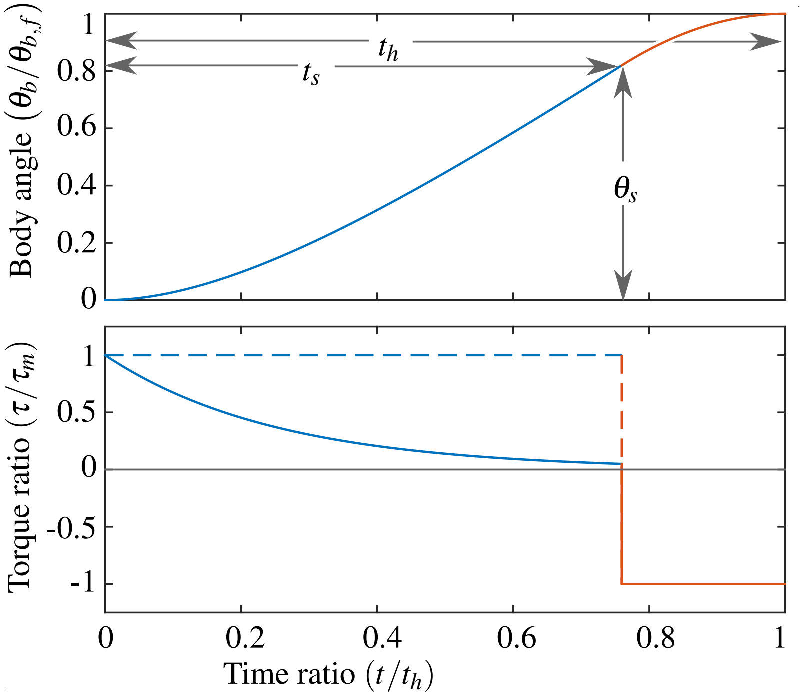

Figure 1.4: System kinematics (top). Bang-bang control for optimal gearing (bottom) selects maximal forward input (dashed line) for 76% of final time, then switches to full reverse; actual torque (solid line) is limited by back-EMF during acceleration (blue) and current during braking (red).

1.3.4 Summary of template design freedom

The solution of the template's kinematics and dynamics enabled two representations of the task-feasible subset of design parameters, each serving a particular role in the two design problems specified at the beginning of this section. Starting with a fixed task specification (t_s and $\theta_{b,f}$), the *Body Selection* problem, P1, can be summarized as a choice of the body parameters (ξ, I_d, s_r, and P) subject to the set constraint $\mathscr{R}^*$, (1.26), with the control and gearing (ω_m and t_s) selected optimally based on this design. Alternatively, given an existing (or putative) design, the set $\mathscr{R}$, (1.12), can be used in a *Performance Evaluation* problem, P2, specifying the achievable tasks. In this latter case, the "cost" of suboptimality can be computed using k_p, (1.23), or by finding an empirical k_p by substituting the template parameters into (1.22).[7]

---

[7] A submaximal limit on torque, or suboptimal controllers like the PD scheme discussed earlier, also manifest as an increase in k_p.

1.4 Anchoring via Morphological Reduction

The concentrically-pinned appendage of the template is not likely to exactly model practical physical designs, raising the question of how the template parametrization relates to real bodies available to a robot designer. We now explore how the task-feasible restriction on template parameters, $\mathscr{R}$ in (1.12) (or with optimized gearing and switching time, $\mathscr{R}^*$ in (1.26)) is reflected in the physical parameters (length, mass, and inertia) of bodies a designer might select for inertial reorientation. A particular template instantiation, $\mathbf{p} \in \mathscr{P}$ could be embodied in myriad ways. This paper considers three categories of physical IR morphologies that have appeared in the literature: tails, radially-symmetric reaction wheels, and coordinated flailing limbs, with respective design spaces, $\mathscr{P}_t$, $\mathscr{P}_w$, and $\mathscr{P}_\ell$. While the physical parameters and dynamics for these systems differ considerably, they all share the same configuration space and (scalar) control input space.[8] Therefore the state and input spaces can be mapped from template to anchor trivially, and we focus our attention on the problem of the parameter spaces. In this section, we show that these bodies can be put into formal correspondence with the template task representation by the introduction of a mapping from these spaces to that of the template,

$$\Xi_i : \mathscr{P}_i \to \mathscr{P}, \tag{1.27}$$

for $i \in \{t, w, \ell\}$, hereafter termed a *morphological reduction*.

The morphological reduction affords designers of these bodies the same insight achieved for templates. The "pullback" of the feasible set of body and task parameters through these maps yields an anchoring design in the sense of guaranteeing task achievement over the entire inverse image,

$$\mathbf{p_i} \in \mathscr{R}_i := \Xi_i^{-1}(\mathscr{R}) \subset \mathscr{P}_i, \tag{1.28}$$

(or similarly, $\mathscr{R}_i^* := \Xi_i^{-1}(\mathscr{R}^*)$), The *Body Selection* and *Performance Evaluation* problems of the previous section can be expressed in the anchor's task-feasible space $\mathscr{R}_i$ by fixing either the task parameters or body parameters, respectively. We will employ both methods to explore reorientation morphology on RHex in Section 1.6.

The kinematics and dynamics of anchors may deviate from that of the template, introducing nonlinearities and configuration dependence into the relationships corresponding to those derived in Section 1.3. For these systems, the morphological reduction is an approximation, with error that varies with task specification and morphology.[9]

For the physical bodies discussed in this manuscript, the parameters defining the powertrain (P, ω_m, s_r), control (t_s), and task (t_f, $\theta_{b,f}$) have direct correspondences in both the template and anchor design spaces, and thus those components of Ξ are simply the identity map and we use the same notation to describe these quantities in both template and anchor. However, equivalent parameters

---

[8] The limbed body is, of course, intrinsically possessed of higher DOF. Here we consider only the case where a coordinating controller has rendered its input and state spaces identical to the template. See Appendix 1.9.1 for a full treatment of this anchoring.

[9] As shown in this section, the tail anchoring is exact when $l_b = 0$, the wheel anchoring is always exact, and the limb anchoring is exact only for the symmetry conditions described in Section 1.4.3.

for effectiveness and inertia are not obvious a priori and therefore are the focus of the following sections (as summarized in Table 1.2 and Fig. 1.2). As shorthand for these non-trivial components of Ξ we use $\Xi_{i,\xi}$ and Ξ_{i,I_d} to denote the canonical projection of Ξ_i onto ξ and I_d, respectively.

1.4.1 Tailed Morphological Reduction

Within this manuscript, we refer to any single mass-offset appendage specialized for inertial reorientation as a "tail" (in contrast to flywheels and limbs, described below), though this configuration could also represent a two-segment body with an actuated spine [4, 48]. As in the template, the tailed system consists of two rigid bodies and one internal degree of freedom, but in this case the mass centers of the bodies are offset from the joint by some distance (l_b and l_t, for body and tail, respectively), and the derivation of the connection field is considerably more involved. The full parameter set for a tailed body motion is,

$$\mathbf{p_t} := [m_b, I_b, l_b, m_t, I_t, l_t, s_r, P, \omega_m, t_s, \theta_{b,f}, t_f], \tag{1.29}$$

that is, mass, inertia, and COM distance from pivot for each of body and tail (Fig. 1.2), as well as the appendage stroke, actuator power, no-load speed, controller switching time, and task specification.

Tailed Body Kinematics

The magnitude of the angular momentum about the system COM is nonlinearly configuration-dependent (see Appendix 1.9.9 for full derivation),

$$\begin{aligned} H_{O,t} = &\left(I_b + I_t + m_r(l_b^2 + l_t^2 - 2l_b l_t \cos\theta_r)\right)\dot{\theta}_b \\ &+ \left(I_t + m_r(l_t^2 - l_b l_t \cos\theta_r)\right)\dot{\theta}_r, \end{aligned} \tag{1.30}$$

where,

$$m_r := \frac{m_b m_t}{(m_b + m_t)} \tag{1.31}$$

is known as the reduced mass. As in (1.4), normalize the angular momentum by the total MOI[10] about the COM, $I_b + I_t + m_r(l_t^2 + l_b^2)$, and define two dimensionless parameters – an equivalent effectiveness,

$$\xi_t := \frac{I_t + m_r l_t^2}{I_t + I_b + m_r(l_t^2 + l_b^2)}, \tag{1.32}$$

and a nonlinearity parameter,

$$\eta := \frac{m_r l_b l_t}{I_t + m_r l_t^2}. \tag{1.33}$$

---

[10] The total MOI for a general tail is configuration-dependent; we take the MOI at $\theta_r = \pm 90°$ to achieve the compact form presented here.

The normalized angular momentum is thus,

$$\widetilde{H}_{O,t} = (1 - 2\xi_t \eta \cos\theta_r)\dot{\theta}_b + \xi_t(1 - \eta\cos\theta_r)\dot{\theta}_r. \tag{1.34}$$

The second dimensionless constant, η, captures the extent to which the system deviates from the linear behavior of the template. Only a subset of the dimensionless parameter space is physically realizable because of coupling between the dimensionless constants and the requirement of non-negativity of the dimensioned parameters (see Appendix 1.9.10). The unreachable region is shaded gray in Fig. 1.5.

As in (1.5), setting $\widetilde{H}_{O,t} = 0$ and applying the chain rule yields the connection field for the tail anchor,

$$\frac{\partial\theta_b}{\partial\theta_r}(\theta_r) = -\xi_t \frac{1 - \eta\cos\theta_r}{1 - 2\xi_t\eta\cos\theta_r}. \tag{1.35}$$

Note that $\partial\theta_b/\partial\theta_r = -\xi_t = const$ when $\eta = 0$ or when $\xi_t = 0.5$, and note that the denominator is nonzero when $2\xi_t\eta < 1$, which is always true for physically-realizable parameters (again, see Appendix 1.9.10). When $\eta > 1$, the sign of the connection may change over the tail's range of motion so that transiently both tail and body rotate in the same direction.

Note that the kinematics are completely described by the connection field, and so two systems with the same ξ_t and η have equal rotations of the body for any given tail rotation. Thus tradeoffs in the physical parameters $(m_b, I_b, l_b, m_t, I_t, l_t)$ that leave the dimensionless parameters (ξ_t, η) unchanged have no effect on the kinematics of the system. In terms of the physical parameters of a robot and tail, this 1-dimensional connection field is,

$$\frac{\partial\theta_b}{\partial\theta_r}(\theta_r) = -\frac{I_t + m_r(l_t^2 - l_b l_t \cos\theta_r)}{I_b + I_t + m_r(l_t^2 + l_b^2 - 2 l_b l_t \cos\theta_r)}. \tag{1.36}$$

This quantity is at most unity (when the tail is infinitely long or heavy), and varies over both the configuration space of the robot and its design space.

For tails pivoting directly at the body COM, $l_b = 0$, the nonlinear terms vanish as $\eta = 0$, and the tail anchors to the template without error via equivalent effectiveness ξ_t. In general, the connection is not constant and the anchoring is approximate; this can be accomplished in a number of ways. The simplest approach (used for the rest of this paper) is to assume negligible effect of nonlinearity, i.e. $\eta \approx 0$, and simply choose $\Xi_{t,\xi}(\mathbf{p_t}) := \xi_t$ as in the body-centered case. This choice of (approximate) morphological reduction is not unique, and may not be the most accurate in all situations, but it works well for all tailed robots described in Table 1.4. One alternative is to assume a small range of motion and evaluate the connection field at an intermediate value, such as $\Xi_{t,\xi}(\mathbf{p_t}) = \partial\theta_b/\partial\theta_r(180^\circ) = \xi_t(1+\eta)/(1+2\xi_t\eta)$. The most accurate approximation for large tail swings is the average value over the full tail stroke (which can be found by integration of the connection field as shown in Appendix 1.9.11). This can be found in closed form but the equation's complexity makes it cumbersome as a design tool, though useful for calculating or reducing error for a finalized design.

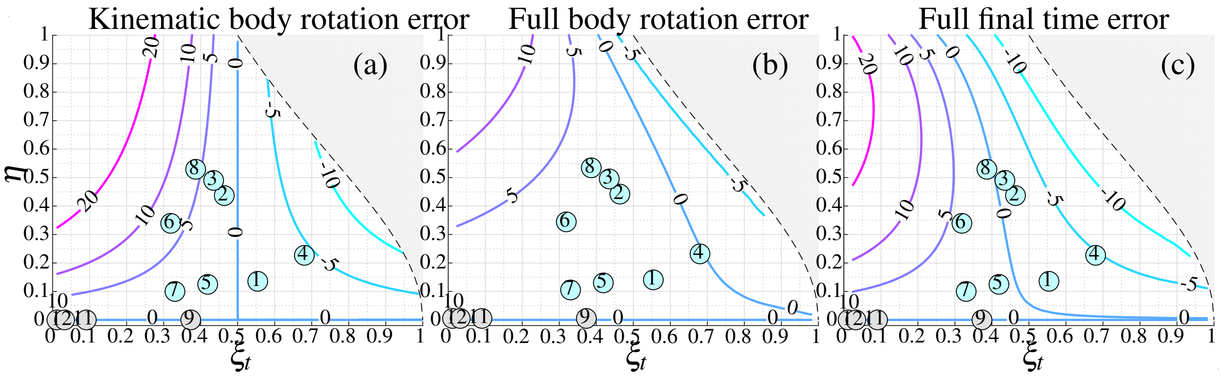

Figure 1.5: Percent errors of approximation for tailed systems undergoing a half tail rotation centered around $\theta_r = 180°$. Numbered points in gray and blue correspond to examples listed in Tables 1.3 & 1.4, respectively. Percent error in (a) body rotation due to effectiveness approximation, $\eta = 0$ (level sets of (1.37)); (b) dimensionless final body rotation due to template optimization (level sets of (1.45)); and (c) final time due to template optimization (level sets of (1.46)). Note that for the full body and time error all examples lie within 5% error.

The relative error in body rotation over a sweep of the tail due to this approximation is plotted in Fig. 1.5a as,

$$e_c(\xi_t, \eta) := \frac{\theta_{b,f} - \xi_t s_r}{\theta_{b,f}}, \tag{1.37}$$

where the exact final body orientation is found by integrating the connection (1.36) over the tail sweep; an analytic expression for this function is derived in Appendix 1.9.11. For robots with $\eta \approx 0$ or with $\xi_t \approx 0.5$, the error of this approximation is essentially negligible (less than 1% for RHex or Tailbot).

Tailed Body Dynamics

Defining for clarity the absolute tail angle, $\theta_t = \theta_b + \theta_r$, and using the balance of angular momentum about the COM of each body, the equations of motion for the full nonlinear tailed system are (see Appendix 1.9.12),

$$\mathbf{M}(\theta_r) \begin{bmatrix} \ddot{\theta}_b \\ \ddot{\theta}_t \end{bmatrix} + \begin{bmatrix} m_r l_b l_t \sin\theta_r \dot{\theta}_t^2 \\ -m_r l_b l_t \sin\theta_r \dot{\theta}_b^2 \end{bmatrix} = \begin{bmatrix} 1 \\ -1 \end{bmatrix} \tau, \tag{1.38}$$

with an inertia tensor,

$$\begin{aligned} \mathbf{M}(\theta_r) &= \begin{bmatrix} I_b + m_r l_b^2 & -m_r l_b l_t \cos\theta_r \\ -m_r l_b l_t \cos\theta_r & I_t + m_r l_t^2 \end{bmatrix} \\ &= (I_b + m_r l_b^2) \frac{\xi_t}{1 - \xi_t} \begin{bmatrix} \frac{1-\xi_t}{\xi_t} & -\eta \cos\theta_r \\ -\eta \cos\theta_r & 1 \end{bmatrix}. \end{aligned} \tag{1.39}$$

Inverting the inertia tensor yields an expression of the tailed body dynamics that, unlike the template (1.6), is both nonlinear and state-dependent,

$$\ddot{\theta}_b = \frac{\tau}{I_{d,t}(\theta_r)} - C_o(\theta_r, \dot{\theta}_b, \dot{\theta}_t), \tag{1.40}$$

where C_o is the Coriolis acceleration, and we define (by analogy to the template's driven inertia), the configuration-dependent inertia, $I_{d,t}$,

$$I_{d,t}(\theta_r) = \frac{(I_t + m_r l_t^2)(I_b + m_r l_b^2) - (m_r l_b l_t \cos\theta_r)^2}{I_t + m_r l_t^2 - m_r l_b l_t \cos\theta_r} \tag{1.41}$$

$$= (I_b + m_r l_b^2)\frac{1 - \frac{\eta^2 \xi_t}{1-\xi_t}\cos^2\theta_r}{1 - \eta\cos\theta_r}. \tag{1.42}$$

In general, the Coriolis terms are negligible for tailed systems with small η, and the anchoring can be accomplished with a constant (average) approximation of the driven inertia. In the simplest case of body-centered tails (i.e. $l_b = 0$, $\eta = 0$), $I_{d,t}$ reduces to I_b exactly and the Coriolis terms drop out, allowing the choice of $\Xi_{t,I_d}(\mathbf{p_t}) := I_b$.

Most of the tails considered in Table 1.4 have $\xi_t \approx 0.5$, and so for these tails consider $I_{d,0.5} := I_{d,t}|_{\xi=0.5}$, which reduces exactly to,

$$I_{d,0.5}(\theta_r) = (I_b + m_r l_b^2)(1 + \eta\cos\theta_r). \tag{1.43}$$

Integrating this function over a half tail sweep, $\theta_r \in [90° \ 270°]$ (approximating the range of motion of many tails in Table 1.4), yields the best approximation for these bodies,

$$\bar{I}^*_{d,0.5} := (I_b + m_r l_b^2)(1 - \frac{2\eta}{\pi}). \tag{1.44}$$

In this paper we choose this as our morphological reduction for the driven inertia, i.e., $\Xi_{t,I_d}(\mathbf{p_t}) := \bar{I}^*_{d,0.5}$, although other choices may work better for some systems. For each of the tailed systems surveyed in this paper the average deviation from (1.42) is less than 15% over their actual tail range of motion; for RHex the error is less than 2.5%.

Final error due to approximate morphological reduction

Using the template relations to constrain the power required to meet the righting task is subject to error from three sources: variation in the connection vector field, the changing inertia tensor, and the Coriolis accelerations. This total error can be quantified over the tail design space (ξ_t, η) for a particular body/tail rotation task by applying the nondimensionalization, (1.13), to the nonlinear dynamics[11] and numerically integrating the resulting system (derived in Appendix 1.9.13), with

---

[11] This step isolates the effect of tail-specific geometry (ξ_t, η) from the remaining parameters, so that error can be quantified with respect to tail parameters alone.

the optimal values of no-load speed and switching time from the template, until the body comes to rest at a time $\tilde{t}_n$. Defining the final body error,

$$e_b(\xi_t, \eta) := \tilde{\theta}(\tilde{t}_n) - 1 \tag{1.45}$$

and final time error,

$$e_t(\xi_t, \eta) := \frac{\tilde{t}_n - \tilde{t}_f^*}{\tilde{t}_f^*}, \tag{1.46}$$

which are plotted in Fig. 1.5b–c for a half sweep of the tail centered around $\theta_r = 180°$. Final error for this maneuver is less than 10% across the large swath of parameter space containing the examples found in the literature thus far; in particular, time and angle error fall within 2% for RHex and within 4% for Tailbot.

1.4.2 Wheeled Morphological Reduction

A reaction wheel is a radially symmetric inertial appendage with mass centered at its joint, and can be seen as a special case of a tail, with $l_t = 0$; the appendage is simply a rigid body with inertia I_w mounted a distance l_b from the body's COM (Fig. 1.2). The parameter set for a reaction wheeled body is,

$$\mathbf{p_w} := [m_b, I_b, l_b, m_w, I_w, s_r, P, \omega_m, t_s, \theta_{b,f}, t_f], \tag{1.47}$$

where in general the wheel stroke, s_r, is infinite.

The connection field (and thus equivalent tail effectiveness) follows from (1.36),

$$\frac{\partial \theta_b}{\partial \theta_r} = -\frac{I_w}{I_w + I_b + m_r l_b^2} := -\xi_w. \tag{1.48}$$

Here the vector field is a configuration-independent constant, as in the template, and so the anchoring is exact. The dynamics are found simply by setting $l_t = 0$ in (1.38) and (1.39); the nonlinear terms disappear and the dynamics become linear with driven inertia,

$$I_{d,w} = I_b + m_r l_b^2. \tag{1.49}$$

The non-identity components of the morphological reduction are thus chosen from (1.48) and (1.49), as listed in Table 1.2.

1.4.3 Limbed Morphological Reduction

Unlike the tail and reaction wheel anchors, whose kinematics' were more complex than the template's and consisted of a greater number of physical parameters but still represented a single degree of freedom, an anchor model of a collection of limbs is truly a higher DOF mechanism.

The general problem of finding "gaits" in this larger shape space that extremize body rotation has been explored in [42]; here we consider the simpler cases that arise when the limbs are coordinated such that the effective shape space is one dimensional. The resulting kinematics lie on a submanifold of the configuration space and, as we show, are equivalent to the kinematics of the simpler template model. Hence the "anchoring" is accomplished through the active, closed loop control that coordinates the limbs.

In general, the effectiveness of an assemblage of limbs varies over their configuration space, even when coordinated. However, two interesting cases arise under certain conditions when all appendages are actively controlled to be parallel, that is each leg's relative angle is commanded to be either $\theta_i = \theta_r$ or $\theta_i = \theta_r + 180^\circ$, for some common θ_r. Given N limbs arranged with pivots in a line coincident with the body's COM (typically the centerline of the robot's body), a sufficient condition[12] for configuration-independence of the connection field is that the limbs are identical (each with mass m_t, length l_t, and MOI I_t), and that the pivot locations are symmetric across the body COM (as with the limbs of RHex, for example). Let $m_{tot} := m_b + N m_t$ represent the total system mass, and ℓ_i the distance from body COM to the ith pivot location (generalizing the tail anchor's pivot offset l_b). The expression of the total angular momentum (derived in Appendix 1.9.14), reduces considerably in two illuminating examples, depending on the phasing of the limbs (represented here by $s_i = \pm 1$, with s negative for legs out of phase with θ_r by 180°). The full parameter set for an N-limbed system with the symmetry condition above is,

$$\begin{aligned}\mathbf{p}_\ell := [&m_b, I_b, \ell_1, s_1, \ldots, \ell_N, s_N, l_t, m_t, I_t,\\ &s_r, P, \omega_m, t_s, \theta_{b,f}, t_f],\end{aligned} \tag{1.50}$$

where here we assume for simplicity the limbs share the same range of motion s_r, and the power P is taken to be the sum across all limbs.

RHex has six identical legs arranged in symmetric pairs of pivots along the centerline of the body; that is, $N = 6$, $\ell_1 = -\ell_3$, $\ell_2 = 0$, and all legs have equal mass m_t and length l_t. The pairs of legs are driven in anti-phase to generate an alternating tripod gait when walking or running, a condition that could be modeled here by taking s_i negative for odd i and positive otherwise, so that $\sum_{i=1}^{6} s_i = 0$. In the anti-phase case, the angular momentum reduces to,

$$H_{O,l} = (I_p + N(I_t + m_t l_t^2))\dot{\theta}_b + N(I_t + m_t l_t^2)\dot{\theta}_r, \tag{1.51}$$

where $I_p = I_b + m_t \sum_{i=1}^{N} \ell_i^2$. When all legs are in phase, $\sum_{i=1}^{6} s_i = N$ and the angular momentum is,

$$H_{O,l} = (I_p + N(I_t + m_{rt} l_t^2))\dot{\theta}_b + N(I_t + m_{rt} l_t^2)\dot{\theta}_r, \tag{1.52}$$

with the subtle difference being the adjusted mass $m_{rt} := m_b m_t / m_{tot}$, a generalization of m_r. In either case, the connection field is constant, and thus the equivalent template effectiveness is error-

---

[12] The necessary condition is considerably more general, see Appendix 1.9.14 for details.

free,

$$\Xi_{\ell,\xi}(\mathbf{p}_\ell) := \xi_\ell = \frac{N(I_t + m_k l_t^2)}{I_b + m_t \sum_{i=1}^{N} \ell_i^2 + N(I_t + m_k l_t^2)}, \tag{1.53}$$

where $m_k = m_t$ when leg pairs are out of phase, and $m_k = m_{rt}$ when legs are in phase. Since $m_t > m_{rt}$, anti-phase leg swings are more effective than in-phase swings, as explored further in Section 1.5.2.

The multi-body dynamics of a robot with several phased appendages are considerably more complex than the developments of the previous sections, and should be derived carefully for any particular case of interest. Here we merely suggest a naïve mapping based on the rotating inertia as expressed in the symmetric cases outlined in Section 1.4.3:

$$\Xi_{\ell,I_d}(\mathbf{p}_\ell) := I_{d,\ell} = I_b + m_t \sum_{i=1}^{N} \ell_i^2, \tag{1.54}$$

mapping the total input power across all limbs to the template.

1.5 Comparative Morphology and Scaling

Each of the diverse IR bodies of the previous section can accomplish the given task, raising the question of how morphology shapes the available design choices. The differences can be expressed and compared directly through each system's morphological reduction, as summarized in Table 1.2. In this section we examine the consequences of those anchoring relations and explore the implications for inertial reorientation at sizes large and small.

1.5.1 Examples from the literature

To facilitate our comparative approach, we present examples of IR machines from the literature in Tables 1.3 & 1.4 (compiled using the references shown and personal communications[13]). As an interesting contrast to the mobile robots that are the focus of this paper, we included another notable example of terrestrial dynamic IR – a small, off-road motorcycle ("dirt bike"), as skilled riders are known to modulate the acceleration of the rear wheel to control orientation during leaps and tricks [18]. Most use morphology designed specially for IR, but three machines (the two legged examples, and the motorcycle) feature appendages designed for terrestrial locomotion that can be co-opted for aerial IR. The mass range covered by the examples is surprisingly large – over 300 fold among the tailed robots, and over three orders of magnitude in all. This is not a comprehensive list of all robots harnessing inertial forces; notably, we have omitted devices where the tail moves in a plane far from the body COM, as in [11]. However, the diversity of the chosen

---

[13] Values differing from those in the cited references are more up-to-date or accurate.

machines provides both a verification of the efficacy of the templates and anchors design approach (noting the low final error for all machines) and enables some useful comparisons, as discussed in the following subsections.

1.5.2 Selection of morphology for inertial reorientation

When is it appropriate to add a new appendage to a limbed body; and when is it better to assign the inertial appendage role to a tail rather than a reaction wheel? In short, tails provide the most reasonable path to high values of effectiveness ($\xi \approx 0.5$ or higher), and are thus well suited to aggressive, dynamic maneuvers, while reaction wheels provide infinite stroke over longer time scales. Limbs may provide a middle ground, varying considerably in morphology across extant robots, and thus in effectiveness, and may provide some IR capability without any additional payload.

Wheeled vs. Tailed Bodies

The symmetric mass of a reaction wheel provides the advantage of simple, linear dynamics and infinite range of motion. Of course, large wheels become cumbersome more quickly than a tail – a practical reaction wheel could be no larger in diameter than a robot body's smallest dimension. In natural systems, tails greater than body length are common, and thus we can expect larger effectiveness from tails than from reaction wheels. For example, between the comparably-sized Hexbug [9] and TaYLRoACH [8] (the former employing a pivot-centered double tail mass which acts like a wheel, and the latter an offset tail), the tailed design achieves roughly 15% higher effectiveness (0.44 vs 0.38) with 20% lower appendage mass ($4g$ vs $5g$, Tables 1.4 & 1.3).

Since wheels and limbs need not incur the constrained range of motion suffered by practical 1-DOF tails,[14] their effectiveness seems less important (i.e. it does not intrinsically limit body rotation) – so why bother with a relatively bulky tail? The answer is revealed though the power equation, (1.22), and its inverse dependence on tail effectiveness. For a given task, a doubling of ξ reduces the power requirement by half. Herein lies the fundamental limitation of low-effectiveness devices for fast reorientation: a small flywheel will require much more power than a relatively long tail for the same maneuver. The short time scales available for aerial reorientation in terrestrial robots suggest a limited role for internal reaction wheels, but when this constraint is lifted (e.g. in space robotics [49]), such devices should be ideal. The motorcycle example in Table 1.3 provides an instructive exception – its IR "appendage" is driven by the machine's locomotive powertrain, resulting in the largest body mass-specific power (over 300 W/kg) of any example here, enabling impressive aerial maneuverability in the right hands. When retrofitting an IR appendage to an existing machine, the lower power requirements of a tailed design should lead to generally lower added mass than a less effective wheel. For tails and wheels of comparable length scale, the advantage goes to the wheel due to the subtle effect of the reduced mass – the offset tail pulls the

---

[14] More complex tails can escape this limitation in some maneuvers, e.g. the conical tail motion generating roll in the falling gecko [19].

system COM towards the tail as appendage mass increases, thus decreasing effectiveness (m_r in ξ_t is strictly smaller than m_t).

Limbed vs. Tailed Bodies

For a given total added mass, a single appendage (tail) will generally provide larger effectiveness than two or more appendages. The squared dependence of effectiveness on length makes elongate appendages most attractive; hence, dividing a tail into two limbs each with half the length and mass of the original appendage would entail a significant loss of performance (a pair of symmetric flywheels sees a similar disadvantage). On the other hand, in many cases (for example RHex), limbs also provide infinite stroke, can exceed body dimensions without negative consequences (unlike a reaction wheel), and will by definition be already present on a legged terrestrial robot, eliminating any added cost or complexity. Machines with relatively long limbs will likely benefit most from this strategy (the quadruped Cheetah Cub achieves almost three times the IR effectiveness of RHex with a third fewer limbs, see Table 1.3). However, the use of these appendages for aerial reorientation may pose significant drawbacks, most notably a constraint on their final orientation upon landing (touching down feet-first is typically desirable). Explicit design for reorientation will likely also conflict with other limb design priorities (for example, distal mass is typically a disadvantage when interacting impulsively with a substrate or when retracting the limb during the swing phase [50]). Still, in many cases even a limb designed for running may result in enough inertial effectiveness to be useful in small (but significant) rotations. We will test this hypothesis in Section 1.6.2.

Core vs. Appendage Actuation

A tailed body and an actuated spine [4, 48] can both be represented by the same anchor model, but represent very different design propositions. The primary advantage of a spine is that it may preserve the overall morphology (in particular volume and body envelope) by essentially separating the body into two chunks with much lower MOIs (with $\xi_t \approx 0.5$ if the segments are similar). Meanwhile, an added tail will in general extend the body envelope. The major drawback of body-bending (as with using limbs for inertial reorientation) is that the final orientation of both segments is important if the legs of the robot are to hit the ground simultaneously [48] – as we show in Section 1.6.2, increasing the number of contact limbs when landing can greatly increase survivability. Furthermore, existing robotic platforms (like RHex) cannot be substantially altered without a major redesign, but their distal appendages may be relatively easy to add, subtract, or change. The core actuation approach may have increased advantages outside the planar scope of this paper; compare for example roll maneuvers in the falling cat [17] against those of the falling gecko [20].

Maximizing tail performance

Intuitively, tail effectiveness increases with tail mass, length and inertia, and decreases with the corresponding body parameters. Minimizing tail offset (placing the joint close to the body COM) has the dual benefits of increasing performance and reducing nonlinearity (the MSU jumping robot [7] comes closest to this ideal, while Tailbot could increase effectiveness by 10% by centering its tail at the body's COM). Concentrating tail mass at the appendage's extreme produces the most effectiveness per unit tail length (recall l_t is the distance from pivot to tail COM, which if $I_t \neq 0$ is strictly less than the total tail length), and thus an idealized tailed body consists of a point-mass tail pinned at the body's COM. Less intuitive is the trade-off between tail mass and length; clearly a given effectiveness can be accomplished with any number of combinations of each, though increasing tail mass eventually sees diminishing returns due to the effect of the reduced mass (1.31). By contrast, increasing tail length quadratically increases effectiveness. RHex's relatively long tail achieves 75% higher effectiveness than that of the Kangaroo robot with approximately the same fraction of overall mass dedicated to appendage. At what point a tail's length becomes cumbersome is surely dependent on the constraints of other tasks and varies widely between applications, but the examples of Table 1.3 see tail lengths commonly exceeding one body length.

1.5.3 Scaling of Inertial Reorientation

Agile mobile robots span an increasingly large size range, raising the question of whether inertial reorientation remains a practicable strategy for robots large and small. In the next section, we design a tail for RHex with a task specification based on the righting performance of Tailbot, a robot approximately one fiftieth of RHex's mass. How will this mass difference dictate changes in morphology or mass-specific motor power? Because ξ is dimensionless and dependent only on morphology, isometrically [51] scaled robots are kinematically similar – for a given appendage rotation, the body rotation will be identical at any size scale. However, the power required for a maneuver will vary with size.

Consider a robot isometrically scaled by a length L. Assuming uniform density, the robot's mass will scale by L^3 and its inertia by L^5. If the robot were required to reorient through the same angle in the same time regardless of size, then by substitution into (1.22), (replacing I_d with L^5 and dividing both sides of the inequality by L^3) we would require power per unit robot mass (power density of the whole machine) $P_d \propto L^2$. However, because gravity is constant, g, a larger robot will fall slower relative to its length (i.e. dynamic similarity [52]). For a free fall distance of $h \propto L$, the time available is $t_f = \sqrt{2h/g} \propto L^{1/2}$. Therefore, from (1.22), the required power per unit robot mass,

$$P_d \propto \frac{I_d}{m t_f^3} \propto \frac{L^5}{L^3 L^{3/2}} = L^{1/2}, \tag{1.55}$$

scales as the square root of length. This indicates that inertial reorientation gets mildly more expensive at large size scales; larger robots may suffer reduced performance, or must dedicate a growing portion of total body mass to tail actuation (or, noting the inverse relationship with ξ, to increased tail effectiveness). However, RHex and Tailbot span a characteristic length range of almost four fold without dramatic differences in ability (see Fig. 1.7); in fact, the smaller machine dedicates more body mass to its tail motor than RHex (6.9% vs. 3.3%), even as the larger machine has relatively higher body inertia (an isometrically-scaled Tailbot of RHex's mass would have $I_b = .11\ kgm^2$, almost 30% lower than RHex). In this case, differences in actuator performance trump scaling – Tailbot uses a low-quality brushed motor, while RHex's higher quality components, [4], allow it to escape the penalty of size.

Intriguingly, generalization of the IR template dynamics suggests that (1.55) may govern scaling of other power-limited self-manipulation tasks, including aspects of legged locomotion. Consider a robot with its feet planted firmly on the ground, rotating its body in the yaw plane about an actuated hip. This situation could be modeled by a single rigid body, connected to the ground by a motor – that is, the system can be modeled by the IR template, considering the ground to be the "appendage", with I_a infinitely large and $\xi = 1$. Power for reorientation for this grounded reorientation task scales as in (1.55).[15] In this simplified scenario, power-limited reorientation scales identically whether the body rotation is driven by inertial or ground reaction forces; we therefore hypothesize that inertial appendages may enhance agility at any size scale permitting legged maneuverability.

1.6 Design for Inertial Reorientation

In this section, we present examples of the complementary design problems of *Body Selection* and *Performance Evaluation* (introduced in Section 1.3) by exploring IR morphology for RHex. The first step in the *Body Selection* problem, P1, is to specify the task or set of tasks required of the machine (i.e. parametrizing (1.1)); the task and other (external) concerns will determine the overall morphology, subject to the trade-offs discussed in the previous section. With a body plan chosen, the designer is then free to pick any set of physical parameters in $\mathscr{R}_i$ that best meets performance needs outside the reorientation task. A naïvely rational design approach might introduce a cost function, $C(\mathbf{p}_i)$, expressing the impact of the IR morphology on some other critical task (e.g. legged locomotion) or penalty (e.g. parts cost) and solve the resulting constrained minimization task. However, it is notoriously difficult to encode robustness within the rigid optimization framework. Robots, putatively general purpose machines, will typically be assigned multiple critical tasks, ofttimes with conflicting objectives (e.g. fast locomotion and steady perception). More frequently, legacy constraints imposed by a robot's existing design will further reduce the design problem to the selection of one or two parameters, precluding the possibility of an optimized design. Every design problem (whether of tails, limbs, flywheels or other morphology) will likely entail its own set of constraints, assumptions and objectives which must be chosen such that (1.28) results in a suitable and unique design solution.

---

[15] The scaling of relevant time scale (during a single step) again follows dynamic similarity, as stride frequency in running scales with $\sqrt{L}$ [52].

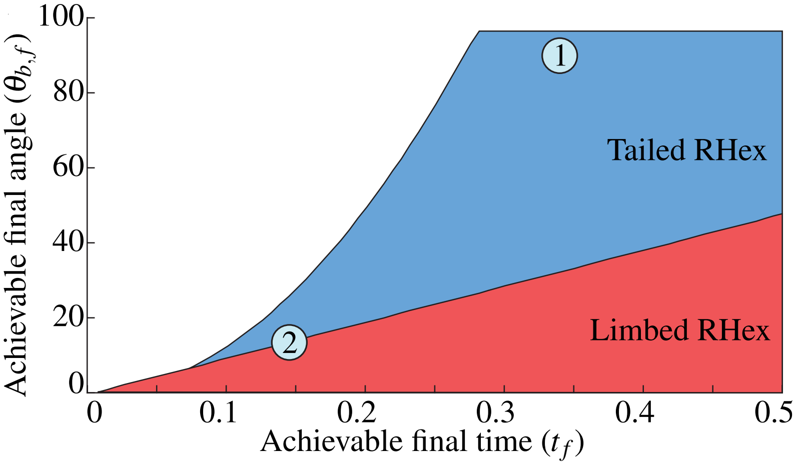

Figure 1.6: The regions of task space (a projection onto the $\theta_{b,f}$ and t_f components of the feasible set $\mathscr{R}$) accessible by two instantiations of IR morphology on RHex for the reorientation task, (1.1). The tail is limited by power for the quickest tasks, and by stroke for slower maneuvers; its higher effectiveness allows far more useful rotation at relevant time scales. The numbers indicate the two experimentally-validated tasks: 1) tailed reorientation in one body-length fall and 2) limbed reorientation during a leap. Both tasks fall within the tailed body's feasible set, but task (1) exceeds the limbed body's capability.

In the *Performance Evaluation* problem, P2, the fixed design restricts the system performance to a subset of task space (the projection of the feasible design set $\mathscr{R}$ onto the $(\theta_{b,f}, t_f)$ subspace). This region can be computed for set values of ξ, I_d, P, s_r, and ω_m by using (1.12) to query the feasibility of a task (values of t_f and $\theta_{b,f}$), selecting the switching time t_s to satisfy the final angle condition, if possible. A fixed template design will necessarily be suboptimally geared for most tasks in the feasible task subspace; the cost of this suboptimality (along with that of submaximal current limit) can be calculated through the changing power cost, k_p, in (1.22). We compare the achievable task subspace for two implementations of IR morphology on RHex in Fig. 1.6, and list values of k_p where applicable.

In practice, the design process will use both the selection and evaluation problems to settle on a solution both practicable and task-feasible. Starting with the *Body Selection* problem (parametrizing a task and choosing a body plan), the designer should first use $\mathscr{R}_i^*$ to achieve a rough design, as the reduced (gearing-optimal) space and simpler form of the constraints will highlight the consequences of any choices (fixing legacy-constrained physical properties, or adding constraints to satisfy other task objectives). Since practical concerns will further limit parameter choices (e.g. the optimal powertrain is not likely to exist as an off-the-shelf product), the designer should then use *Performance Evaluations* of several candidate designs to find a feasible and physically realizable design. A major advantage of this approach over a straightforward optimization is that the effects of the inevitable deviations from optimality can be quantified and compared (e.g. through k_p), thus informing the designer's concessions to practicability.

Real-world actuator selection is constrained by factors beyond rated power, as used in the preceding sections. Choosing a powertrain for a real system also involves characterizing motors by their electrical (current, voltage), thermal, legacy (constraints of the robot's body), physical (size, mass), financial, and labor costs, as we show in the selection of the final motor for the following design experiments.

1.6.1 Appendage design for RHex

Tail payload

As an example of the *Body Selection* problem, P1, we designed a tail for RHex by first specifying the task parameters, and then using $\mathscr{R}_t^*$ to guide the selection of the remaining values in $\mathbf{p}_t$; the robot's existing morphology further constrains our choices to a subset of $\mathscr{R}_t$.

In the interest of direct comparison with Tailbot [2], we selected task specifications based on replicating one element of the smaller robot's behavioral repertoire: a reorientation of $\theta_{b,f} = 90^\circ$ in the course of falling one body length, L. For RHex, this translates to the task specification,

$$\theta_{b,f} = 90^\circ, \qquad t_f = \sqrt{\frac{2L}{g}} \approx 0.34\ s, \tag{1.56}$$

where g is the gravitational acceleration. As discussed in Section 1.5.2, the large effectiveness easily achieved by a tail makes that morphology the most attractive choice for this relatively aggressive maneuvering task (significantly decreasing the actuator requirements through the power equation, (1.22)).

Of the full set of tailed-body parameters $\mathbf{p_t}$, (1.29), two (body mass and inertia) were already set by RHex's existing body morphology, and a third (pivot location) was constrained by the body's envelope. Confident that we could make the tail very nearly a point mass on a near massless rod (thus maximizing effectiveness per unit mass and length), we further eliminated I_t.[16] While Tailbot was a special-built machine, the tail for RHex was added to the existing platform as a modular payload [4] and as such the range of motion is significantly lower than Tailbot's. As the design of the modular payload system limits maximum tail sweep to 180° regardless of pivot position, we centered the tail along the body axis to minimize $l_b = 8\ cm$ (maximizing effectiveness, reducing η and further motivating the efficacy of (1.26)); a small safety margin to avoid collision with the body reduced stroke slightly further to $s_r \leq 172.5°$. With the selection of this range of motion limit, tail effectiveness is constrained by (1.26) to $\xi_t \geq 0.522$, leaving the question of the balance between tail length and mass. The addition of weight to RHex via external payload has known (small) performance costs, while the addition of a long tail has unpredictable and potentially large consequences on capability outside of aerial righting; we therefore chose to minimize tail length by selecting an additional mass constraint based on previous experiences with modular payloads, $m_t \leq 0.6\ kg$ (giving $m_r = 0.56\ kg$). With $I_t \approx 0$, the minimum tail length to meet the effectiveness requirement can be found directly from the definition of ξ_t (see Table 1.2), and is $l_t \geq 0.55\ m$. As assembled, RHex's actual tail effectiveness is slightly larger than required, and is about 20% larger than that of Tailbot (see Table 1.4), as needed to achieve feasibility respecting the stroke constraint consequent upon the roughly 30% reduction of its tail stroke relative to that of the smaller machine.

Meeting the body stroke specification fixed all parameters save motor power, which is constrained by the second inequality in (1.26); the smallest allowable value of P satisfying this constraint is approximately 39 W, with an optimal no-load speed just over 2 Hz. The Maxon pancake motors that drive RHex's legs are rated for 50 W continuous operation, and can achieve transient output up to 342 W [4], but practical concerns including thermal safety limit current to 12 A, just 33% of transient stall current (see Appendix 1.9.3). A putative design using these motors falls well within $\mathscr{R}_t$ despite their suboptimal gearing of 28:1 (effective $\tilde{\omega}_m \approx 1.0$, $\beta = 0.33$ giving $k_{p,t} \approx 11$ for this task, roughly four times higher than optimal); we found that mitigation of integration issues outweighed any possible weight savings that could be had by choosing a smaller motor with more optimal gearing. The chosen design is capable of rotating the body to 90° within a predicted final time of approximately 300 ms, well within the performance specification. This tailed design is tested in Section 1.6.2.

Flailing limbs

A highly attractive alternative to the added complexity of a tail is to simply use RHex's existing limbs, preferably in the in-phase condition so as to land on all six simultaneously. The total re-

---

[16] The mass-centered rotational inertia of a small mass on a light rod is far smaller than the offset inertia, $m_r l_t^2$; the I_t value of this tail was therefore reported as zero in the cited work.

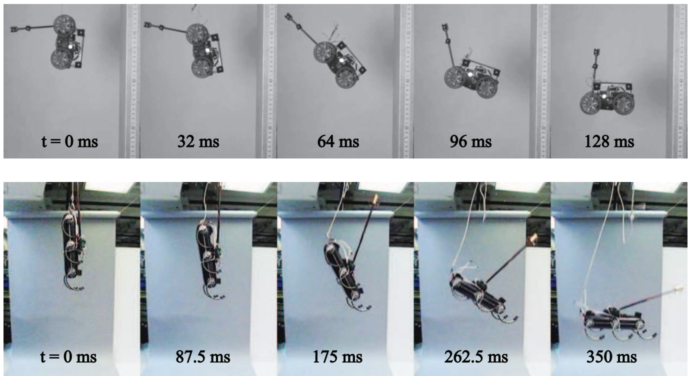

Figure 1.7: Dynamically similar aerial righting in two robots spanning a 60-fold mass range: Tailbot (top) and RHex (bottom). Each machine rotates 90° in approximately one body length of fall.

orientation effectiveness, as predicted by (1.53), is $\xi_\ell = 0.037$ (see Table 1.3). With $\mathbf{p}_\ell$ fixed by the existing design, we can query (1.12) to check the feasibility of this body with respect to the task, (1.56). The unlimited limb rotation means the design trivially meets the stroke specification, but not within the final time (Fig. 1.6). The very low effectiveness of the combined limbs necessitates almost eight full swings of the limbs to complete the body stroke requirement of (1.56), and thus a substantially different power train than is used for terrestrial locomotion: the optimal no-load speed for the limbed design of 2,178 RPM is almost 13 times higher than RHex's maximum leg speed.

While RHex's existing morphology is inadequate for this highly agile task, its limbs still provide a potentially useful IR capability – the limbed system can rotate 32.3° in one body-length of fall, or over 50° in the 1.36 m fall we used to test RHex's tail (see Fig. 1.6). Such small reorientations could be significant especially when running, where the nominal body orientation varies a similarly small amount [53]. One full rotation of RHex's six limbs produces 13.3° of body rotation, and its powertrain can achieve this reorientation in as little as 150 ms. This new reorientation task fits easily into the aerial phase of a single leap, usefully allowing modulation of landing angle; we test it empirically in Section 1.6.2.

1.6.2 Experiments on RHex

IR Task Implemented on the Tailed-Body RHex Design

As an anecdotal validation of the foregoing scaling arguments, we conducted a series of inertial reorientation experiments on RHex (Figs. 1.7 & 1.8). In the first experiment, the robot was dropped nose first from a height of 1.36 m (over 8 times the standing height and 2.7 times the body length, though we still required the robot to meet the task specification in (1.56)).

We implemented a PD (proportional-derivative) controller on the internal angle in lieu of a

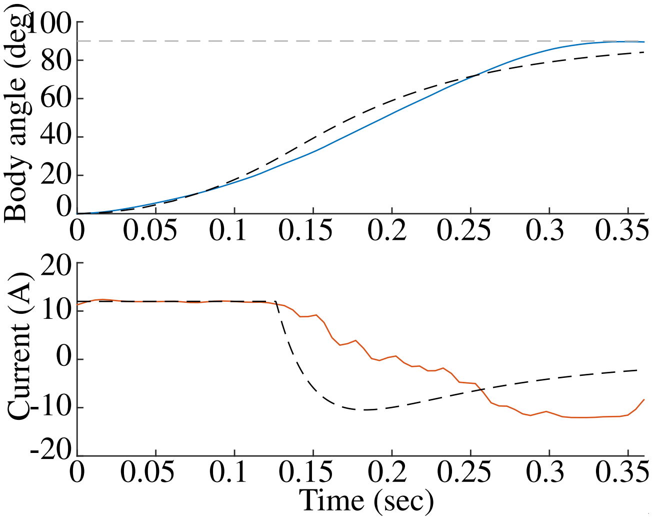

Figure 1.8: Logged data from a tailed robot experiment. (Top) Body angle, from high-speed video (blue) and predicted by template with PD controller (dashed); (Bottom) motor current, applied (red) and predicted by template (dashed). Disagreement between model and template is primarily due to unmodeled compliance in the tail pivot and shaft.

bang-bang controller – as discussed in Appendix 1.9.2, the saturated PD controller converges to the bang-bang design given large enough gains. In practice, the sensor bandwidth and other unmodeled effects result in oscillation around the regulated angle, so we relaxed the high gain requirement slightly, accepting the slight performance cost in favor of the extra robustness provided by the closed-loop design (the effective current switching time of approximately 0.22 seconds corresponds to a $\tilde{t}_s \approx 2.85$, slightly later than the optimal 2.40 for the chosen gearing and current limit). The legs were simultaneously controlled to point towards the ground.

Data from a typical reorientation experiment can be seen in Fig. 1.8; we logged sensor data and shot high-speed video at 210 frames per second. The robot rotated to within 1° of horizontal before landing on all six legs, taking about 350 *ms* to complete the reorientation, corresponding to a dimensionless halting time of approximately 4.55, and a corresponding power cost $k_p \approx 23.5$ – more than nine times optimal, and twice the cost predicted in section 1.6.1, due to the suboptimal controller and several unmodeled effects. Drivetrain losses decreased output torque by roughly 25% and the tail mount and carbon fiber shaft exhibited substantial elasticity, causing acceleration lag and increasing the deviation from bang-bang torque application. Despite the high cost of the suboptimal design, the robot completes the task within 3% of the target time. As further verification of the template, we added the PD controller and drivetrain efficiency losses to the model; simulation of this more accurate (suboptimal) template is plotted against experimental data in Fig. 1.8.

When dropped with the tail controller off, the robot impacted the ground nose first, with only

Figure 1.9: RHex surviving a run off a cliff outdoors.

the front pair of legs in support. The impacted limbs quickly snapped, allowing the robot's body to strike the ground, causing internal damage. We therefore conclude that the active inertial tail substantially expands the task space of RHex by tripling the number of support limbs available for impact mitigation (thereby roughly tripling the strain energy tolerable before failure and increasing the survivable falling height).

To demonstrate this new ability for RHex in a practical task, the robot was also tested outdoors running along and then off of a 62 *cm* (3.8 hip-heights or 1.2 body-lengths) cliff. This stabilization task is governed by a different set of performance constraints that could be probed analogously to our approach to the reorientation task in Section 1.3.3; [17] in lieu of a more exhaustive analytic exploration of this task space, we note that this fall nearly saturated RHex's tail stroke and likely represents a near-limit for full stabilization at this running speed. The robot's inertial sensors detect the cliff upon initial body pitch, then actuate the tail according to the same PD control policy, landing the robot on its feet (Fig. 1.9). As with the indoor experiments, a test with RHex running off a cliff with a passive tail confirmed that the robot lands nose first.

IR Template Anchored on RHex as a Limbed Body

Finally, a third set of experiments tested the ability of RHex's legs to work as inertial tails. The existing limb design is incapable of achieving the original task (90° body rotation in 0.34 *s*, Fig. 1.6), and so instead a feasible task consisting of a single rotation is used instead to test the flail kinematics. As first reported in [34, Sec. IV-C.5], after leaping vertically into the air all of the legs were recirculated together to the same landing angle. Using the legs in phase for this experiment allows the robot to land on all six, though using the legs out of phase would have increased the effectiveness by about 3.5% (Section 1.4.3).[18] The limbs were rotated clockwise in the first experiment and counterclockwise in the second for a net difference of 360° in stroke; the difference in final body angle between the two cases was 14°. While the leap gave only enough time for a single revolution of the limbs, the resulting body rotation made an appreciable difference in the quality

---

[17] The stabilization task could be specified by keeping the body angle within some allowable deviation over a time horizon t_f by swinging the tail to mitigate an impulse characterized by $\tilde{H}$ as in (1.4). Constraints analogous to (1.26) could be derived by solving the template kinematics and dynamics subject to this new task.

[18] As in the tailed trials, we used a PD controller on the internal angle (see Appendix 1.9.2), however here this single control effort was pulled back into the more complicated limbed body through an anchoring controller (specifically, six independent PD controllers each regulating a limb to the common commanded position.

of the landing, supporting our hypothesis that IR with even unspecialized limbs can be useful.

1.7 Conclusion

As mobile robots proliferate in the complexity of both their morphology and behavioral scope, there is a growing need for principled methodology relating their body design to their capability. The templates-and-anchors approach adopted for this paper provides a unifying framework for the comparative morphology of robots (and even animals) and a practical approach to the design and evaluation of inertial reorientation performance on real robots. We defined the Inertial Reorientation template, the simplest model of an IR maneuver, equipped with a DC motor-like model parametrized by peak output power. The template revealed the particular importance of a single parameter, defined here as IR effectiveness, which prescribed both the appendage rotation needed to move a body and the power needed to do so in fixed time. Dimensional analysis of template behavior revealed that a relatively modest increase in power density (growing with the square root of length) should be required to retain righting performance as platform size increases.

The model's linear dynamics, along with a bang-bang controller, enabled analytic solution of the template's single-switch reorientation behavior, revealing a simple relationship between morphology and performance, described by the task-feasible set $\mathscr{R}$, (1.12). We then showed how the feasible set could be "pulled back" through a more complex body's *morphological reduction* (defined as the possibly-approximate mapping between parameter spaces of real robot body and abstracted template), to provide design restriction to a more usefully diverse set of machines. The resulting set of feasible real designs (1.28) retains enough freedom (e.g. allowing length to trade for mass) to afford some "optimization" in the sense of minimizing the impact of the design on other task abilities. In practice, concessions to practicality will necessitate deviations from optimality; fortunately, our framework gives the designer flexibility to compare candidate (suboptimal) designs and even quantify the performance cost of those compromises (e.g. through (1.23)).

Our approach facilitated the design of a tail for RHex, enabling inertial reorientation capabilities dynamically similar to the much-smaller Tailbot. A separate anchoring to the same template quantified the capability of RHex's existing appendages (its six semi-circular legs) to produce useful reorientation in their own right, and revealed a preferred posture for doing so. A recent proliferation of tails (and other high-effectiveness appendages) for inertial righting allows us to calculate and compare effectiveness across a number of independent designs; generally their effectiveness is close to 0.5, where the connection becomes configuration-independent. As a result, these designs anchor nicely to the IR template with relatively low error. We expect that most well-designed appendages will fall within this paradigm.

The constraints making up $\mathscr{R}$ and its gearing-optimal refinement (1.26) revealed general principles of design for righting morphology, while the morphological reductions provided crucial insight into the tradeoffs of each body type; we provide a detailed discussion in Section 1.5. Tails are a natural choice for fast, large amplitude inertial reorientation, owing to the ease at which they can be designed for high effectiveness values without disrupting the existing platform morphology. However, as legged robots increase the numbers of DOFs in limbs and body alike, these affordances should provide compelling sources of inertial reorientation as well. In practice, the choice of anchor morphology for enabling inertial reorientation in a robot is tightly coupled to overall function with respect to its mission, historical and other constraints on body design, and the task-specific rewards for high reorientation performance.

While the present analysis focuses on purely aerial maneuvers, inertial appendages also show promise in a variety of terrestrial tasks, stabilizing or actuating turns [8, 10], or stabilizing pitch over obstacles [2]. Likewise, inertial appendages have utility beyond the sagittal plane for aerial maneuvers, with out-of-plane appendage swings capable of effecting body rotations in yaw and roll as well as pitch, e.g. [20, 33]. We postulate that tail effectiveness will remain a useful metric in these arenas as well, though the analysis of the dynamics and control affordance underpinning such behaviors remains an open problem.

1.8 Chapter acknowledgments

Some of the data in Tables 1.4 & 1.3 was collected through personal communication with the authors of the cited work, and we would like to thank Nick Kohut, Jianguo Zhao, Pei-Chun Lin, Avik De, and Steve Heim for contributing this morphometric data. The motorcycle example used information from Zero Motorcycles, Zero FX. The authors would like to thank Praveer Nidamaluri for building the X-RHex tail, Aaron Effron and the four anonymous reviewers for their notes on the manuscript, as well as David Hallac, Justin Starr, Avik De, Ryan Knopf, Mike Choi, Joseph Coto, and Adam Farabaugh for help with RHex and experiments.

1.9 Chapter appendix

1.9.1 Generalized Template-Anchor Relationship

This section develops a general framework for the anchoring of more complex dynamical systems to a simpler template dynamical system [38]. This is a more general notion of anchoring than in, e.g., [54], which requires the template dynamics be, "conjugate to the restriction dynamics of the anchor on an attracting invariant submanifold," or in [3, Sec. 1.2], which seeks, "controllers whose closed loops result in a low dimensional attracting invariant submanifold on which the restriction dynamics is a copy of the template."

In particular consider two dynamical systems: the "template", X, and the "anchor", Y. Each system has a state ($x \in \mathscr{X}$ and $y \in \mathscr{Y}$, respectively), control input ($u_X \in \mathscr{U}_X$ and $u_Y \in \mathscr{U}_Y$, respectively), parameter set ($p_X \in \mathscr{P}_X$ and $p_Y \in \mathscr{P}_Y$, respectively), and dynamics ($\dot{x} = f_X(x, u_X, p_X)$ and $\dot{y} = f_Y(y, u_Y, p_Y)$, respectively). The template is the simpler model, so in general, $\dim \mathscr{X} \leq \dim \mathscr{Y}$.

The generalized anchoring is a specification of a set of mappings between the state spaces, control inputs, and parameter sets of the template and anchor. Specifically, define a *state reduction*,

$h : \mathscr{Y} \to \mathscr{X}$, that anchors the state space, and its right-inverse, $h^\dagger : \mathscr{X} \to \mathscr{Y}$, such that $h \circ h^\dagger = id_X$. Let Dh and $Dh^\dagger$ be the Jacobians of these maps. Define similarly a *control reduction*[19], $g : \mathscr{U}_Y \to \mathscr{U}_X$, that anchors the control input, and its right-inverse, $g^\dagger : \mathscr{U}_X \to \mathscr{U}_Y$, such that $g \circ g^\dagger = id_{\mathscr{U}_X}$. Finally, define a *parameter* or *morphological reduction*, $\Xi : \mathscr{P}_Y \to \mathscr{P}_X$, that anchors the parameter space, and its right-inverse, $\Xi^\dagger : \mathscr{P}_X \to \mathscr{P}_Y$, such that $\Xi \circ \Xi^\dagger = id_{\mathscr{P}_X}$. Collectively these six maps fully define the anchoring of Y in X.

An anchoring will be called *exact* if,

$$f_Y(y, u_Y, p_Y) = Dh^\dagger \circ f_X(h(y), g(u_Y), \Xi(p_Y)), \tag{1.57}$$

which implies that,

$$f_X(x, u_X, p_X) = Dh \circ f_Y(h^\dagger(x), g^\dagger(u_X), \Xi^\dagger(p_X)) \tag{1.58}$$

(though the reverse is not necessarily true). By contrast, an anchoring will be called *approximate* if this relationship is only approximately true (up to some desired tolerance).

Define a *template controller*, $\tau_X : \mathscr{X} \times \mathscr{P}_X \to \mathscr{U}_X$, which may be applied by assigning $u_X = \tau_X(x, p_X)$. Similarly define an *anchor controller*, $\tau_Y : \mathscr{Y} \times \mathscr{P}_Y \to \mathscr{U}_Y$, which may be applied by assigning $u_Y = \tau_Y(y, p_Y)$. The template controller may be pulled back into the anchor via the choice,

$$\tau_Y(y, p_Y) := g^\dagger \circ \tau_X(h(y), \Xi(p_Y)). \tag{1.59}$$

An anchoring will be called *passive* if this is the only control authority exerted on the anchor system. By contrast, an anchoring will be called *active* if there is an additional *anchoring controller*, $\bar{\tau}_Y$, exerted in order to achieve the exact or approximate anchoring, i.e.,

$$u_Y = \tau_Y(y, p_Y) + \bar{\tau}_Y(y, p_Y), \tag{1.60}$$

where $\bar{\tau}_Y$ lies in the null space of g.

In this paper we consider three anchor systems: one that has a passive exact anchoring, one that has a passive approximate anchoring, and one that has an active exact anchoring. For the passive anchors, $\mathscr{X} = \mathscr{Y}$ and $\mathscr{U}_X = \mathscr{U}_Y$ – therefore the maps $h, h^\dagger, g$, and $g^\dagger$ are all identity. The active anchor, through the additional controller, $\bar{\tau}_Y$, restricts down to the template dynamics exactly, and so these maps are similarly uninteresting. Therefore this paper's focus is on the remaining anchoring functions, Ξ and $\Xi^\dagger$, and on the design of the template parameters and controllers to achieve the task.

---

[19] Note that often the control input will be a subset of the cotangent bundle over the state space, $\mathscr{U}_X \subset T^*\mathscr{X}$ and $\mathscr{U}_Y \subset T^*\mathscr{Y}$, i.e. force or torque applied to one or more coordinates. In this case, the control embedding may be related to the state space embedding, $g := \pi_{U,Y}(Dh^\dagger)^T$, i.e. the projection down to the appropriate coordinates of the transpose of the Jacobian of $h^\dagger$.

1.9.2 Alternate template controller formulations

For additional robustness, the template controller may use proportional-derivative (PD) feedback on the body angle (relative to the desired final position, $\theta_{b,f}$, and velocity, $\dot{\theta}_b = 0$). The controller torque takes the form,

$$\tau = K_p(\theta_{b,f} - \theta_b) + K_d(0 - \dot{\theta}_b), \tag{1.61}$$

subject to the limits imposed by the motor model. Given high enough gains, the torque will saturate, producing speed-limited acceleration and current-limited braking as in the switched case; the effective switching time (when $\tau = 0$) depends on the ratio of controller gains.

The ratio of gains that produces the optimal switch is found by examining the point where the acceleration switches signs, i.e. when the terms of (1.61) are equal; plugging in the angle and velocity at the time of switch and applying the spatiotemporal transformation (1.13) yields the ratio for the optimal value of $\tilde{\mathbf{p}}$ (see Appendix 1.9.8 for this derivation). After scaling back to physical torques the optimally-switching gain ratio is,

$$\frac{K_d}{K_p} \approx \frac{0.26}{\gamma} \tag{1.62}$$

Servoing on the internal angle produces an equivalent formulation for the PD controller. In the dimensioned, zero angular momentum template with initial conditions $\theta_b = \theta_r = 0$, the connection field, (1.5) can be integrated to yield $\theta_b = -\xi\theta_r$. Starting with a PD controller servoing the body angle to a desired orientation $\theta_{b,d}$,

$$\begin{aligned} \tau &= K_p(\theta_{b,d} - \theta_b) + K_d(0 - \dot{\theta}_b) \\ &= -K'_p(\theta_{r,d} - \theta_r) - K'_d(0 - \dot{\theta}_r), \end{aligned} \tag{1.63}$$

where $K'_p := \xi K_p$, $K'_d := \xi K_d$, and the desired appendage angle $\theta_{r,d} := -\theta_{b,d}/\xi$. The control torque on the appendage is opposite in sign to the body angle controller as expected.

1.9.3 Dimensionless constraints for current-limited dynamics

If the maximum allowable torque (equivalently motor current) is limited to some factor $\beta \in (0,1)$ less than the stall torque of the motor, $\tau_\ell = \beta\tau_m$, the optimal reorientation consists of three phases: a constant torque phase until the acceleration becomes voltage-limited, then a phase following the speed–torque curve of the motor until the controlled switch at $\tilde{t}_s$, followed by a constant braking torque phase until $\tilde{t}_h$. These dynamics can be integrated to produce a current-limited equivalent to $\mathscr{R}$. Alternatively, equivalent functions to $\tilde{g}_h$ and $\tilde{g}_\theta$ can be used to calculate k_p, k_s and k_t given β and a parameter set $\mathbf{p}$. We provide those equivalent relations here; their full derivations can be found in Appendix 1.9.5,

$$\tilde{g}_h(\tilde{\omega}_m, \tilde{t}_s, \beta) := \tilde{t}_s + \frac{\tilde{\omega}_m^2}{\beta}\left(1 - \beta \exp\left(\frac{-(\tilde{t}_s - \tilde{t}_\ell)}{\tilde{\omega}_m^2}\right)\right) \tag{1.64}$$

$$\begin{aligned}\tilde{g}_\theta(\tilde{\omega}_m, \tilde{t}_s, \beta) :=& \tilde{\omega}_m \tilde{t}_s + \tilde{\omega}_m^3(\beta - 1)\exp\left(\frac{1-\beta}{\beta} - \frac{\tilde{t}_s}{\tilde{\omega}_m^2}\right) \\ &+ \frac{\beta \tilde{\omega}_m^3}{2}\left(1 - \exp\left(\frac{2(1-\beta)}{\beta} - \frac{2\tilde{t}_s}{\tilde{\omega}_m^2}\right)\right).\end{aligned} \tag{1.65}$$

1.9.4 Analytic solution of template dynamics

Integration of the system dynamics, given in (1.8) as,

$$\ddot{\theta}_b = \begin{cases} \frac{4P}{\omega_m I_d}\left(1 - \frac{\dot{\theta}_b}{\xi \omega_m}\right), & \text{for } 0 \le t < t_s, \\ -\frac{4P}{\omega_m I_d}, & \text{for } t \ge t_s. \end{cases}$$

is easier in the rescaled coordinates introduced in (1.13),

$$\tilde{t}_s = \gamma t_s, \quad \tilde{t}_f = \gamma t_f, \quad \tilde{\theta}_h = \frac{\theta_h}{\theta_{b,f}}, \quad \tilde{\omega}_m = \frac{\xi \omega_m}{\gamma \theta_{b,f}}, \tag{1.66}$$

where (1.14),

$$\gamma := \left(\frac{4P\xi}{I_d \theta_{b,f}^2}\right)^{\frac{1}{3}}. \tag{1.67}$$

We will use prime notation instead of a dot to denote time derivatives with respect to $\tilde{t}$, i.e. $()' := d/d\tilde{t}$,

$$\dot{\theta}_b = \gamma \theta_{b,f} \tilde{\theta}_b', \qquad \ddot{\theta}_b = \gamma^2 \theta_{b,f} \tilde{\theta}_b''. \tag{1.68}$$

In the rescaled system, the dynamics are simply,

$$\tilde{\theta}'' = \begin{cases} \frac{1}{\tilde{\omega}_m}\left(1 - \frac{\tilde{\theta}'}{\tilde{\omega}_m}\right), & \text{for } 0 \le \tilde{t} < \tilde{t}_s \\ -\frac{1}{\tilde{\omega}_m}, & \text{for } \tilde{t} \ge \tilde{t}_s. \end{cases} \tag{1.69}$$

Integrating from the initial conditions $\tilde{\theta}'(0) = 0$ and $\tilde{\theta}(0) = 0$ yields the flow over the acceleration phase,

$$\tilde{\theta}'(\tilde{\omega}_m, \tilde{t}) = \tilde{\omega}_m\left(1 - \exp\left(\frac{-\tilde{t}}{\tilde{\omega}_m^2}\right)\right) \tag{1.70}$$

$$\tilde{\theta}(\tilde{\omega}_m, \tilde{t}) = \tilde{\omega}_m \tilde{t} - \tilde{\omega}_m^3\left(1 - \exp\left(\frac{-\tilde{t}}{\tilde{\omega}_m^2}\right)\right), \tag{1.71}$$

for $\tilde{t} < \tilde{t}_s$. The flow over deceleration is,

$$\tilde{\theta}'(\tilde{\omega}_m,\tilde{t}) = \tilde{\theta}'(\tilde{\omega}_m,\tilde{t}_s) - \frac{1}{\tilde{\omega}_m}(\tilde{t}-\tilde{t}_s), \tag{1.72}$$

$$\tilde{\theta}(\tilde{\omega}_m,\tilde{t}) = (\tilde{t}-\tilde{t}_s)\tilde{\theta}'(\tilde{\omega}_m,\tilde{t}_s) - \frac{1}{2\tilde{\omega}_m}(\tilde{t}-\tilde{t}_s)^2 + \tilde{\theta}(\tilde{\omega}_m,\tilde{t}_s,), \tag{1.73}$$

for $\tilde{t} > \tilde{t}_s$. The maneuver ends at a halting time $\tilde{t}_h = \tilde{t}_s + \tilde{t}_r$, when the body comes to rest. The duration of the braking phase, $\tilde{t}_r$, is the zero of (1.72), or equivalently the speed at the switch divided by the braking acceleration $(1/\tilde{\omega}_m)$,

$$\tilde{t}_r = \tilde{\omega}_m\tilde{\theta}'(\tilde{\omega}_m,\tilde{t}_s). \tag{1.74}$$

The final body angle is thus an explicit function of the switching time and $\tilde{\omega}_m$, and can be written out by combining (1.70)–(1.74),

$$\begin{aligned}
\tilde{\theta}_h = \tilde{g}_\theta(\tilde{\omega}_m,\tilde{t}_s) &:= \tilde{\theta}(\tilde{t}_s + \tilde{g}_r(\tilde{\omega}_m,\tilde{\omega}_m,\tilde{t}_s)) \\
&= \tilde{t}_r\tilde{\theta}'(\tilde{\omega}_m,t_s,) - \frac{1}{2\tilde{\omega}_m}\tilde{t}_r^2 + \tilde{\theta}(\tilde{\omega}_m,t_s) \\
&= \frac{\tilde{\omega}_m}{2}(\tilde{\theta}'(\tilde{\omega}_m,t_s))^2 + \tilde{\theta}(\tilde{\omega}_m,t_s) \\
&= \frac{\tilde{\omega}_m}{2}\left(\tilde{\omega}_m - \tilde{\omega}_m \exp\left(\frac{-\tilde{t}_s}{\tilde{\omega}_m^2}\right)\right)^2 \\
&\qquad + \tilde{\omega}_m\tilde{t}_s - \tilde{\omega}_m^3 + \tilde{\omega}_m^3 \exp\left(\frac{-\tilde{t}_s}{\tilde{\omega}_m^2}\right) \\
&= \tilde{\omega}_m\tilde{t}_s - \frac{\tilde{\omega}_m^3}{2}\left(1 - \exp\left(\frac{-2\tilde{t}_s}{\tilde{\omega}_m^2}\right)\right).
\end{aligned} \tag{1.75}$$

The halting time is simply the sum of the switching time and the braking time,

$$\begin{aligned}
\tilde{t}_h = \tilde{g}_h(\tilde{\omega}_m,\tilde{t}_s) &:= \tilde{t}_s + \tilde{t}_r \\
&= \tilde{t}_s + \tilde{\omega}_m^2\left(1 - \exp\left(\frac{-\tilde{t}_s}{\tilde{\omega}_m^2}\right)\right)
\end{aligned} \tag{1.76}$$

Substituting the definitions of the rescaled coordinates, (1.66) and (1.67), into (1.75) and (1.76),

$$t_h = g_h(\mathbf{p}) := \frac{1}{\gamma}\tilde{g}_h\left(\frac{\xi\omega_m}{\gamma\theta_{b,f}}, \gamma t_s\right) \tag{1.77}$$

$$= t_s + \frac{I_b\xi\omega_m^2}{4P}\left(1 - \exp\left(-\frac{4P}{I_b\xi\omega_m^2}t_s\right)\right), \tag{1.78}$$

$$\theta_h = g_\theta(\mathbf{p}) := \theta_{b,f}\tilde{g}_\theta\left(\frac{\xi\omega_m}{\gamma\theta_{b,f}}, \gamma t_s\right) \tag{1.79}$$

$$= \xi\omega_m t_s - \frac{I_b\xi^2\omega_m^3}{8P}\left(1 - \exp\left(-\frac{8P}{I_b\xi\omega_m^2}t_s\right)\right). \tag{1.80}$$

as given in (1.9) and (1.10).

1.9.5 Analytic solution of template dynamics with a current limit

If the maximum allowable torque is limited to some factor $\beta \in (0,1)$ less than the stall torque of the motor, $\tau_\ell = \beta\tau_m$, the optimal reorientation consists of three phases: a constant torque phase until a time $\tilde{t}_\ell$ when the acceleration becomes voltage-limited, then a phase following the speed–torque curve of the motor until the controlled switch at $\tilde{t}_s$, followed by a constant braking torque phase of duration $\tilde{t}_r$ until $\tilde{t}_h$. In this case, the time-switched dynamics of (1.69) become instead,

$$\tilde{\theta}'' = \begin{cases} \frac{\beta}{\tilde{\omega}_m}, & \text{for } 0 \leq \tilde{t} < \tilde{t}_\ell \\ \frac{1}{\tilde{\omega}_m}\left(1 - \frac{\tilde{\theta}'}{\tilde{\omega}_m}\right), & \text{for } \tilde{t}_\ell \leq \tilde{t} < \tilde{t}_s \\ -\frac{\beta}{\tilde{\omega}_m}, & \text{for } \tilde{t} \geq \tilde{t}_s \end{cases} \tag{1.81}$$

The current limited acceleration flow is,

$$\tilde{\theta}'(\tilde{\omega}_m, \tilde{t}, \beta) = \frac{\beta}{\tilde{\omega}_m}\tilde{t}$$

$$\tilde{\theta}(\tilde{\omega}_m, \tilde{t}, \beta) = \frac{\beta}{2\tilde{\omega}_m}\tilde{t}^2 \tag{1.82}$$

for $\tilde{t} < \tilde{t}_\ell$.

The transition to voltage-limited acceleration occurs at a time t_ℓ, when the current-limited torque equals the back-EMF limited torque,

$$\tilde{t}_\ell = \inf\left\{\tilde{t} > 0 \mid \frac{\beta}{\tilde{\omega}_m} = \frac{1}{\tilde{\omega}_m}\left(1 - \frac{\tilde{\theta}'(\tilde{\omega}_m, \tilde{t}, \beta)}{\tilde{\omega}_m}\right)\right\} \tag{1.83}$$

$$= \frac{1-\beta}{\beta}\tilde{\omega}_m^2, \tag{1.84}$$

The transition state is thus an explicit function of β and $\tilde{\omega}_m$,

$$\tilde{\theta}'_\ell := \tilde{\theta}'(\tilde{\omega}_m, \tilde{t}_\ell, \beta) = (1-\beta)\tilde{\omega}_m \tag{1.85}$$

$$\tilde{\theta}_\ell := \tilde{\theta}(\tilde{\omega}_m, \tilde{t}_\ell, \beta) = \frac{(1-\beta)^2}{2\beta}\tilde{\omega}_m^3. \tag{1.86}$$

With these initial conditions, (1.85)–(1.86), the voltage-limited dynamics admit the solution,

$$\tilde{\theta}'(\tilde{\omega}_m,\tilde{t},\beta) = \tilde{\omega}_m\left(1-\beta\exp\left(\frac{-(\tilde{t}-\tilde{t}_\ell)}{\tilde{\omega}_m^2}\right)\right), \tag{1.87}$$

$$\begin{aligned}\tilde{\theta}(\tilde{\omega}_m,\tilde{t},\beta) = {} & \tilde{\theta}_\ell + \tilde{\omega}_m(\tilde{t}-\tilde{t}_\ell)\\ & -\beta\tilde{\omega}_m^3\left(1-\exp\left(\frac{-(\tilde{t}-\tilde{t}_\ell)}{\tilde{\omega}_m^2}\right)\right),\end{aligned} \tag{1.88}$$

for $\tilde{t}_\ell \leq \tilde{t} \leq \tilde{t}_s$. Finally, the flow over deceleration is,

$$\tilde{\theta}'(\tilde{\omega}_m,\tilde{t},\beta) = \tilde{\theta}'(\tilde{\omega}_m,\tilde{t}_s,\beta) - \frac{\beta}{\tilde{\omega}_m}(\tilde{t}-\tilde{t}_s), \tag{1.89}$$

$$\begin{aligned}\tilde{\theta}(\tilde{\omega}_m,\tilde{t},\beta) = {} & \tilde{\theta}(\tilde{\omega}_m,\tilde{t}_s,\beta) + (\tilde{t}-\tilde{t}_s)\tilde{\theta}'(\tilde{\omega}_m,\tilde{t}_s,\beta)\\ & -\frac{\beta}{2\tilde{\omega}_m}(\tilde{t}-\tilde{t}_s)^2,\end{aligned} \tag{1.90}$$

for $\tilde{t} > \tilde{t}_s$. The analysis follows similarly to the previous section, with the return time given by the function,

$$\tilde{t}_r = \tilde{g}_r(\tilde{\omega}_m,\tilde{t}_s,\beta) := \frac{\tilde{\omega}_m}{\beta}\tilde{\theta}'(\tilde{\omega}_m,\tilde{t}_s,\beta), \tag{1.91}$$

the final time given by,

$$\tilde{t}_h = \tilde{g}_h(\tilde{\omega}_m,\tilde{t}_s,\beta) := \tilde{t}_s + \tilde{t}_r \tag{1.92}$$

$$= \tilde{t}_s + \frac{\tilde{\omega}_m^2}{\beta}\left(1-\beta\exp\left(\frac{-(\tilde{t}_s-\tilde{t}_\ell)}{\tilde{\omega}_m^2}\right)\right) \tag{1.93}$$

and the explicit form of $\tilde{g}_\theta$,

$$\tilde{\theta}_h = \tilde{g}_\theta(\tilde{\omega}_m,\tilde{t}_s,\beta) := \tilde{\theta}(\tilde{\omega}_m,\tilde{t}_s+\tilde{g}_r(\tilde{\omega}_m,\tilde{t}_s),\beta) \tag{1.94}$$

$$= \tilde{\theta}(\tilde{\omega}_m,\tilde{t}_s,\beta) + \frac{\tilde{\omega}_m}{2\beta}(\tilde{\theta}'(\tilde{\omega}_m,\tilde{t}_s,\beta))^2 \tag{1.95}$$

$$\begin{aligned} = {} & \tilde{\omega}_m\tilde{t}_s + \tilde{\omega}_m^3(\beta-1)\exp\left(\frac{1-\beta}{\beta}-\frac{\tilde{t}_s}{\tilde{\omega}_m^2}\right)\\ & + \frac{\beta\tilde{\omega}_m^3}{2}\left(1-\exp\left(\frac{2(1-\beta)}{\beta}-\frac{2\tilde{t}_s}{\tilde{\omega}_m^2}\right)\right)\end{aligned} \tag{1.96}$$

Note that if $\tilde{\omega}_m$ is very large, the acceleration will be so slow that the system never reaches the speed-limited phase and the critical switching time $\tilde{t}_c \geq \tilde{t}_\ell$. In this case, the acceleration and braking phases are symmetric with equal durations and $\tilde{t}_h = 2\tilde{t}_s$. The condition for this behavior can be found by taking $\tilde{t}_s = \tilde{t}_\ell$ in (1.95) and is,

$$\tilde{\omega}_m \geq \left(\frac{\beta}{(1-\beta)^2}\right)^{\frac{1}{3}}. \tag{1.97}$$

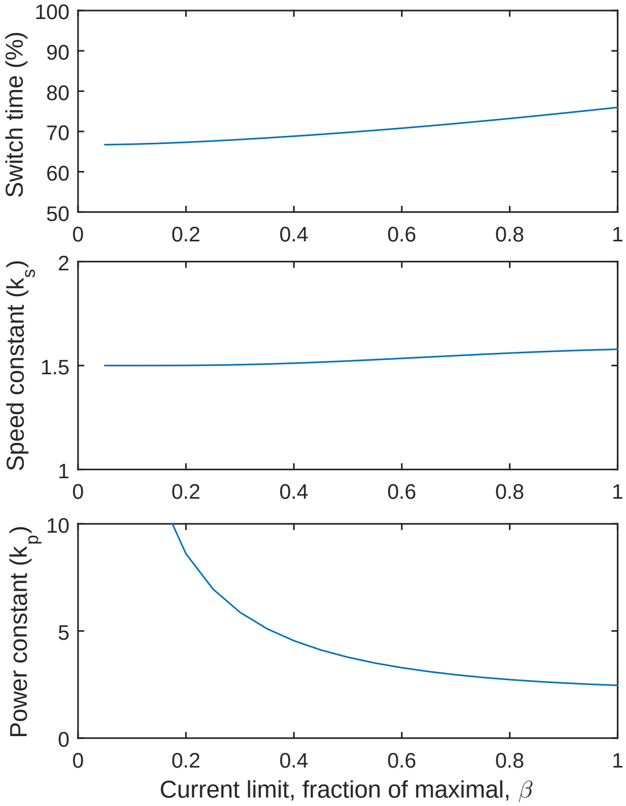

Figure 1.10: Constrained switching time fraction, $\tilde{t}_c/\tilde{t}_f$, no-load speed ratio k_s, and power constant k_p for submaximal current limitation.

The optimal gearing can be found by using the critical switching time, $\tilde{t}_c = \tilde{g}_c(\tilde{\omega}_m)$ and minimizing the final time $\tilde{t}_h = \tilde{g}_\theta(\tilde{\omega}_m, \tilde{g}_c(\tilde{\omega}_m))$, with no constraints on $\tilde{\omega}_m$ other than non-negative real. The halting time $\tilde{t}_h$ varies with β, thus varying the power constant k_p and speed constant k_s, as defined in 1.3.3. Optimal gear ratio is only weakly sensitive to current limit, varying less than 5% over the possible values of β (Fig. 1.10, middle). The required nominal power with the optimal gear ratio grows rapidly with decreasing current limit; limiting torque to 50% increases required nominal power by 53%, while a current limit of 25% nearly triples the required nominal power (Fig. 1.10, bottom).

The current-limited versions of the template behavior, (1.9) and (1.10), can be derived by substituting the definitions of the rescaled coordinates, (1.66), into (1.93) and (1.95) as in the previous subsection.

1.9.6 Alternate controller formulations

1.9.7 Event-based switching

The time-switched bang-bang controller of the previous section can be replaced by an event-based switch or guard condition $G(\tilde{\theta}, \tilde{\theta}') = 0$. For example,

$$G_\theta := \tilde{\theta} - \tilde{\theta}_s, \tag{1.98}$$

where the value of $\tilde{\theta}_s$ is found easily from (1.71) (or (1.88) for the current-limited case). For the optimally geared case with $\beta = 1$, $\tilde{\theta}_s \approx 0.7$; this value changes for suboptimal gearing or $\beta < 1$ (Fig. 1.10, top).

1.9.8 Feedback controllers regulating body angle

For additional robustness, the template controller may use proportional-derivative (PD) feedback on the body angle (relative to the desired final position, $\theta_{b,f}$, and velocity, $\dot{\theta}_b = 0$). The controller torque takes the form,

$$\tau = K_p(\theta_{b,f} - \theta_b) + K_d(0 - \dot{\theta}_b), \tag{1.99}$$

subject to the limits imposed by the motor model. Given high enough gains, the torque will saturate, producing speed-limited acceleration and current-limited braking as in the switched case; the effective switching time (when $\tau = 0$) depends on the ratio of controller gains. Finding the ratio of gains corresponding to a particular value of **p** is easily done in the dimensionless system coordinates. Substituting $\tau = \ddot{\theta}_b / I_d$ and applying the spatiotemporal rescaling of (1.66) to (1.99), the dimensionless closed-loop dynamics are,

$$\theta'' = \tilde{K}_p(1 - \tilde{\theta}) + \tilde{K}_d(0 - \tilde{\theta}'), \tag{1.100}$$

where $\tilde{K}_p = K_p/(\gamma^2 I_d)$ and $\tilde{K}_d = K_d/(\gamma I_d)$. The closed loop dynamics are subject to the motor-imposed acceleration limits,

$$-\frac{\beta}{\tilde{\omega}_m} \leq \tilde{\theta}'' \leq \frac{\beta}{\tilde{\omega}_m}\left(1 - \frac{\tilde{\theta}'}{\tilde{\omega}_m}\right), \tag{1.101}$$

for $\tilde{\theta}' \geq 0$ (the condition for negative body velocity is found by multiplying the inequality by -1, but will never occur during the optimal reorientation).

Substituting expressions (1.70)–(1.71) for the state at the time of switch (where $\theta'' = 0$),

$$\begin{aligned} 0 &= \tilde{K}_p(1 - \tilde{\theta}(\tilde{t}_s, \tilde{\omega}_m)) - \tilde{K}_d \tilde{\theta}'(\tilde{t}_s, \tilde{\omega}_m) \\ \frac{\tilde{K}_d}{\tilde{K}_p} &= \frac{1 - \tilde{\theta}(\tilde{t}_s, \tilde{\omega}_m)}{\tilde{\theta}'(\tilde{t}_s, \tilde{\omega}_m)} \\ \frac{\tilde{K}_d}{\tilde{K}_p} &= \frac{1 - \tilde{\omega}_m \tilde{t}_c + \tilde{\omega}_m^3 \left(1 - \exp\left(\frac{-\tilde{t}_c}{\tilde{\omega}_m^2}\right)\right)}{\tilde{\omega}_m \left(1 - \exp\left(\frac{-\tilde{t}_c}{\tilde{\omega}_m^2}\right)\right)}, \end{aligned} \tag{1.102}$$

for $\beta = 1$ (the expression for the gain ratio follows the above, substituting (1.89)–(1.90) instead). The critical value that produces the optimal switch is found by substituting the optimal no-load speed, $\tilde{\omega}_m^* \approx 0.74$, and corresponding switching time, $\tilde{t}_c^* \approx 1.63$ and has a value of $\tilde{K}_d/\tilde{K}_p \approx 0.26$. For current-limited dynamics, the ratio of gains increases with decreasing β.

When scaling back to physical torques, the gains will scale with I_d and γ as defined above, so the optimal ratio is,

$$\frac{K_d}{K_p} = \frac{\tilde{K}_d}{\gamma \tilde{K}_p} \approx 0.26 \frac{1}{\gamma} \tag{1.103}$$

1.9.9 Derivation of tail connection field

The angular momentum of the system of rigid bodies can be found by adding the angular momentum of each body with respect to some point, O,

$$\mathbf{H_O} = \mathbf{H_{b,O}} + \mathbf{H_{t,O}}.$$

Let $\{\mathbf{E}_1, \mathbf{E}_2\}$ be the world reference frame in the plane, and define $\mathbf{E}_3 := \mathbf{E}_1 \times \mathbf{E}_2$ which exits the page. Let $\mathbf{r}_b$ and $\mathbf{r}_t$ be the position vectors relative to O of the body and tail, respectively (as in Fig. 1.11). Each link's angular momentum is the sum of its angular momentum about its own COM and its moment of linear momentum about O,

$$\mathbf{H_{i,O}} = I_i \dot{\theta}_i \mathbf{E}_3 + \mathbf{r}_i \times m_i \mathbf{v_i},$$

where the subscripts $i \in \{b,t\}$ denote the body and tail, respectively, and $\mathbf{v_i} := \mathbf{v_O} + \dot{\mathbf{r}}_i$ is the absolute velocity of each link. The total angular momentum of the two body system is,

$$\begin{aligned} \mathbf{H_O} &= \mathbf{H_{b,O}} + \mathbf{H_{t,O}} \\ &= (m_b \mathbf{r}_b + m_t \mathbf{r}_t) \times \mathbf{v_O} + \sum_{i \in \{b,t\}} \left(I_i \dot{\theta}_i \mathbf{E}_3 + \mathbf{r}_i \times m_i \dot{\mathbf{r}}_i \right). \end{aligned} \tag{1.104}$$

The centroid of the combined tailed-body mechanism with respect to O, denoted $\mathbf{r}_{com}$, is a weighted sum of the link positions,

$$\mathbf{r}_{com} = \frac{m_b \mathbf{r}_b + m_t \mathbf{r}_t}{m_b + m_t}. \tag{1.105}$$

Note that the first term in (1.104) is eliminated by choosing $\mathbf{r}_{com} = \mathbf{0}$ by placing O at the system COM; in this case, the angular momentum about O is invariant to system velocity.

Let $\{\mathbf{e}_r, \mathbf{e}_s\}$ be an orthonormal reference frame with $\mathbf{e}_r$ aligned with the vector connecting the tail COM to the body COM, and let θ_a be the angle of $\mathbf{e}_r$ with respect to the world reference frame, i.e. the frame is defined by a rotation of θ_a about $\mathbf{E}_3$,

$$\mathbf{e}_r := \cos\theta_a \mathbf{E}_1 + \sin\theta_a \mathbf{E}_2, \tag{1.106}$$

$$\mathbf{e}_s := -\sin\theta_a \mathbf{E}_1 + \cos\theta_a \mathbf{E}_2. \tag{1.107}$$

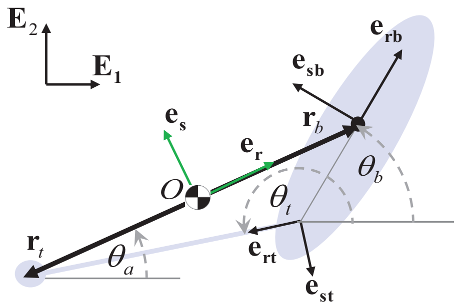

Figure 1.11: Reference frames and coordinates.

This frame enables a simple definition of the vectors from the system COM to the segment COMs,

$$\mathbf{r}_b = r\mathbf{e}_r; \qquad \mathbf{r}_t = -(l-r)\mathbf{e}_r. \tag{1.108}$$

The definition of the center of mass fixes r,

$$-m_t(l-r)+m_b r = 0 \qquad \Rightarrow \qquad r = \frac{m_t}{m_b+m_t} l. \tag{1.109}$$

Hence the body and tail vectors are related by,

$$\mathbf{r}_t = \frac{r-l}{r}\mathbf{r}_b = (1-\frac{m_b+m_t}{m_t})\mathbf{r}_b = -\frac{m_b}{m_t}\mathbf{r}_b. \tag{1.110}$$

We can now simplify (1.104), the expression for total angular momentum,

$$\begin{aligned}\mathbf{H_O} &= (I_b\dot{\theta}_b + I_t\dot{\theta}_t)\mathbf{E}_3 + \mathbf{r}_b \times (m_b\dot{\mathbf{r}}_b) + \mathbf{r}_t \times (m_t\dot{\mathbf{r}}_t) \\ &= (I_b\dot{\theta}_b + I_t\dot{\theta}_t)\mathbf{E}_3 + \left(m_b + \frac{m_b^2}{m_t}\right)\mathbf{r}_b \times \dot{\mathbf{r}}_b. \end{aligned} \tag{1.111}$$

The last term of (1.111) describes the component of angular momentum due to the two point masses orbiting the COM. This cross product, derived below, is always perpendicular to the plane and has a relatively simple expression for its magnitude in terms of the body-fixed reference frame, $\{\mathbf{e}_{rb},\ \mathbf{e}_{sb}\}$, and the tail-fixed reference frame, $\{\mathbf{e}_{rt},\ \mathbf{e}_{st}\}$ (defined analogously to (1.106)–(1.107) as a rotation about $\mathbf{E}_3$ of θ_b and θ_t, respectively).

Equating two expressions for the vector from the pivot to the system COM,

$$\begin{aligned} l_b\mathbf{e}_{rb} - \mathbf{r}_b &= l_t\mathbf{e}_{rt} - \mathbf{r}_t \\ -\frac{m_b+m_t}{m_t}\mathbf{r}_b &= l_t\mathbf{e}_{rt} - l_b\mathbf{e}_{rb} \\ \mathbf{r}_b &= -\frac{m_t}{m_b+m_t}(l_t\mathbf{e}_{rt} - l_b\mathbf{e}_{rb}). \end{aligned} \tag{1.112}$$

The vector $\dot{\mathbf{r}}_b$ follows from time differentiation of $\mathbf{r}_b$,

$$\dot{\mathbf{r}}_b = -\frac{m_t}{m_b+m_t}(l_t\dot{\mathbf{e}}_{rt} - l_b\dot{\mathbf{e}}_{rb}) \tag{1.113}$$

$$= -\frac{m_t}{m_b+m_t}(l_t\dot{\theta}_t\mathbf{e}_{st} - l_b\dot{\theta}_b\mathbf{e}_{sb}). \tag{1.114}$$

Hence the final term in (1.111) becomes,

$$\frac{m_b m_t}{(m_b+m_t)}(l_t\mathbf{e}_{rt} - l_b\mathbf{e}_{rb}) \times (l_t\dot{\theta}_t\mathbf{e}_{st} - l_b\dot{\theta}_b\mathbf{e}_{sb}).$$

The mass coefficient is also known as the reduced mass,

$$m_r := \frac{m_b m_t}{(m_b+m_t)}. \tag{1.115}$$

Using the following identities,

$$(\mathbf{e}_{rt}\times\mathbf{e}_{sb}) = \cos\theta_r\mathbf{E}_3; \ \ (\mathbf{e}_{rb}\times\mathbf{e}_{st}) = \cos\theta_r\mathbf{E}_3, \tag{1.116}$$

we can now evaluate the remaining cross product,

$$\begin{aligned}&(l_t\mathbf{e}_{rt} - l_b\mathbf{e}_{rb}) \times (l_t\dot{\theta}_t\mathbf{e}_{st} - l_b\dot{\theta}_b\mathbf{e}_{sb})\\ &= (l_t^2\dot{\theta}_t - l_bl_t\dot{\theta}_b\cos\theta_r - l_bl_t\dot{\theta}_t\cos\theta_r + l_b^2\dot{\theta}_b)\mathbf{E}_3\\ &= \big((l_t^2 - l_bl_t\cos\theta_r)\dot{\theta}_t + (l_b^2 - l_bl_t\cos\theta_r)\dot{\theta}_b\big)\mathbf{E}_3.\end{aligned}$$

As all terms of $\mathbf{H_O}$ are perpendicular to the plane, we drop the vector notation and simply examine the magnitude of the total angular momentum in this tail anchor, $H_{O,t}$, where $H_{O,t}\mathbf{E}_3 = \mathbf{H}_O$. With the coordinate substitution, $\theta_t = \theta_b + \theta_r$, and the simplification of the cross product,

$$\begin{aligned}H_{O,t} &= (I_b + m_r(l_b^2 - l_bl_t\cos\theta_r))\dot{\theta}_b\\ &\quad + (I_t + m_r(l_t^2 - l_bl_t\cos\theta_r))\dot{\theta}_t\\ &= (I_b + I_t + m_r(l_b^2 + l_t^2 - 2l_bl_t\cos\theta_r))\dot{\theta}_b\\ &\quad + (I_t + m_r(l_t^2 - l_bl_t\cos\theta_r))\dot{\theta}_r,\end{aligned}$$

as stated for the tail template kinematics, (1.30).

1.9.10 Restriction on domain of dimensionless parameters

Because of coupling between the dimensionless constants and the requirement of non-negativity of the dimensioned parameters, only a subset of the dimensionless parameter space is physically realizable. By definition, (1.32), ξ_t is restricted to the interval $[0,1]$, as the denominator is no smaller than the numerator and both are strictly positive. Furthermore, for a given value of ξ_t there is a maximum value of η. Starting with positivity of physical parameters,

$$\begin{aligned} 0 <& I_b I_t + I_b m_r l_t^2 + I_t m_r l_b^2 \\ \frac{m_r^2 l_b^2 l_t^2}{(I_t + m_r l_t^2)^2} <& \frac{I_b I_t + I_b m_r l_t^2 + I_t m_r l_b^2 + m_r^2 l_b^2 l_t^2}{(I_t + m_r l_t^2)^2} \\ \eta^2 <& \frac{1-\xi_t}{\xi_t}, \qquad \eta < \sqrt{\frac{1-\xi_t}{\xi_t}}, \end{aligned} \tag{1.117}$$

that is η is bounded above as shown in gray in 1.5. Another bound used in the paper, ensuring positivity of the denominator of (1.35), may be found by starting with the positivity of physical parameters and of squared values,

$$\begin{aligned} 0 <& \frac{I_b + I_t + m_r(l_b - l_t)^2}{I_b + I_t + m_r(l_b^2 + l_t^2)} \\ 0 <& 1 - \frac{2 m_r l_b l_t}{I_b + I_t + m_r(l_b^2 + l_t^2)}, \qquad 2\xi_t \eta < 1 \end{aligned} \tag{1.118}$$

1.9.11 Integration of the connection field

The total inertial effect of the tail over a given tail sweep, $\theta_r \in [\theta_{r1}, \theta_{r2}]$, is the integral of the connection magnitude $A(\theta_r)$, (1.35), over that stroke range. This integral can be written in closed form by first factoring the connection,

$$\begin{aligned} A(\theta_r) &= \xi \frac{1 - \eta\cos\theta_r}{1 - 2\xi\eta\cos\theta_r} \\ &= \frac{1}{2} \frac{2\xi - 2\xi\eta\cos\theta_r + 1 - 1}{1 - 2\xi\eta\cos\theta_r} \\ &= \frac{1}{2}\left(\frac{2\xi - 1}{1 - 2\xi\eta\cos\theta_r} + 1\right) \\ &= \frac{1}{2} + \frac{2\xi - 1}{4\xi\eta}\frac{1}{a - \cos\theta_r}, \qquad a := \frac{1}{2\xi\eta}. \end{aligned}$$

The change in body angle, $\Delta\theta_b := \theta_{b,f} - \theta_{b,0}$, over a given tail sweep, $\Delta\theta_r := \theta_{r2} - \theta_{r1}$, is then,

$$\Delta\theta_b = -\int_{\theta_{r1}}^{\theta_{r2}} A(\theta_r)\, d\theta_r \tag{1.119}$$

$$= -\frac{\Delta\theta_r}{2} + \frac{1 - 2\xi}{4\xi\eta}\int_{\theta_{r1}}^{\theta_{r2}} \frac{d\theta_r}{a - \cos\theta_r}. \tag{1.120}$$

The remaining integral can be simplified by way of the substitution, $t := \tan\frac{\theta_r}{2}$, and the following identities,

$$\begin{aligned}
2\arctan t &= \theta_r \\
d\theta_r &= \frac{2}{1+t^2}dt \\
\cos\frac{\theta_r}{2} &= \frac{1}{\sqrt{1+t^2}} \\
\sqrt{\frac{1+\cos\theta_r}{2}} &= \frac{1}{\sqrt{1+t^2}} \\
\cos\theta_r &= \frac{2}{1+t^2} - 1 \\
\cos\theta_r &= \frac{2}{1+t^2} - \frac{1+t^2}{1+t^2} \\
\cos\theta_r &= \frac{1-t^2}{1+t^2}.
\end{aligned}$$

Making the substitutions, the integral in (1.120) simplifies to,

$$\begin{aligned}
\int \frac{d\theta_r}{a-\cos\theta_r} &= \int \frac{1}{a-\frac{1-t^2}{1+t^2}} \frac{2}{1+t^2}dt \\
&= \int \frac{2}{a(1+t^2)-(1-t^2)}dt \\
&= \int \frac{2}{(a-1)+(a+1)t^2}dt \\
&= \frac{2}{(a+1)}\int \frac{1}{b^2+t^2}dt, \quad b^2 := \frac{a-1}{a+1} \\
&= \frac{2}{a+1}\left(\frac{1}{b}\arctan\frac{t}{b} + C_1\right) \\
&= \frac{2}{b(a+1)}\arctan\left(\frac{\tan\left(\frac{\theta_r}{2}\right)}{b}\right) + C_2.
\end{aligned}$$

For the sake of space, define the function,

$$\begin{aligned} R(\theta_i) :=& \arctan\left(\frac{\tan\left(\frac{\theta_i}{2}\right)}{b}\right) \\ =& \arctan\left(\sqrt{\frac{a+1}{a-1}}\tan\left(\frac{\theta_i}{2}\right)\right) \\ =& \arctan\left(\sqrt{\frac{1+2\xi\eta}{1-2\xi\eta}}\tan\left(\frac{\theta_i}{2}\right)\right). \end{aligned} \tag{1.121}$$

Returning to the expression for body stroke, (1.120),

$$\Delta\theta_b = -\frac{\Delta\theta_r}{2} + \frac{1-2\xi}{\sqrt{1-(2\xi\eta)^2}}\big(R(\theta_{r2}) - R(\theta_{r1})\big). \tag{1.122}$$

1.9.12 Derivation of equations of motion for a tailed system

Equipped with the kinematic results of 1.3, the balance of angular momentum for a general tailed system about the COM of each body is (see Fig. 1.12),

$$\dot{\mathbf{H}}_b = \tau\mathbf{E}_3 + (-l_b\mathbf{e}_{rb}) \times \mathbf{F}_p, \tag{1.123}$$

$$\dot{\mathbf{H}}_t = -\tau\mathbf{E}_3 + (-l_t\mathbf{e}_{rt}) \times (-\mathbf{F}_p), \tag{1.124}$$

where τ denotes the torque output of the power train, and $\mathbf{F}_p$ is the pin constraint force (see Fig. 1.12). Since both the body and the COM frame are subject to the same gravitational acceleration, the force of gravity does not appear in the pin force, which is simply $\mathbf{F}_p = m_b\ddot{\mathbf{r}}_b$. The body acceleration relative to the COM is found by differentiating (1.114),

$$\ddot{\mathbf{r}}_b = -\frac{m_t}{m_b+m_t}(l_t\ddot{\theta}_t\mathbf{e}_{st} - l_t\dot{\theta}_t^2\mathbf{e}_{rt} - l_b\ddot{\theta}_b\mathbf{e}_{sb} + l_b\dot{\theta}_b^2\mathbf{e}_{rb}).$$

Substituting into (1.123) yields,

$$\begin{aligned} \dot{\mathbf{H}}_b &= \tau\mathbf{E}_3 - l_b\mathbf{e}_{rb} \times m_b\ddot{\mathbf{r}}_b \\ I_b\ddot{\theta}_b\mathbf{E}_3 &= \tau\mathbf{E}_3 + m_r l_b\mathbf{e}_{rb} \times \\ &\quad (l_t\ddot{\theta}_t\mathbf{e}_{st} - l_t\dot{\theta}_t^2\mathbf{e}_{rt} - l_b\ddot{\theta}_b\mathbf{e}_{sb} + l_b\dot{\theta}_b^2\mathbf{e}_{rb}). \end{aligned}$$

Using the identities (1.116) from Section 1.9.9, above, along with

$$(\mathbf{e}_{rb} \times \mathbf{e}_{rt}) = \sin\theta_r\mathbf{E}_3; \tag{1.125}$$

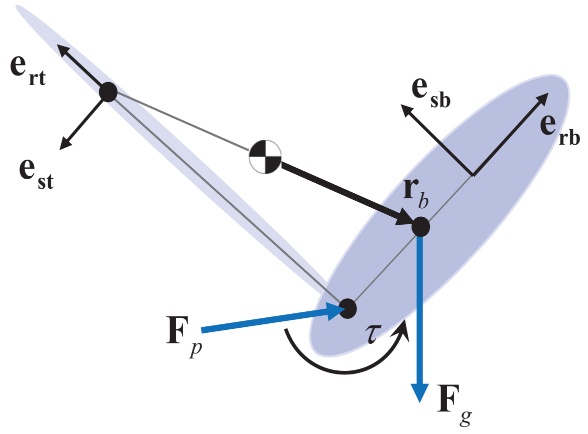

Figure 1.12: Free body diagram for derivation of equations of motion.

to evaluate the cross products, collecting terms and dropping the vector notation (as all terms are aligned with $\mathbf{E}_3$) we arrive at the equation of motion for the body link,

$$(I_b + m_r l_b^2)\;\ddot{\theta}_b = \tau + m_r l_b l_t (\cos\theta_r \ddot{\theta}_t - \sin\theta_r \dot{\theta}_t^2) \tag{1.126}$$

Following the same procedure for the tail,

$$\begin{aligned} \dot{\mathbf{H}}_t &= -\tau\mathbf{E}_3 + l_t\mathbf{e}_{rt} \times m_b\ddot{\mathbf{r}}_b \\ I_t\ddot{\theta}_t\mathbf{E}_3 &= -\tau\mathbf{E}_3 - m_r l_t\mathbf{e}_{rt} \times \\ &\quad (l_t\ddot{\theta}_t\mathbf{e}_{st} - l_t\dot{\theta}_t^2\mathbf{e}_{rt} - l_b\ddot{\theta}_b\mathbf{e}_{sb} + l_b\dot{\theta}_b^2\mathbf{e}_{rb}) \\ (I_t + m_r l_t^2)\ddot{\theta}_t &= -\tau + m_r l_b l_t (\cos\theta_r\ddot{\theta}_b + \sin\theta_r\dot{\theta}_b^2). \end{aligned} \tag{1.127}$$

the equations of motion for the full nonlinear system are,

$$\mathbf{M}(\theta_r)\begin{bmatrix} \ddot{\theta}_b \\ \ddot{\theta}_t \end{bmatrix} + \begin{bmatrix} m_r l_b l_t \sin\theta_r \dot{\theta}_t^2 \\ -m_r l_b l_t \sin\theta_r \dot{\theta}_b^2 \end{bmatrix} = \begin{bmatrix} 1 \\ -1 \end{bmatrix}\tau \tag{1.128}$$

with a mass matrix,

$$\mathbf{M}(\theta_r) = \begin{bmatrix} I_b + m_r l_b^2 & -m_r l_b l_t \cos\theta_r \\ -m_r l_b l_t \cos\theta_r & I_t + m_r l_t^2 \end{bmatrix}, \tag{1.129}$$

as claimed in (1.38) and (1.39).

1.9.13 Nondimensionalization of nonlinear tail dynamics

The equations of motion (1.38) and (1.39) can be written in the generalized coordinates (θ_b, θ_r) by substituting for $\theta_t = \theta_b + \theta_r$ and applying the change of basis to (1.38),

$$\mathbf{M}(\theta_r)\begin{bmatrix} \ddot{\theta}_b \\ \ddot{\theta}_r \end{bmatrix} + \begin{bmatrix} m_r l_b l_t \sin\theta_r(2\dot{\theta}_b\dot{\theta}_r + \dot{\theta}_r^2) \\ -m_r l_b l_t \sin\theta_r \dot{\theta}_b^2 \end{bmatrix} = \begin{bmatrix} 0 \\ -1 \end{bmatrix}\tau, \tag{1.130}$$

with a mass matrix,

$$\mathbf{M}(\theta_r) = \begin{bmatrix} I_b + I_t + m_r(l_t^2 + l_b^2 - 2l_b l_t \cos\theta_r) & I_t + m_r l_t^2 - m_r l_b l_t \cos\theta_r \\ I_t + m_r l_t^2 - m_r l_b l_t \cos\theta_r & I_t + m_r l_t^2 \end{bmatrix}.$$

Following the process of 1.3.2, we substitute the template motor model for the torque and the scaling factors from the template, (1.14), along with a new scaling for the relative angle, $\theta_r' := \dot{\theta}_r/\gamma$ (note that unlike for θ_b, we do not normalize for final position). Normalizing by $\frac{\xi_t}{1-\xi_t}(I_b + m_r l_b^2)$, we define the dimensionless mass matrix,

$$\widetilde{\mathbf{M}}(\theta_r) = \begin{bmatrix} \frac{1-\xi_t}{\xi_t} + 1 - 2\eta\cos\theta_r & 1 - \eta\cos\theta_r \\ 1 - \eta\cos\theta_r & 1 \end{bmatrix},$$

and the dimensionless Coriolis terms,

$$\widetilde{C}(\theta_r, \tilde{\theta}', \theta_r') = \eta\,\theta_{b,f}\sin\theta_r \begin{bmatrix} \frac{2\tilde{\theta}'\theta_r'}{\theta_{b,f}} + (\frac{\theta_r'}{\theta_{b,f}})^2 \\ -(\tilde{\theta}')^2 \end{bmatrix}, \tag{1.131}$$

resulting in dimensionless system dynamics,

$$\mathbf{M}(\tilde{\theta}_r)\begin{bmatrix} \tilde{\theta}'' \\ \frac{1}{\theta_{b,f}}\theta_r'' \end{bmatrix} + \widetilde{C}(\theta_r, \tilde{\theta}', \theta_r') = \begin{bmatrix} 0 \\ -1 \end{bmatrix}\frac{(1-\xi_t)\tilde{\tau}}{\xi_t}, \tag{1.132}$$

with

$$\tilde{\tau} = \frac{1}{\tilde{\omega}_m}\left(1 - \frac{\xi_t\theta_r'}{\theta_{b,f}\tilde{\omega}_m}\right) \tag{1.133}$$

during acceleration, and $\tilde{\tau} = 1/\tilde{\omega}_m$ during braking.

1.9.14 Derivation of the connection for assemblage of limbs

Here we consider a simplified case, where all appendages are parallel (but potentially out of phase by 180°, as in RHex's alternating tripod gait), and the N limbs are arranged with pivots along the centerline of the robot's body (along which the body's COM also falls). Again, the limbs are driven by a high-gain synchronizing control such that all N legs share the same angle θ_t, modulo the phasing noted above.

Using the same reference frames from the tail case, Section 1.9.9, above, let $\mathbf{e}_{rb}$ be the vector parallel to the body axis, and $\mathbf{e}_{rt}$ be the vector to which all limbs are parallel. Denote the vector from body COM to the ith pivot by,

$$\mathbf{p}_i := \ell_i \mathbf{e}_{rb}, \tag{1.134}$$

and the vector from pivot to appendage COM by,

$$\mathbf{t}_i := s_i l_i \mathbf{e}_{rt}, \tag{1.135}$$

where ℓ_i is the position of the pivot along the body (ℓ is negative for pivots behind the body COM), l_i is the length of the ith limb, and $s_i := \pm 1$ is negative for legs out of phase with $\mathbf{e}_{rt}$ by π. The vector from system COM to appendage COM is,

$$\mathbf{r}_i := \mathbf{r}_b + \mathbf{p}_i + \mathbf{t}_i = \mathbf{r}_b + \ell_i \mathbf{e}_{rb} + s_i l_i \mathbf{e}_{rt}, \tag{1.136}$$

and the relation between system COM and segment COMs is,

$$m_{tot}\mathbf{r}_{com} = m_b \mathbf{r}_b + \sum_{i=1}^{N} m_i \mathbf{r}_i, \tag{1.137}$$

where m_i is the mass of the ith appendage, and $m_{tot} := m_b + \sum\limits_{i=1}^{N} m_i$ is the total system mass. Placing the origin at the system COM ($\mathbf{r}_{com} = \mathbf{0}$) and solving for $\mathbf{r}_b$,

$$\mathbf{0} = m_b \mathbf{r}_b + \sum_{i=1}^{N} m_i(\mathbf{r}_b + \ell_i \mathbf{e}_{rb} + s_i l_i \mathbf{e}_{rt}) \tag{1.138}$$

$$m_{tot}\mathbf{r}_b = -\sum_{i=1}^{N} m_i(\ell_i \mathbf{e}_{rb} + s_i l_i \mathbf{e}_{rt}) \tag{1.139}$$

$$\mathbf{r}_b = -\frac{1}{m_{tot}}\left(\mathbf{e}_{rb}\sum_{i=1}^{N} m_i \ell_i + \mathbf{e}_{rt}\sum_{i=1}^{N} m_i s_i l_i\right). \tag{1.140}$$

If $\sum\limits_{i=1}^{N} m_i \ell_i = 0$ (that is, the mass-weighted pivot distances from body COM are symmetric), then $\mathbf{r}_b$ is strictly parallel to $\mathbf{e}_{rt}$,

$$\mathbf{r}_b = c\,\mathbf{e}_{rt}; \qquad c := -\frac{1}{m_{tot}}\sum_{i=1}^{N} m_i s_i l_i, \tag{1.141}$$

and the vector to the ith appendage COM simplifies to,

$$\mathbf{r}_i = \ell_i \mathbf{e}_{rb} + (c + s_i l_i)\mathbf{e}_{rt}. \tag{1.142}$$

The connection can be derived from the total angular momentum; extending (1.104) to multiple appendages,

$$\mathbf{H}_{O,l} = I_b\dot{\theta}_b\mathbf{E}_3 + \mathbf{r}_b \times (m_b\dot{\mathbf{r}}_b) + \sum_{i=1}^{N}\Big(I_i\dot{\theta}_t\mathbf{E}_3 + \mathbf{r}_i \times (m_i\dot{\mathbf{r}}_i)\Big). \tag{1.143}$$

The moment of linear momentum due to the body mass can be simplified using (1.141),

$$\begin{aligned}\mathbf{r}_b \times m_b\dot{\mathbf{r}}_b &= c\,\mathbf{e}_{rt} \times m_b c\,\mathbf{e}_{st}\\ &= m_b c^2\dot{\theta}_t\mathbf{E}_3.\end{aligned}$$

The moment of linear momentum due to each appendage can be simplified using (1.142),

$$\begin{aligned}&\mathbf{r}_i \times m_i\dot{\mathbf{r}}_i\\ &= m_i\Big(\ell_i\mathbf{e}_{rb} + (c+s_il_i)\mathbf{e}_{rt}\Big) \times \Big(\ell_i\dot{\theta}_b\mathbf{e}_{sb} + (c+s_il_i)\dot{\theta}_t\mathbf{e}_{st}\Big)\\ &= m_i\Big(\ell_i^2\dot{\theta}_b + \ell_i(c+s_il_i)(\dot{\theta}_b+\dot{\theta}_t)\cos\theta_r + (c+s_il_i)^2\dot{\theta}_t\Big)\mathbf{E}_3.\end{aligned}$$

With these simplifications, the magnitude of the angular momentum, (1.143), in the $\mathbf{E}_3$ direction, $H_{O,l}\mathbf{E}_3 := \mathbf{H}_{O,l}$, is,

$$\begin{aligned}H_{O,l} = I_b\dot{\theta}_b + m_bc^2\dot{\theta}_t + \sum_{i=1}^{N}\Bigg(I_i\dot{\theta}_t + m_i\Big(\ell_i^2\dot{\theta}_b\\ + (c+s_il_i)^2\dot{\theta}_t + \ell_i(c+s_il_i)(\dot{\theta}_b+\dot{\theta}_t)\cos\theta_r\Big)\Bigg),\end{aligned}$$

where the only remaining configuration dependent term is,

$$\sum_{i=1}^{N} m_i\ell_i(c+s_il_i)(\dot{\theta}_b+\dot{\theta}_t)\cos\theta_r,$$

and hence one criterion for configuration independence is,

$$\sum_{i=1}^{N} m_i\ell_i(c+s_il_i) = 0. \tag{1.144}$$

This is satisfied if all appendages have equal length, l_i, and phase, s_i, (as when all six of XRL's legs share the same angle) and if $\sum_{i=1}^{N} m_i\ell_i = 0$ (as required for the simplification of $\mathbf{r}_b$). Note that if an assemblage of N appendages satisfy this condition, then the addition of an appendage with $\ell_i = 0$ will result in an assemblage of $N+1$ appendages that will satisfy this condition as well.

For limb systems that satisfy (1.144), the magnitude of the angular momentum, (1.143), in the $\mathbf{E}_3$ direction simplifies to,

$$\begin{aligned} H_{O,l} = &\left(I_b + \sum_{i=1}^{N} m_i \ell_i^2\right)\dot{\theta}_b + \\ &\left(m_b c^2 + \sum_{i=1}^{N}\left(I_i + m_i\left(s_i l_i - \frac{\sum_{j=1}^{N} m_j s_j l_j}{m_{tot}}\right)^2\right)\right)\dot{\theta}_t. \end{aligned} \tag{1.145}$$

If, further, all legs have identical mass, length, and inertia, which we will call m_t, l_t and I_t for comparison with the tail anchor, and the pivot locations are symmetric across the body centerline, i.e. $\sum \ell_i = 0$),

$$\begin{aligned} H_{O,l} = &(I_b + m_t \sum_{i=1}^{N} \ell_i^2)\dot{\theta}_b + N I_t \dot{\theta}_t + \\ &m_t l_t^2\left(\frac{m_b m_t}{m_{tot}^2}\left(\sum_{i=1}^{N} s_i\right)^2 + \sum_{i=1}^{N}\left(s_i - \frac{m_t \sum_{j=1}^{N} s_j}{m_{tot}}\right)^2\right)\dot{\theta}_t. \end{aligned} \tag{1.146}$$

To simplify further, assume first that $\sum s_i = 0$,

$$H_{O,l} = (I_b + m_t \sum_{i=1}^{N} \ell_i^2)\dot{\theta}_b + N(I_t + m_t l_t^2)\dot{\theta}_t. \tag{1.147}$$

which, after a change of coordinates to (θ_b, θ_r), is as claimed in (1.51). If instead $\sum s_i = N$,

$$\begin{aligned} H_{O,l} = &(I_b + m_t \sum_{i=1}^{N} \ell_i^2)\dot{\theta}_b + N I_t \dot{\theta}_t + \\ &m_t l_t^2\left(\frac{m_b m_t}{m_{tot}^2} N^2 + \sum_{i=1}^{N}\left(\frac{m_b + N m_t}{m_{tot}} - \frac{m_t N}{m_{tot}}\right)^2\right)\dot{\theta}_t. \end{aligned} \tag{1.148}$$

$$\begin{aligned} = &(I_b + m_t \sum_{i=1}^{N} \ell_i^2)\dot{\theta}_b + N I_t \dot{\theta}_t + \\ &\frac{m_t m_b}{m_{tot}} l_t^2 N\left(\frac{N m_t + m_b}{m_{tot}}\right)\dot{\theta}_t. \end{aligned} \tag{1.149}$$

which, after a change of coordinates to (θ_b, θ_r) and substituting the definition of m_{rt}, is as claimed in (1.52).

g_h, g_θ	Time and angle functions (1.9), (1.10)
$\tilde{g}_h, \tilde{g}_\theta, \tilde{g}_c$	Normalized time and angle functions (1.15), (1.16), (1.18)
H_O	Angular momentum (1.3)
I_a, I_b, I_t	Inertia of the appendage, body, and tail (1.3.1), (1.4.1)
$I_d, I_{d,t}$	Driven inertia of the template and tail (1.3.2), (1.42)–(1.44)
l_b, l_t	Length from the pivot to the body and tail (1.4.1)
k_p, k_t, k_s	Power, time, and speed constants (1.23), (1.3.3)
ℓ_i	Limb offsets (1.4.3)
L	Characteristic body length (1.5.3)
m_b, m_t	Mass of the body and tail (1.4.1)
m_r	Reduced mass (1.31)
N	Number of limbs (1.4.3)
$\mathbf{p} \in \mathscr{P}$	Template parameters (1.2)
$\mathbf{p}_i \in \mathscr{P}_i$	Anchor i parameters (1.29), (1.47), (1.50)
P	Motor power (1.3.2)
$\mathscr{R}, \mathscr{R}^*, \mathscr{R}_i$	Allowable parameter set (1.12), (1.26), (1.28)
s_r	Range of motion (1.3.1)
t, t_s, t_h, t_f	Time, switching, halting and final time (1.3.1), (1.3.3)
$\tilde{t}, \tilde{t}_s, \tilde{t}_c, \tilde{t}_h$	Normalized, switching, critical, and halting time (1.3.3)
γ	Time scaling parameter (1.14)
η	Nonlinearity parameter (1.33)
$\theta_b, \theta_t, \theta_r, \theta_h$	Body, tail, relative, and halting appendage angles (1.3.1)
$\tilde{\theta}$	Normalized relative angle (1.3.3)
ξ, ξ_t	Effectiveness of the template and tail (1.4), (1.32)
ξ_w, ξ_l	Effectiveness of the reaction wheel, and limbs (1.48), (1.53)
Ξ_i	Morphological reduction i (1.27)
τ	Motor torque (1.3.2)
$\omega_m, \tilde{\omega}_m$	Motor and normalized no-load speed (1.3.2), (1.3.3)

Table 1.1: Key symbols used throughout this paper with section or equation number of introduction marked.

Table 1.2: Morphological Reductions for Three Candidate Anchoring Bodies

Attribute	Tail	Reaction wheel	Limbs
Inertial Effectiveness, $\Xi_{i,\xi}$	$\frac{I_t+m_r l_t^2}{I_t+I_b+m_r(l_t^2+l_b^2)}$	$\frac{I_w}{I_w+I_b+m_r l_b^2}$	$\frac{N(I_t+m_k l_t^2)}{I_b+m_t \sum_{i=1}^{N} \ell_i^2+N(I_t+m_k l_t^2)}$
Driven Inertia, Ξ_{i,I_d}	$(I_b+m_r l_b^2)(1-\frac{2\eta}{\pi})$	$I_b+m_r l_b^2$	$I_b+m_t \sum_{i=1}^{N} \ell_i^2$
Anchoring accuracy[9]	Approximate	Exact	Exact

Table 1.3: Comparison of physical properties for limbed or wheeled systems with the capability for aerial reorientation. Unlike the tailed examples, these machines anchor without error.

Attribute	RHex	Cub	Hexbug	Dirt bike
Citation		[27]	[9]	[18]
Number in error figure	12	11	9	10
Appendage Type	Limbs	Limbs	Wheel	Wheel
Body length (cm),L	57	21	5	140
Body mass (g), m_b	7500	1300	40	105×10^{3}
App. mass (g), m_t	63	52	5	10×10^{3}
App. offset (cm), l_b, ℓ_i	25, 0, 25	10, 10	2.5	70
App. length (cm), l_t	10	6.3	0	0
Body inertia (kgm^2), I_b	0.15	9.8×10^{-3}	17×10^{-6}	20
App. inertia (kgm^2), I_t	0.46×10^{-3}	0.14×10^{-3}	12×10^{-6}	0.4
Effectiveness, ξ_ℓ, ξ_w	0.037	0.096	0.38	0.016
Driven inertia (kgm^2), I_d	0.17	0.012	19×10^{-6}	24
Peak motor power (W)	2052	23.3	0.34	33×10^{3}
Range of motion, s_r	360°	180°	360°	360°
App. speed (RPM), ω_m	434	77	916	1200

Table 1.4: Comparison of physical properties for tailed systems with the capability for aerial reorientation.

Attribute	RHex	Tailbot	TaYLRoACH	2DOF Tailbot	Jumper	Kangaroo	Jerboa	Cub
Citation		[2]	[8]	[33]	[7]	[13]	[26]	[27]
Number in error figure	1	2	3	4	5	6	7	8
Body length (cm), L	57	11.7	10	13.5	7.5	46	21	21
Body Mass (g), m_b	8100	160	46	105	25.1	5030	2270	1250
Tail Mass (g), m_t	600	17	4	70	1.4	371	150	310
Tail offset (cm), l_b	8	4.5	5	5.2	1	15.6	3	10
Tail length (cm), l_t	59	10.3	10.2	7.3	6.8	17.7	30	16.8
Body Inertia (kgm^2), I_b	0.15	154×10^{-6}	39.6×10^{-6}	210×10^{-6}	9.3×10^{-6}	0.05	0.025	0.01
Tail Inertia (kgm^2), I_t	0[16]	0[16]	0[16]	479×10^{-6}	6.4×10^{-6}	0.0172	0[16]	875×10^{-6}
Nonlinearity, η	0.136	0.437	0.49	0.227	0.072	0.339	0.1	0.529
Tail effectiveness, ξ_t	0.5587	0.4683	0.4396	0.6848	0.5705	0.3235	0.3351	0.3911
Peak Motor Power (W)	342	4	2.5	1.75	0.257	19	426	5.82
Driven inertia (kgm^2), I_d	0.141	145×10^{-6}	37.2×10^{-6}	283×10^{-6}	9.02×10^{-6}	0.0482	0.0236	0.0092
Range of motion, s_r	172.5°	255°	265°	135°	280°	220°	180°	110°
Tail speed (RPM), ω_m	356	3000	400	320	1000	240	353	77
Error, final angle (1.45)	−1.29%	−1.90%	−1.26%	−4.78%	−0.630%	3.48%	1.48%	0.507%
Error, final time (1.46)	1.20%	3.92%	4.91%	0.105%	0.836%	5.75%	1.94%	6.59%

Chapter 2

Inertial Reorientation in Terrestrial Turning

2.1 Introduction

If locomotion is one of the hallmarks of animals, then maneuvering is what makes motion useful – apart from during migration, animals rarely travel in a straight line for long. Many survival-critical behaviors of animals, including foraging, prey capture and escape, and interspecific competition, depend on maneuverability at least as much as on speed. For terrestrial species, whose movement space is primarily distributed in the horizontal plane, turning is arguably the most important component of maneuverability. Cheetahs, the fastest legged runners, slow down when chasing prey to increase turning rate [55]. Turning is a key feature of aerial [56], aquatic [57], and terrestrial [58] escape responses. Moving through structured or rugged environments like tree canopies, the underbrush, or boulder fields also requires high maneuverability [59, 60]. Despite its importance, the mechanisms that control and stabilize turning remain largely unknown. Maneuverability may also be more sensitive to body form than straight-line performance [61], but aside from general scaling, little is known about how morphology affects turning ability. In this chapter, we reveal how body flexibility may enhance turning ability of lizards, and what role inertial forces might play in the control and stability of maneuvers.

At the most fundamental level, a turn is a reorientation of the body in the horizontal plane plus (optionally) a redirection of linear momentum to coincide with the reorientation. In animals with two [62], four [63], and six [64] legs, the timing and location of foot contacts is important to the production of whole-body torques and forces that rotate the body in concert with the redirection of center of mass (COM) velocity. The external torques generated by these interactions accelerate the body's angular motion and halt it at the conclusion of the turn; therefore the body's polar moment of inertia (MOI) about its COM has been cited as a key performance parameter [61, 64]. However, bodies need not be rigid. Many aquatic locomotors have flexible bodies that greatly enhance turning ability [65]. In the previous chapter, we explored the dynamics, control, and functional morphology of inertial reorientation (IR) – an extreme case of turning where both linear and angular momentum remain static (or zero), and body rotation is due to internal motion. By contrast, the literature on legged turning has focused exclusively on the other extreme, where body internal configuration remains fixed, and the body turns under the influence of external forces. Many runners have significant trunk flexibility, and the more elongate animals (squamates, theropod dinosaurs) predicted to suffer in agility are likely to be the most flexible. How might body flexibility change turning performance? Here we begin to bridge the gap between inertial and impulsive legged maneuverability.

Can terrestrial runners take advantage of IR mechanisms to aid turning when the limbs are in contact with the substrate? If so, what interactions (if any) might occur between core (inertial) and distal (ground reaction) forces? The inertial and impulsive models of previous studies may simply add independently, so that the predictions from that work may be useful in the general setting. Alternatively, environmental forces could reduce, enhance, or eliminate the effect of inertial reorientation (or vice-versa); we extend the IR template of the previous chapter to explore some possibilities in Section 2.2.1. Body shape also affects MOI directly. If these changes are large and timed correctly, actual performance could be far greater than that predicted from rigid-body models; mice transiently reduce their MOI by up to 35% during turns by dorsoventral flexion [63].

Motivated by these questions, and informed by the results of Chapter 1, we hypothesize that at least for more active animals, elongate form need not limit agility. Specifically, we predict that the rigid body assumption of Carrier and others greatly overestimates the role of whole-body inertia in regulating turning performance. We hypothesize that animals with flexible bodies can reduce their inertia dramatically to increase turning speed, and moreover that the same shape change that reduces inertia could be used for inertial reorientation that adds additional performance. We also expect that elongate form enables the recruitment of axial musculature to contribute to the mechanical energy demands of maneuvering. To test these hypotheses, we will observe rapid turns in a lizard known to employ IR mechanisms for orientation control [1], *Agama agama*. We will use planar, rigid body models to estimate the external forces they apply about their COM when executing planar maneuvers, and to make predictions of how their motion would change without body shape change.

In this chapter, we will consider the external forces as lumped into a resultant force/torque pair about the COM; we will consider the role of individual limbs in Chapter 3. Likewise, we will ignore for now the Cartesian motion of the body and focus on the reorientation component of the turn, where body shape change and inertial forces are likeliest to make an impact. The remainder of this chapter is structured as follows. In Section 2.2.1, we will expand on the kinematic and dynamic models of Chapter 1 to find descriptive models that incorporate changing inertia and inertial reorientation into the simple models used previously to describe turning. In Section 2.3 we will introduce the study animal, detail the experiments performed, and explicate the rigid-body chain model used to estimate turning dynamics. In Section 2.4, we will use the models to reveal the contributions of body shape change to planar turns by agamas. In Section 2.5, we will consider implications of both the models and the experimental results for the role of morphology in animal agility and for the design of agile robots, and offer a brief conclusion.

2.2 Models of planar turning

2.2.1 Rigid-body turning

As with any rigid-body rotation, there are an infinite number of rotations that could accomplish a yaw turn; for instance, a 90 degree pitch, followed by a 180 degree roll, followed by a -90 degree pitch would produce a 180 degree turn in the horizontal plane. High-performance fliers including hummingbirds [66] use similar 3D rotations to effect horizontal-plane reorientation during escape responses, and (anecdotally) running mammals may use out-of-plane rotations during rapid head-stand turns [61]. Body shape change may play an even stronger role in these maneuvers, but as a first step, this work will focus on planar rotations, specifically a rotation of the entire body about the vertical axis.

For a body confined to the plane, we can define a turn to be a finite rotation in finite time with zero velocity at the beginning and end of the reorientation (e.g. the reorientation task of Sec. 1.3). A turning rigid body must experience an angular impulse in the direction of the turn, followed by an impulse of equal and opposite direction in order to halt at the end of the maneuver. The maximum angular velocity is simply the first impulse divided by the body's moment of inertia (MOI), and the maximum angular acceleration is the maximum torque normalized by the MOI. This simple model has been used to conclude that all else being equal, turning performance is an inverse function of MOI; therefore compact bodies should be more agile than elongate bodies like those of lizards [61] and dinosaurs [67].

We can use the results of Sec. 1.3 to examine this more closely. When the Inertial Effectiveness, ξ (defined by the ratio of external to internal rotation, (1.4)) is unity, the appendage is stationary during the reorientation; that is, the extreme case of IR is simply rigid-body reorientation (the appendage can be thought of as the substrate). The actuator across the pin joint of the IR template then represents the torque source considered in the simple models used by e.g. [61] (exerted presumably by the sum effect of legs in ground contact). As explored in Sec. 1.3, saturating this torque source with speed captures the essential power limit experienced by all real actuators, including DC motors (for which this linear hybrid model is fairly accurate) and muscles (the force relations of which are far more complex, but are essentially speed-limited in an analogous way). From Sec. 1.3, with $\xi = 1$, the relationship between the fastest possible reorientation, and the actuator power required to produce that reorientation is,

$$\frac{P}{I_d} \geq k_p \frac{\theta_{b,f}^2}{t_f^3}, \tag{2.1}$$

where k_p was a dimensionless power constant equal to approximately 2.5 for the optimal controller and gearing. Leaving aside for now the question of how this model could be anchored to a morphologically-representative body with legs (possibly affecting P and k_p through the gearing effects of jointed limbs), the results of Chapter 1 enable some general predictions regarding the effect of MOI on turning. For a given task, total actuator power must increase linearly with MOI.

For a given rotation with fixed power, the time to complete the maneuver goes as the cube root of inertia. The low exponent of the time scaling means that the 3-5 fold larger inertia of lizards (compared to rodents) noted by [61] could represent only a 40% - 70% increase in reorientation time (again, assuming task, power, and gearing similar for the comparison). While this reduction in performance is much lower than might be naively expected (e.g. by a linear prediction), overall the predictions concur with Walter and Carrier and others in that increased body inertia is detrimental to reorientation performance when the body is forced to remain rigid.

2.2.2 Relaxing the rigid-body assumption

As explored in Chapter 1, real bodies need not be rigid, and there are many potential benefits of changing shape during a maneuver. Any body shape change can induce inertial reorientation, potentially aiding (or obviating the need for) external forces. Shape change could also reduce the body's inertia, increasing acceleration for a given external torque. More subtly, decreasing MOI in the presence of angular momentum can induce additional acceleration even after limbs stop applying torque (as when an ice skater retracts her limbs to increase the rate of a spin). These three mechanisms are well understood in the absence of external forces, but how might they change during legged turning? Further, how can we quantify the effect to which each aspect of body shape change may increase performance relative to a rigid body? In the remainder of this section, we will derive first order models relating turning to external impulse and body shape to measure how IR and changes in inertia increase turning performance over the rigid body model.

2.2.3 First-order models of turning

What predictive or explanatory measurements can we make of an animal performing a turn while changing body shape? Estimating the total core (spine and tail) muscle power and gearing would require a very detailed anatomical model. Likewise, measuring internal torques is not feasible (the axial musculature is distributed in such a way to preclude measurement of individual muscle forces with tendon buckles [68]). Electromyograms could establish the presence of muscle activity [69], but again, without a detailed musculoskeletal model and solid (experimental) understanding of muscle function during real behavior, these measurements alone could not quantify the contribution of body shape change to the observed reorientation. Here we introduce first-order (velocity) models that predict body rotation from observations of angular momentum and shape change. These models can link morphology with impulse to describe how internal and external torques affect a reorientation, and can be informed by kinematic measurements, which are more easily collected than internal force measurements. The trade-off is that these models consider angular momentum to be a fixed time series and therefore do not account for changes in external forces with motion. They are therefore descriptive rather than predictive.

When turning with a completely rigid body (assuming legs of negligible mass), the turn is related to the impulse in a simple way:

$$\theta_{b,f} = \int_{t_0}^{t_f} \dot{\theta}_b(t) = \frac{1}{I_r} \int_{t_0}^{t_f} H(t) \tag{2.2}$$

Thus for a single rigid body, turning angle is inversely proportional to inertia if external impulse is fixed. We can estimate the moment of inertia of a turning animal from the observed rotation and observed impulse (angular momentum) as $\hat{I}_r = (\int_{t_0}^{t_f} H(t))/\theta_{b,f}$. Performing the same calculation on a non-rigid body undergoing a turn provides a simple means of comparison; if the effective inertia is close to a measurement of the animal's actual inertia as a rigid body, the rigid body approximation is reasonable. We will make this calculation for agamas during a turn in Sec. 2.4.1.

2.2.4 Variable body inertia

As a generalization of the single rigid body model, consider a set of interconnected rigid bodies (approximating the distribution of mass over the body of an animal or robot). The total angular momentum of the N bodies about the system's center of mass O is the sum of the angular momentum of each link about its center of mass, plus the moment of its linear momentum about the system COM:

$$H_0\mathbf{E}_3 = \sum_{i=1}^{N} \left(I_i \dot{\theta}_i \mathbf{E}_3 + \mathbf{r}_i \times (m_i \dot{\mathbf{r}}_i) \right) \tag{2.3}$$

where $\mathbf{E}_3 = \mathbf{E}_1 \times \mathbf{E}_2$ is the Cartesian basis vector exiting the horizontal plane, and $\mathbf{r}_i$ are the position vectors from the system COM to the COM of each link. The position vectors can be writen in cylindrical polar coordinates as $\mathbf{r}_i = \rho_i \mathbf{e}_{ri}$, defining the basis vectors,

$$\mathbf{e}_{ri} = \cos\psi_i \mathbf{E}_1 + \sin\psi_i \mathbf{E}_2.$$

where ρ_i is the distance from system COM to ith segment COM, and ψ_i is the angle of the ith position vector relative to $\mathbf{E}_1$. The angular momentum is parallel to $\mathbf{E}_3$; H_0 simplifies to,

$$H_0 = \sum_{i=1}^{N} \left(I_i \dot{\theta}_i + m_i \rho_i^2 \dot{\psi}_i \right)$$

The condition for rigid-body rotation is that all body angular velocities are identical, e.g.

$$\dot{\theta}_i = \dot{\phi}_i := \dot{\theta}_b.$$

and $\dot{\rho}_i = 0$ for all i. The moment of inertia of this rigid body about its center of mass is

$$I_c = \sum_{i=1}^{N} \left(I_i + m_i \rho_i^2 \right)$$

If no relative angular motion is allowed, but the radial motion is permitted, the moment of inertia can vary without inducing inertial reorientation as defined in Chapter 1. The angular velocity of this body, $\dot{\theta}_b(t)$, is simply a function of its angular momentum and instantaneous moment of inertia (which may vary with ρ). The angle of the body (the remaining rotational degree of freedom) can be found from the impulse and the (changing) moment of inertia by

$$\theta_{b,f} = \int_{t_0}^{t_f} \dot{\theta}_b(t) = \int_{t_0}^{t_f} \frac{H(t)}{I_c(t)} \tag{2.4}$$

where angular momentum and the radial COM positions ρ_i are given as functions of time.

This formulation makes clear that (1) the body only moves through the action of external impulses (if $H = 0$ the body does not rotate regardless of the radial velocities $\dot{\rho}_i$), and (2) in the presence of angular momentum, a reduction in I_c (through a change in radial mass position ρ_i) causes additional angular acceleration. This is distinct from inertial reorientation in the sense that mass motion is purely radial, and zero angular momentum reorientation is impossible.

It is important to note that (2.4) does not reveal the mechanism by which the body changes shape, only the effect of that shape change on the orientation of the body given the external impulses (momentum). For instance, the bodies could move apart ($\dot{\rho}_i > 0$) passively (e.g. without actuation to provide centripetal acceleration) or through the action of external moments rather than internal torques. What this model does provide is a quantification of the effect of MOI changes on the external impulse required to turn a body. In Sec. 2.4.1 we will use (2.4) to estimate the increase in the agama's turning performance afforded by variable MOI relative to a fixed body.

2.2.5 Multi-link chain model of Agama

Since agamas and other lizards have high lateral flexibility, we will generalize the two-link body-tail model from Chapter 1 into an N-link chain. Starting as before from (2.3), we can write the vectors $\mathbf{r}_i$ by referencing from the anterior tip of the animal (see Fig. 2.1) and following the body-fixed basis vectors $\mathbf{e}_1 \ldots \mathbf{e}_N$ along the chain,

$$\mathbf{r}_i = \mathbf{r}_0 - \sum_{k=1}^{i-1} l_k \mathbf{e}_{rk} - s_i \mathbf{e}_{ri},$$

where l_i and s_i denote the length and COM position of the ith segment. Note that the body-fixed basis vectors are strictly a function of the absolute orientation of the links:

$$\mathbf{e}_i = \cos\theta_i \mathbf{E}_1 + \sin\theta_i \mathbf{E}_2.$$

Now to write the position vector as a function of the orientation of the chain, we need only find r_0, which follows from the definition of the center of mass:

$$\left(\sum_{i=1}^{N} m_i\right) \mathbf{d}_c = \sum_{i=1}^{N} m_i \mathbf{r}_i,$$

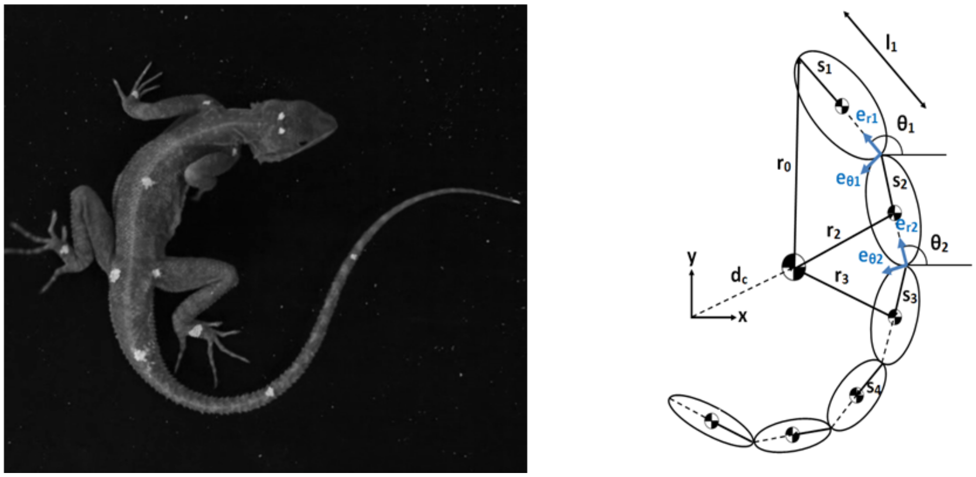

Figure 2.1: Animal and rigid-body representation.

where in this case the distance to the center of mass d_c is by definition zero. Hence,

$$0 = \sum_{i=1}^{N} m_i \left(\mathbf{r}_0 - \sum_{k=1}^{i-1} l_k \mathbf{e}_{rk} - s_i \mathbf{e}_{ri} \right)$$

and we can solve for the desired quantity,

$$\mathbf{r}_0 = \frac{1}{m_t} \sum_{i=1}^{N} \left(s_i m_i \mathbf{e}_{ri} + m_i \sum_{k=1}^{i-1} l_k \mathbf{e}_{rk} \right); \qquad m_t = \sum_{i=1}^{N} m_i$$

Hence the position vector for each link can be written in terms of the absolute orientation of the animal:

$$\mathbf{r}_i = \frac{1}{m_t} \sum_{j=1}^{N} \left(s_j m_j \mathbf{e}_{rj} + m_j \sum_{k=1}^{i-1} l_k \mathbf{e}_{rk} \right) - \sum_{k=1}^{i-1} l_k \mathbf{e}_{rk} - s_i \mathbf{e}_{ri} = \sum_{j=1}^{N} r_{ij} \mathbf{e}_{rj}.$$

The velocity of each link is simply the time derivative of the position vector:

$$\mathbf{v}_i = \frac{d\mathbf{r}_i}{dt} = \frac{1}{m_t} \sum_{j=1}^{N} \left(s_j m_j \dot{\theta}_j \mathbf{e}_{\theta j} + m_j \sum_{k=1}^{i-1} l_k \dot{\theta}_i \mathbf{e}_{\theta k} \right) - \sum_{k=1}^{i-1} l_k \dot{\theta}_i \mathbf{e}_{\theta k} - s_i \dot{\theta}_i \mathbf{e}_{\theta i}, = \sum_{j=1}^{N} r_{ij} \dot{\theta}_j \mathbf{e}_{\theta j}$$

where we used the time derivative of the body-fixed vector,

$$\frac{d\mathbf{e}_{ri}}{dt} = \dot{\theta}_i (-\sin\theta_i \mathbf{E}_1 + \cos\theta_i \mathbf{E}_2) = \dot{\theta}_i \mathbf{e}_{\theta i}$$

It should be clear from the definitions of the position and velocity vectors that the cross products in the total angular momentum depend only on the constants r_{ij}, the segment velocities $\dot{\theta}_i$ and the cross products $\mathbf{e}_{ri} \times \mathbf{e}_{\theta j} = \cos(\theta_i - \theta_j)\mathbf{E}_3$, where $i, j = 1 \ldots N$. Dropping the vector notation, since clearly the only component is out of the plane, the total angular momentum can be written simply as

$$H_0 = \sum_{i=1}^{N} \left(c_i \dot{\theta}_i\right),$$

where $c_i = C_i(\theta_i - \theta_j)$ are configuration-dependent coefficients comprised of I_i, r_{ij}, and $\cos(\theta_i - \theta_j)$. To make explicit the effect of the changing shape on the total orientation of the animal, we introduce the coordinate change

$$\phi_i = \theta_i - \theta_1; \qquad i = 2 \ldots N,$$

where we will refer to ϕ_i as the shape angles. Substituting the shape angles and their derivatives into the angular momentum yields

$$\begin{aligned} H_0 &= c_1 \dot{\theta}_1 + c_2(\dot{\theta}_1 + \dot{\phi}_2) + \ldots + c_N(\dot{\theta}_1 + \dot{\phi}_N) \\ H_0 &= \sum_{i=1}^{N} (c_i)\, \dot{\theta}_1 + \sum_{i=2}^{N} (c_i)\, \dot{\phi}_i \\ H_0 &= I_c \dot{\theta}_1 + \sum_{i=2}^{N} \left(c_i \dot{\phi}_i\right), \end{aligned}$$

where $c_i = C_i(\phi_i)$ are configuration-dependent coefficients, and $I_c = I_c(\phi_i)$ is the instantaneous moment of inertia of the entire animal about its COM. Intuitively, if the shape is constant ($\dot{\phi}_i = 0$), the angular momentum is simply that of the rigid animal spinning about its COM at a constant rate.

Rearranging terms to solve for the instantaneous turning rate yields the equivalent of (1.4) from Chapter 1,

$$\dot{\theta}_1(t) = \frac{H_0(t)}{I_c} - \frac{1}{I_c} \sum_{i=2}^{N} \left(c_i \dot{\phi}_i\right).$$

and integrating this expression yields the equivalent of (2.4) with inertial reorientation,

$$\theta_{b,f} = \int_{t_0}^{t_f} \dot{\theta}_1(t) = \int_{t_0}^{t_f} \frac{H_0(t)}{I_c} - \int_{t_0}^{t_f} \frac{1}{I_c} \sum_{i=2}^{N} \left(c_i \dot{\phi}_i\right).$$

This formulation decomposes the body angular velocity into a component representing the rate at which the whole body would rotate without internal rotation, plus the inertial reorientation of the same body undergoing the observed shape change. Again, this is not a complete causal model of the mechanics of turning, but should instead be viewed as more detailed expression of (2.2): a measure of how external impulses (the integral of torques) are filtered through body inertia (and now, added to body shape change) to produce reorientation. In the absence of angular momentum ($H = 0$), the model reduces to the local connection vector field of [42]. Hatton and others have explored geometric methods for finding trajectories through the shape space $(\phi) := [\phi_1 \ldots \phi_N]^T$ that maximize body rotation.

2.2.6 Inertial reorientation with external forces

In the presence of external forces, $H \neq 0$ and all three mechanisms (impulse, MOI change, and inertial reorientation) come into play. Intriguingly, (2.2.5) states that the total rotation is simply the sum of the impulsive model, (2.4) and the zero angular momentum IR model. Since (2.2.5) is not a causal model, it cannot answer the question of how inertial reorientation and impulse might interact, but it is worth considering some possibilities. To do so, we will augment the IR template from Chapter 1 with external forces.

Consider the inertial reorientation template augmented with N_i external forces, $F_{i,j}$, applied to applied to body i. The external forces exert a total moment about the center of mass of each link, $\tau_{e,b}$ for the body, and $\tau_{e,a}$ for the appendage in addition to the internal torque, τ_s, of the IR template (the s denoting shape change). The acceleration of the body can be written by differentiating (1.4),

$$\ddot{\theta}_b = \frac{\dot{H}_O}{I_a + I_c} - \xi \ddot{\theta}_r \tag{2.5}$$

By Euler's laws, $\dot{H}_O = \tau_{e,a} + \tau_{e,b}$. The component due to shape acceleration is due to a combination of internal torque and external forces,

$$\begin{aligned}
\ddot{\theta}_r &= \ddot{\theta}_t - \ddot{\theta}_b \\
&= \frac{\tau_{e,a} - \tau_s}{I_a} - \frac{\tau_{e,b} + \tau_s}{I_b} \\
&= \frac{\tau_{e,a} - \tau_s}{\xi I_c} - \frac{\tau_{e,b} + \tau_s}{(1-\xi) I_c} \\
&= \frac{\tau_{e,a}}{\xi I_c} - \frac{\tau_{e,b}}{(1-\xi)} - \frac{1}{\xi(1-\xi)} \tau_s
\end{aligned} \tag{2.6}$$

In general, we cannot distinguish between internal torque and externally-driven shape change from observations of H and θ_r. As noted earlier, measurement of internal forces (τ) is extremely difficult, although we could estimate them if we had complete measurements of all external forces. If external forces are state-independent and applied in the inertial frame (so that external torque is not affected by body shape change), and shape change is insensitive to external forces (either due to geometry, or the action of high physical or closed-loop stiffness), then the combined inertial + impulsive maneuver would simply be the linear superposition of the impulsive and inertial models. More realistically, external forces will exert moments about internal joints, and thus affect the changing shape of the body [point to the term in the template math]. Thus, when observing a maneuver in which (2.4) predicts shape change plays a large role in reorientation, some or even all of that reorientation could come from passive body shape change (in the extreme, $\tau = 0$) rather than inertial reorientation in the sense of Chapter 1. The shape change prediction of the inertial model should be therefore treated as an upper bound of the effect of inertial forces. In Sec 2.4.2, we will attempt to test this upper bound for the turning agamas by reducing external forces and observing changes in shape-induced rotation.

How is the possibility of inertial reorientation affected by external forces that are not state-independent? The answer invariably depends on the nature of the coupling to the environment. In one extreme, legs could be extremely stiff (e.g. non-backdrivable servos) and strongly adhered to the substrate (e.g. feet with interlocking or high friction); body rotation in this case would likely be completely dominated by actuator mechanics. Inertial reorientation in the sense of Chapter 1 would be impossible because internal shape change would simply induce reaction forces at the feet (though decreasing inertia could still be helpful). The inertial reaction forces at the feet would be in the same direction as the appendage motion; that is, they would result in angular impulse about the COM in the opposite direction of the motion that would have been induced had inertial reorientation been successful.

When foot-substrate friction is reduced, inertial forces could cause the feet to lose traction and slide if legs are sufficiently stiff; this case has been explored extensively in legged robots [8, 9, 70] and inertial reorientation successfully induced turning, with the feet producing parasitic drag so the resulting reorientation was lower than predicted by a model that neglected external forces. Kohut et al. used this strategy to steer the robot TaYLRoaCH during forward locomotion with good tracking performance on smooth substrates [8], but rougher terrain produced uncontrollable perturbations as intermittent bouts of high traction caused the IR controller to produce large impulses counter to the direction of desired turning (personal communication, Kohut). The smaller Hexbug experienced unpredictable counterrotation after the end of inertial reorientation [9]. Successful control of IR with stiff legs and (intermittently) high traction contact would require fast, reliable sensing of contact condition, as the effect of relative appendage motion changes between the sliding condition (IR with drag, as in TaYLRoaCH) and the sticking condition (reaction forces producing impulse counter to the appendage motion). The sensorimotor delay of animals [71] would likely preclude such a strategy for high-tempo locomotion.

With more compliant or backdrivable limbs and spine, interactions between body shape and external forces could be constructive or only mildly destructive. Torques in the spine could be augmented by external torques (τ_s and τ_e same sign). Inertially-driven body rotation may reduce or enhance muscle forces (by changing $\dot{\theta}_b$, and therefore limb speed), but without the high-stiffness interactions observed in TaYLRoaCH. The limbs of animals are more compliant and backdrivable than those of spring-legged robots like RHex and TaYLRoaCH (inspiring the present vogue in direct-drive robotics [26, 50]. Further, mechanisms like swing-leg retraction [72] reduce the possibility of jamming interactions when inertial reorientation might cause a leg to contact the surface prematurely.

We will probe the interactions between inertial forces, external forces, shape change, and reorientation in three ways. First, in Section 2.4.2, we will look for apparent inertial reorientation accompanied by external impulses opposing the direction of IR (suggesting drag/jamming interactions similar to those found in TaYLRoaCH). Second, in Section 2.4.2, we will compare the work done by limbs to average changes in total kinetic energy to measure any additional work done by the spine. Third, in section 2.4.2, we will compare measured limb velocity to a prediction of speed based on rigid rotation/translation of the whole body, thereby examining the possible effect on muscle velocities due to shape change.

2.3 Methods

2.3.1 Model system

Lizards, *Agama agama*, were acquired from a commercial pet vendor (reptilesncritters.com) and group housed in large tanks (3 individuals per tank) with a rocky and sandy substrate. Animals were kept in an environmentally controlled room ($25 \pm 2^{\circ}$ C; relative humidity, 27%) with 12-h light-dark cycles and fed a diet of water and crickets. The Animal Care and Use Committee at the University of California, Berkeley, whose activities are mandated by the US Animal Welfare Act and Public Health Service Policy, approved all experimental procedures. The animals were hand fed individually, twice per week. To facilitate data collection, we trained lizards to hand feed. Since individuals were initially startled by the feeder's movement, we started with static presentations in forceps, and slowly progressed to tossing the cricket away from the agama at increasing distances. After weeks of training, most individuals aggressively chased both the forceps and the cricket, and were no longer averse to the hand movements of the trainers. At this point, we could use prey capture behaviors to reliably elicit produce high-effort, directed locomotor behavior.

2.3.2 Experiments

Lizards performed planar maneuvers on a flat acrylic platform (30 *cm* by 45 *cm*) covered in high-traction paint. The platform was raised above the floor and a 10 *cm* by 10 *cm* cutout provided space for a 6-axis force transducer (ATI Nano 17) with an acrylic top plate (force platform), mounted flush to the acrylic platform. The floor of the tank was filled with sand such that the acrylic platform and force plate were flush to the sand surface. Agamas were marked with non-toxic white paint at regular intervals along the dorsal surface (Fig. 2.2).

During experiments, animals were fed twice per week as in training. The experimenter presented a cricket in 30 *cm*-long forceps above the acrylic platform. When the agama approached the forceps, the experimenter manipulated its location to isolate one foot on top of the force platform. The experimenter then threw the cricket behind the lizard, aiming for a location directly anterior and approximately 50 *cm* behind the lizard's COM. Crickets thrown too far did not elicit a full response, as agamas lost visual contact after the onset of turning. Overly close throws resulted in low-speed runs. These trials were later culled by our trial definition (Sec. 2.3.6).

2.3.3 Measurements

Maneuvers were filmed from above at 1.3 megapixel, 500 frames per second (Fastec HiSpec 1). Images were post-corrected for parallax and distortion in MATLAB. The positions of the dorsal white markers were digitized (Xcitex ProAnalyst) and exported for further analysis in MATLAB. The position of each foot was manually digitized when touchdown and liftoff events occurred. Foot position was defined at the metatarsal- (or metacarpal-) phalangeal joint between the second and third digit, and touchdown and liftoff were defined by the contact condition of this point. Analog force data were acquired and digitized (National Instruments USB-6251) with custom MATLAB software.

2.3.4 Rigid-body model and morphometrics

The N-link rigid-body model of the agama (Fig. 2.1) was fit to the marker location data, providing estimates of COM locations for each of the rigid bodies, and the location of the animal's COM. We followed the approach in [1], but increased the number of bodies to six (two for the body and four for the tail), accounting for the greater flexibility of the spine in the dorsal plane compared to the sagittal plane of the earlier study.

We developed a morphometric model from cadavers to estimate the inertial properties of each rigid body on the study animals. The four tail segments were each modeled by an elliptical frustum [73, 74]. We modeled the body (from vent to snout) by two rigid bodies; the more complex morphology of the anterior segments precluded representation by any simple parametric solid, so we generated a parametric model from data.

Seven cadavers were cut into the six segments described by the rigid-body model and deep frozen ($48 \pm 22g$ on average). For each tail segment, we measured width and height of the segment at the proximal and distal end, along with the overall length. The torso was sectioned halfway between the pelvis and the shoulder girdle. For each body segment, we measured length (from vent to cut, and cut to anterior tip for posterior and anterior, respectively) and dorsoventral thickness at the cut. We pinned the proximal limb segments at 90 to the fore-aft axis and measured the distance between left and right knees and left and right elbows. Measurements are summarized in Fig. 2.2. We found the horizontal plane COM and MOI about the COM of each segment using the knife-edge method and single pendulum method, respectively (following [75]).

The morphometric model for the torso segments assumed isometric scaling between individuals. The mass of the anterior and posterior torso segments were thus estimated as a constant 41% and 38% of body mass, respectively (mean of seven cadavers, std. dev. 1.9% and 2.9%, respectively). The COMs of the anterior and posterior torso segments were estimated as a constant 57% and 53% of the distance from the posterior to anterior end of the segment (mean of seven cadavers, std. dev. 6% and 10%, respectively). The MOIs of each segment were estimated as $I_i = p_i m_i l_i^2$, where l_i was the taken as overall segment length for the anterior segment and knee-to-knee width for the posterior segment, m_i was estimated from total body mass as described above, and p_i were coefficients fit from linear regression of cadaver data ($p_i = 0.08$ for anterior and $p_i = 0.11$ for posterior). Using terms for length and width for both segments did not improve error.

The morphometric model for the tail segments assumed constant tail density (1200 kg/m^3, measured by calculating approximate volume by water displacement) and an elliptical frustum shape for each segment. We estimated the mass, COM position, and MOI about mass center for each tail segment by a parametric model [73] and verified the model predictions in Solidworks. Over the seven cadavers, median model error was 2.5% for total body mass (due to frustum estimation of tail segments), 7.8% for COM location, and 8.6% for MOI.

Figure 2.2: Weekly morphometric measurements for an agama. The individual is weighed, and dorsoventral thickness measured by caliper at each marker point along the tail. Colored circles mark locations of points used to inform morphometric models. We used the line between the shoulder markers and hip markers to define the average body heading. The line between the point midway along the torso and hip or shoulder markers was used to define the angle of hip and shoulder girdles, respectively.

2.3.5 Rigid-body model predictions

To apply the model to living animals, we measured external morphometrics on each subject weekly. We measured total body mass, and took overhead photos of each animal. We used calipers to measure the major and minor axes of each tail segment from vent to tip at each marker. Markers were freshly painted weekly. Overhead photos were digitized to measure the distance between markers, width of each tail segment, and knee-knee and elbow-elbow distance (Fig. 2.2). These data were used as inputs to the morphometric model to generate the rigid-body model for any experimental trials in the seven days closest to the day of measurement.

We used the morphometric model in concert with the digitized kinematics to calculate the positions and orientations of the six links of the model. Segment COM positions and angles were filtered (5th order Butterworth, 40 Hz low-pass) and numerically differentiated to estimate linear and angular velocity. Angular momentum of each segment was estimated by (2.3), with total angular momentum estimated as the sum of segment momentum for all segments. Linear momentum was estimated by the product of segment mass and segment velocity.

2.3.6 Trial inclusion and cropping

We defined body heading by the angle of line between the shoulder markers and those on the pelvic girdle (Fig. 2.2). We chose trials in which the prey item landed such that Agamas needed to rotate at least 150° to intercept, and far enough away that COM speed reached at least 70 cm/s. We further culled trials that displayed pauses in rotation or acceleration towards the prey; agamas appeared to lose visual contact with the target in these trials, resulting in two or more sub-movements where the animal turned and accelerated or decelerated. Our chosen field of view did not permit observation of the prey target's final location in all trials. Agamas typically slowed before capturing prey if they lost visual contact or if the prey escaped. Since behavior after the acceleration phase was highly variable in timing and degree of braking, we trimmed trials at the point of the first velocity peak subsequently followed by a reduction of speed by at least 25 cm/s. We treated left and right turns as equivalent; in the subsequent analysis, we mirrored right turns and rotated the coordinate axes to align with the initial torso angle, so that all trials could be compared directly.

2.3.7 Alignment and averaging

To best characterize the typical maneuver, we averaged individual kinematic trajectories after aligning them in time. Since the initial body rotation was roughly linear in time from 30 to 90 degrees, we fit a linear relationship to this portion of the angle trajectory and used the time-intercept as the common alignment for every trial. This method aligned individual trials better than attempts to use changes in linear or angular velocity to trigger the beginning of motion; those methods were more sensitive to video noise or movements of the animal's head or tail tip. Foot forces indicated that acceleration began slightly earlier on average than the zero found by this method; for consistency, we defined $t = 0$ as 40 ms before the time-intercept found by linear fit (so that on average, torque about the COM was 10% of peak at $t = 0$).

After temporal alignment, we resampled the trajectories (by linear interpolation at the same sample rate) and found the mean signal at each new time sample across all trials, along with a 95% confidence interval for the mean trajectory (± one standard error, calculated at each sample).

2.4 Results

We observed 83 turns from three individuals. Agamas began at rest, with all limbs contacting the substrate. We did not find significant differences in task performance across individual, so we lumped data from all trials together in the following. Shortly after prey stimulus presentation, they initiated turning by pushing laterally with the forelimbs and applying twisting forces with

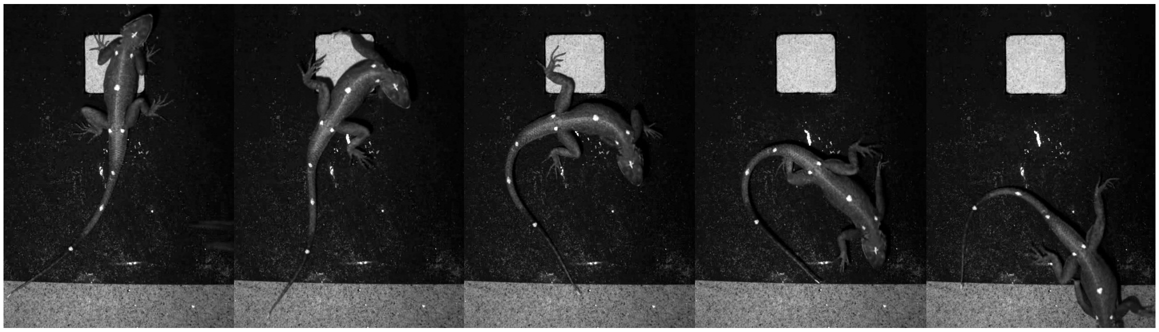

Figure 2.3: Stills from a typical turn (top view). The prey stimulus was presented directly behind the animal (figure bottom). The light-colored square is the top plate of the force platform.

the hindlimbs (for a more complete treatment of the function of individual limbs, see Chapter 3). Agamas took 2-3 strides to complete the turn and transition to straight running (Fig. 2.3). Maximum turn angles were 175° on average (Fig. 2.5; animals typically took about 250 *ms* to complete the maneuver inclusion criteria (150° rotation and 70 cm/s). As predicted, the body changed shape considerably, with the tail swinging towards (and in some cases, above) the head, and the spine bending so that the angle of the shoulder and hip girdles exceeded 60° on average. The shoulders typically led the hips throughout the turn. Animals re-straightened their spine and tail as they transitioned to steady running, with minimum MOI achieved around 170 *ms* on average (Fig. 2.6). The average shoulder, hip, and average heading angle were not significantly different after 250 *ms* into the maneuver, and agamas typically recovered 80% of their maximum inertia by 300 *ms*. We used the 6-link chain model to estimate angular momentum about the COM (Fig. 2.4) and found that on average, animals maintained positive angular momentum throughout the duration of the turn, despite taking several full strides.

2.4.1 Effect of changing inertia on turning rate

To gauge the effect of inertia and shape change on performance, we compared the angles of the shoulder and hip girdles, along with the average body orientation, to predictions from the rigid-body models of Section 2.2.1. As predicted, actual rotation was much larger than that predicted by the fixed-inertia model. The fixed-inertia model, (2.2), lagged behind the average orientation by up to 60°. The variable-inertia model, (2.4), also lagged behind actual rotation, by a smaller margin. Calculating an effective rigid inertia from Sec. 2.2.3 predicts that agama's moment of inertia would have to be almost three-fold smaller to achieve their early turning performance (to reach 90° as quickly as the shoulder girdle) and 1.5 times smaller to achieve the total turning performance (to reach 150° as quickly as all body segments). We therefore reject the hypothesis that rigid body models suffice to predict turning performance in agamas.

Since the time-derivative of angular momentum about the COM is the sum of external torques about the COM (by Euler's laws; see Chapter 3 for a more thorough treatment), the slope of the

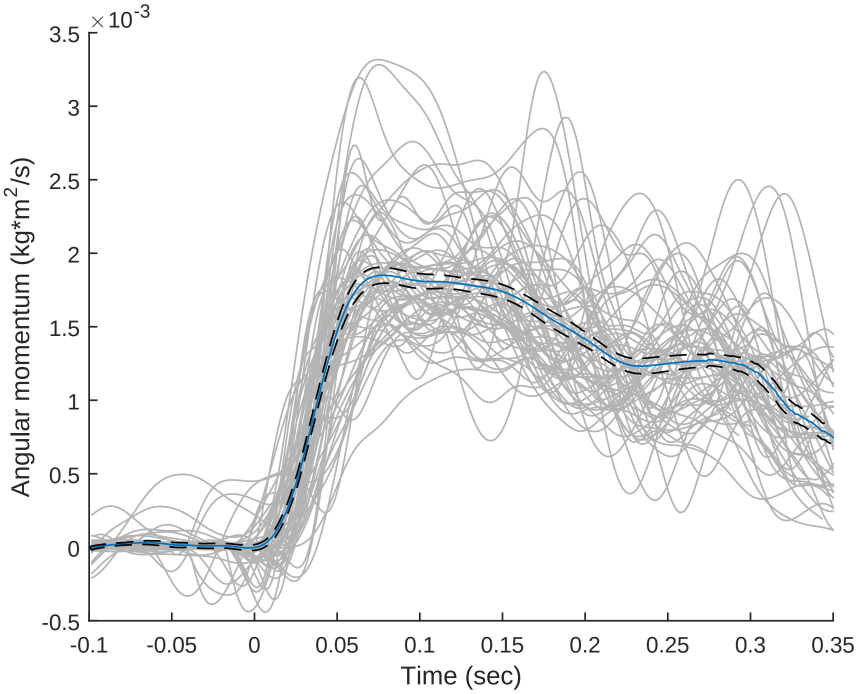

Figure 2.4: Angular momentum about the center of mass plotted against time. Individual trials (light grey) were aligned and averaged to produce a mean trajectory in blue (± SE in dashed).

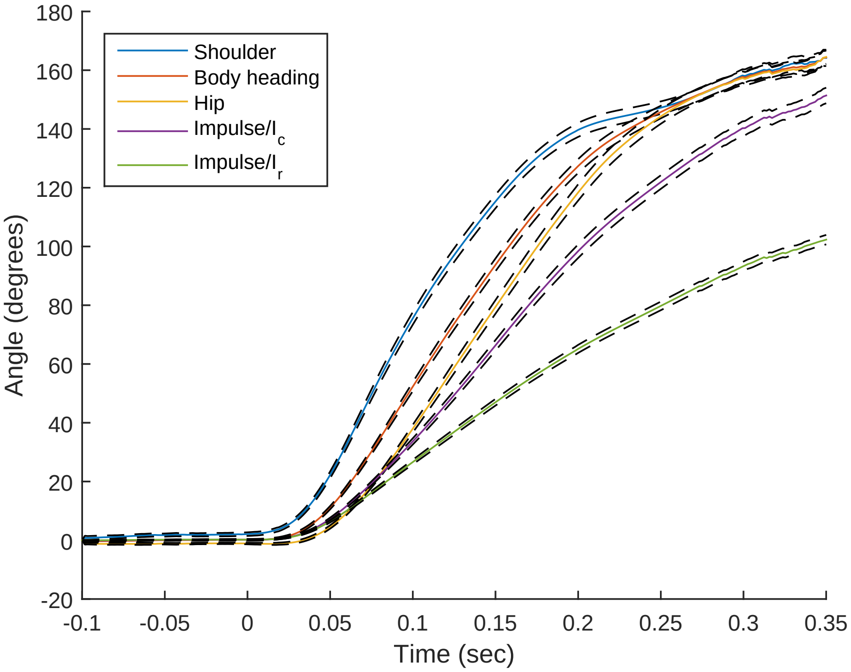

Figure 2.5: Average kinematics for turning agamas compared to average estimates for rigid-body models (mean ± SE for aligned trials). Real turns always led rigid-body estimates. Shoulder girdle, hip girdle, and average body heading as defined in Fig. 2.2. The two models correspond to the integral of impulse divided by the (variable) estimated moment of inertia, I_c, as in (2.4), and the impulse divided by the fixed maximum (rigid) body inertia, I_r, as in (2.2).

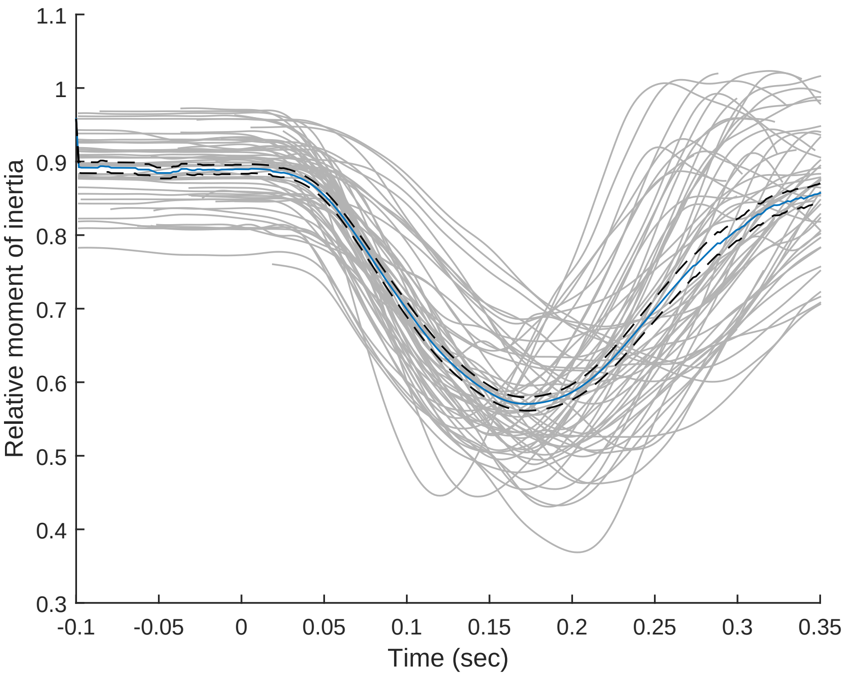

Figure 2.6: Moment of inertia relative to (maximal) straight configuration plotted against aligned time. Animals rarely achieved maximum inertia, and body bending reduced MOI to as little as 37% (57% on average) of maximum.

curves in Fig. 2.4 correspond to the action of the limbs pushing to turn the body. The largest push (biggest impulse) occurs over the first 77 *ms* on average (peak of the average angular momentum). During that time, the MOI falls from 86% of maximum to 77% of maximum (on average, Fig. 2.6); therefore during the highest external torques, MOI was relatively high, and far from the minimum value of approximately 37%. On average, over 63% of the observed the inertia reduction occurs after peak angular momentum. Agamas do not appear to preemptively reduce their inertia to lower turning resistance (e.g. as posited for theropods [67]).

While agamas did not receive the benefit of inertia reduction during the period of angular impulse, later reduction still accelerated the animal. Reduction of moment of inertia increased performance in two ways, as illustrated in the roughly 50% difference between the variable and fixed inertia predictions in Fig. 2.5. First, the MOI was smaller than it would have been in a rigid (maximal) posture, as reported above. Second, and more importantly, further decreases in MOI when the angular momentum was near its peak accelerated the animal further. Overall, changes in MOI accounted for the majority of difference between actual rotation and that predicted by a rigid agama.

2.4.2 Inertial reorientation behavior

While changes in the agama's moment of inertia accounted for much of performance gap between the rigid-body prediction and the actual turns, the variable-inertia model still lagged behind actual rotation by a large margin, particularly midway through the turn (Fig. 2.7). We hypothesized that the remainder of the difference arose from inertial forces from the spine and tail accelerating the trunk. We evaluated inertial reorientation in two ways. First, by anchoring to the IR template and predicting rotation based on observed tail range of motion; second, by using the six-link anchor to directly predict reorientation during individual trials. In both cases, we found evidence to support the hypothesis that inertial reorientation enhances maneuverability during horizontal plane maneuvering.

Predictions from first-order models

We used the six-link anchor model to make predictions of the inertial reorientation of the shoulder, hip, and average body frames based on actual shape trajectories observed during turns. From (2.2.5), we note that this model prediction is the same as the difference between the actual observed rotations and the prediction of the variable inertia model (i.e. the difference between the corresponding curves in Fig. 2.5). The average predictions are plotted in Fig. 2.7. Inertial reorientation predicted turns that were always in the direction of the turn (except for small counter-rotations of the hip during the first step). The shoulders moved the furthest, reaching approximately 50° on average, and over 80° in the most extreme case observed.

As predicted by the template, the reversed body shape change in the second half of the turn produced a negative body rotation in all trials. The final orientation did not return completely to zero. In contrast to the IR template, the six-link chain (and the real morphology of the animal) need not lose all IR upon fully reversing shape change. As discussed in Sec. 2.2.1, the six link chain can undergo cyclic deformations that produce net body rotation with net-zero shape change. If the path taken through shape space on the extension "stroke" produced less negative rotation than on the flexion "stroke," the body would retain net rotation even in the absence of external impulse. This is challenging to evaluate empirically, since animals never returned exactly to the same point in the five-dimensional shape space. Anecdotally, we found some trials in which animals returned to a straight posture with small net gains in rotation ($5^\circ - 10^\circ$); we tentatively conclude that lizards do not benefit greatly from cyclic "wiggling" to generate rotation during planar turns as explored in e.g. [42]. While IR appeared to generate little net rotation, our models predict that body shape change greatly enhanced reorientation midway through the maneuver. Near mid turn, rotation due to shape change accounts for nearly half of shoulder girdle angle.

Stabilizing final heading

The backwards rotation prediction of the IR models may have a stabilizing function. For a rigid body to stabilize its final heading in the same direction as its COM movement direction, braking forces must be applied to slow angular velocity. Specifically, its angular momentum must go to zero

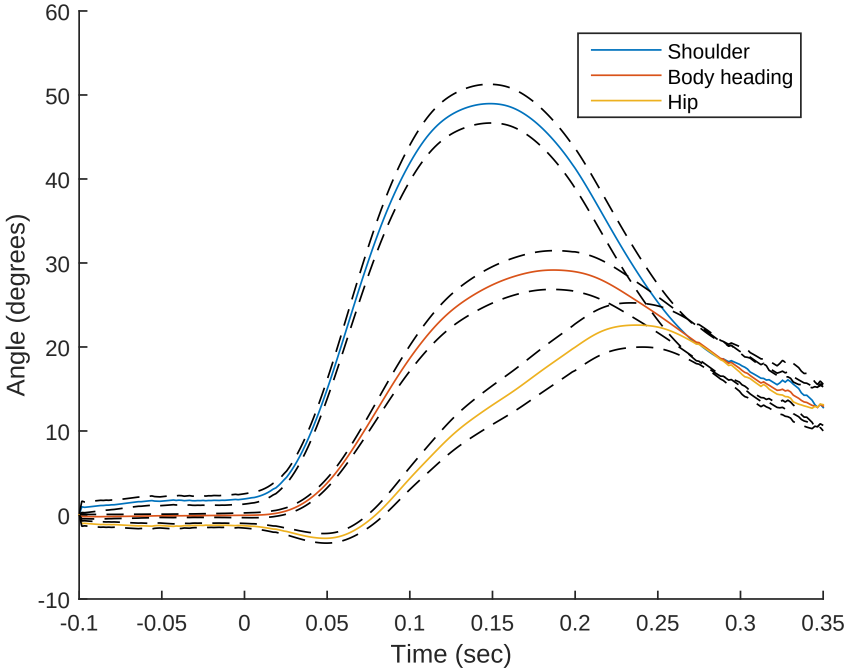

Figure 2.7: Rotation predicted by body shape change models for shoulder girdle, average heading, and hip girdle (difference between measured kinematics and Impulse/I_c model in Fig. 2.5; mean ± SE for aligned trials).

as it approaches steady running. In the turning agamas, angular momentum decreased as the animal completed the turn, but not as quickly as required to stabilize final orientation. Observed angular velocity of the torso (slope of the body heading in Fig. 2.5) fell quickly to under 10% of its peak value by the end of our observation window of 350 *ms*, whereas over 40% of angular momentum remained at the end of the trial. The angular velocity predicted by the rigid (variable inertia) model (i.e. slope of the $Impulse/I_c$ curve in Fig. 2.5) is more than double the actual observed velocity. As the agamas returned shape to the steady-running posture (i.e. uncurl their spine/tail so that shape angles near zero), the IR model predicts counter-rotation; that is, they swing their tails in the direction of angular momentum, reducing body rotation in the manner of [1]. Compared to a rigid-bodied animal, the agamas therefore appear less reliant on braking forces to stop the turn and prevent over-rotation.

Modulating leg speed

At any point in time, the velocity of a physical location on the chain can be modulated by shape change without changing the total linear and angular momentum about the COM. Since muscle forces are strongly velocity-dependent, this modulation could exert considerable influence over the limb forces. To test the extent to which this affected leg velocity during observed steps, we compared observed leg velocity to a prediction based on rigid-body motion. We defined a virtual leg, $\mathbf{r}_\ell$, as the vector to the foot from the shoulder or hip (depending on the limb). If body shape velocity were zero, the leg velocity could be found from the center of mass velocity, $\mathbf{v}_{com}$, angular momentum $\mathbf{H}$, and instantaneous MOI, I_c as

$$\dot{\mathbf{r}}_{\ell,rigid} = -\mathbf{v}_{com} - \mathbf{r}_j \times \frac{H}{I_c}\mathbf{E}_3,$$

where $\mathbf{r}_j$ is the vector from body center of mass to the hip/shoulder joint. To see how body shape change affected limb velocity, we regressed the components of $\dot{\mathbf{r}}_{\ell,rigid}$ against the actual limb velocity, $\dot{\mathbf{r}}_\ell$. If shape change had a negligible effect on limb speed, the trajectories would fall on the line of unity slope. If shape change decreased leg speed, the rigid-body prediction would fall above the line of unity.

We found that body shape change increased limb velocities for all limbs during the first step of almost all trials (Fig. 2.8); this is unsurprising given the conclusion of Sec. 2.4.2 that shape change greatly increases body angular velocity during the first step. Changes in the second and third step were more mixed and did not show a linear relationship, with some steps showing increased or decreased velocity due to shape change. Third step differences were small as limb velocity is dominated by forward running speed rather than turning during the latter phase of the maneuver. While first step limb velocities were nearly doubled on average by shape change, they also were slow relative to limb velocities observed in later steps (typically $1/4$ to $1/2$ maximum observed speeds). We conclude that increased body rotation due to shape change typically comes with a cost of increased leg speed (and therefore likely decreased ground reaction force).

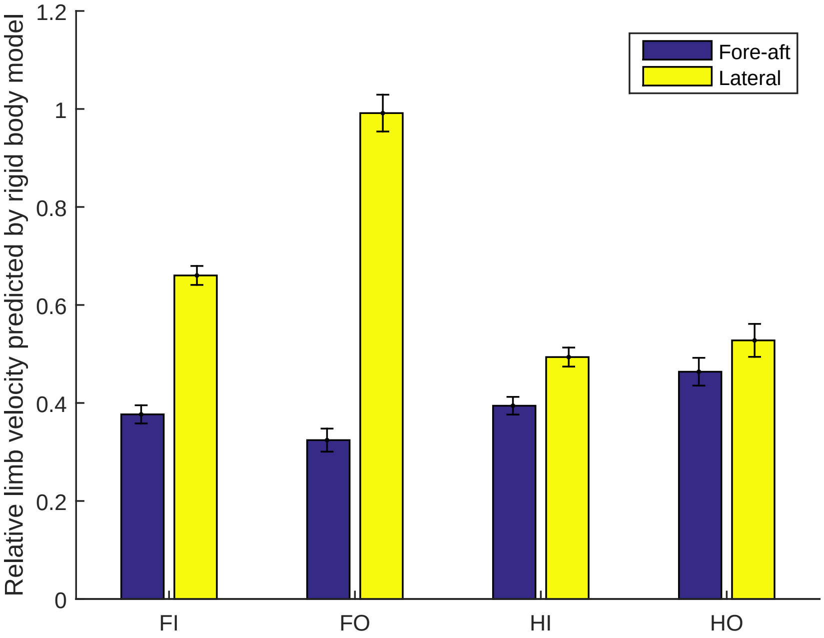

Figure 2.8: Limb speed predicted by a fixed-shape model relative to actual observed speed (see text for definition of limb speed). Values of less than unity mean the animal would experience lower limb speeds if it had not changed body shape during the step.

Is rotation by shape change active?

Body shape change greatly increases body rotation in the first half of the turn, but as noted in Sec. 2.2.1, our first order models could not discern between active (spine-driven) inertial reorientation and passive shape change under the influence of external forces. To test the hypothesis of an active spine capable of generating inertial forces, we compared work done by the legs to total changes in kinetic energy of the body. If the spine were passive, limb work would be equal to or greater than total energy change, as the spine would absorb or passively transmit energy to distal segments (as in a whip). Kinetic energy greater than leg work would indicate a propulsive role of axial musculature during turns, supporting the IR hypothesis.

We calculated work done by the limbs for the steps that fell on the force platform (see Section 2.3 for details) by assuming that legs were of negligible mass. We calculated the resultant force and torque about the center of mass of the segment the leg was attached to (shoulders or hips) and used kinematics to calculate the instantaneous power of these forces,

$$P = \mathbf{F} \cdot \mathbf{v}_{seg} + (\mathbf{r}_{foot} \times \mathbf{F}) \cdot \dot{\theta}_{seg} \mathbf{E}_3, \tag{2.7}$$

where $\mathbf{r}_{foot}$ is the vector from the segment COM to the foot, and $\dot{\theta}_{seg}$ is the angular velocity of the segment.

We integrated power over the step to calculate work by the limb. Since we only had force data from one leg at a time, we compared limb work to kinetic energy for each limb separately over the same time interval from the onset of motion to the time when any foot touched down for the beginning of its second step. Since limb work correlates with total work (due to trial-to-trial variations in effort), we fit linear models of limb work against kinetic energy change; the slope of the fit line corresponds to the average fraction of total work done by that limb (plotted as slope ± one standard error of slope in Fig. 2.9). We used the sum of the average work fractions as an estimate for the total limb work relative to kinetic energy. The limb work accounted for just over half of the total change in body kinetic energy during the first step, indicating a large role for the axial musculature and supporting the hypothesis of an active spine.

2.5 Discussion

The fixed inertia model used in previous literature was a poor predictor of turning performance for *A. agama*. The torsos of agamas turned more than twice as far as predicted by the fixed inertia model, and the shoulder girdle rotated up to four times faster midway through the turn. We conclude that variable body inertia and body shape change considerably increased the turning performance of agamas relative to a stiff-bodied equivalent. Estimates of limb and whole-body energetics strongly support the hypothesis that body shape change is actively generated by axial musculature. Unlike previous robots that used IR to turn against the action of leg forces (generating drag impulse in the opposite direction of the turn), agamas appear to use inertial forces from spine and tail in concert with external (limb) forces to generate their turning. Our six-link anchor model

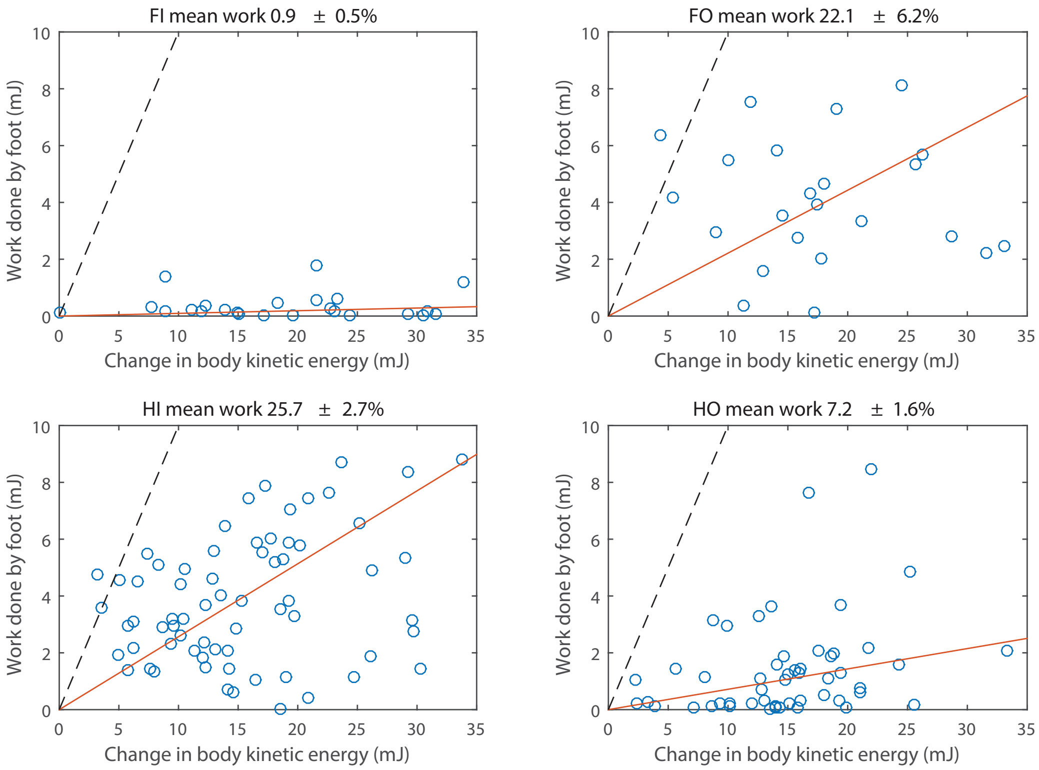

Figure 2.9: Work done by feet during the first step vs. change in total kinetic energy. Work done by all feet only accounts for about 50% of total work done during the first stride.

predicted high inertial effectiveness at rotating the hip and shoulder girdles, potentially enabling animals to modulate body posture and limb speeds rapidly and without external forces.

In contrast to the net reorientation of Chapter 1 and the single-direction impulse stabilization of [1], the IR behavior predicted during turning was bi-directional and low net reorientation. If range of motion is fixed and confined to a plane, IR is limited by the inertial effectiveness and range of motion (see (1.11) in Chapter 1); therefore it is not surprising that agamas could not use IR to produce the very large reorientations demanded by the prey capture task (our six-link anchor predicted at most 80° of maximum rotation using the observed range of motion of the spine). However, the agamas are not confined to planar motions like those of our models – the tail can be swung overhead as easily as to the side [1] – so it is surprising that they return their shape change along roughly the same path, thereby eliminating any IR gains in rotation from the early part of the turn. Hypothetically, agamas could "helicopter" the tail overhead upon reaching their planar range of motion limits (so that the planar projection of motion continues in the direction opposite the turn, maintaining IR in the direction of the turn). This overhead motion could produce some roll [20], which might be disadvantageous enough to counter any yaw advantage.

Alternatively, there may be some advantage to straightening the body (and therefore generating inertial forces that counter-rotate the torso). The hips or shoulders could be moved into a posture more advantageous for generating limb forces, or inertial reorientation of body segments might reduce joint (and therefore muscle) velocities. In this particular maneuver, the lizards are transitioning to straight running, and therefore the uncurling motion may aid linear acceleration. In particular, counter-rotation of the tail stabilizes body orientation in the direction of final COM velocity without the need for braking forces. Transferring angular momentum to tail rotation could allow lizards to escape the constraints of "leg effectiveness" [64] – that is, limb forces are free to produce deflection (forces that change COM velocity direction) without concern for their rotational impulse. A rigid-bodied animal (e.g. a cockroach) would need to choose limb forces such that the resulting angular impulse stopped the turn, limiting some legs from producing linear impulse in the direction of final running; for example, legs on the outside of the turn could not generate large linear forces without over-rotating the animal. In the next chapter, we will examine limb contacts and forces in more detail and attempt to address this hypothesis directly.

Our rigid-body model predicted that body shape change does have a substantial impact on limb speeds, and given that muscles are highly speed-dependent, we hypothesize interaction between shape change and external forces could be significant. While we did not find evidence of jamming as experienced by robots turning with IR, we predict that external forces would be lowered during the periods when limb speed was increased under the influence of body shape change. During the first step, where body shape change greatly increases torso speed, we find limb speeds increased by a factor of roughly two. Further, limb contact time is greatly reduced, as limbs extend more quickly. In vertical jumping, animals including humans [76] and other primates swing their appendages upward during takeoff, thereby producing inertial forces that reduce limb speed and extend stance time (e.g. the opposite of the agama's turning strategy). If agamas swung their tail in the opposite direction during the first step, they could generate more angular impulse and turn much more quickly on the second stride. Again, this hypothetical alternative may have interesting disadvantages. Body rotation would lag significantly in the first step of the hypothetical strategy. Agamas are visual predators, and early rotation may be crucial for maintaining sensory contact with their prey. Evolutionary history may also influence maneuvering strategy; the lateral bending and tail swing bears striking similarity to the C-start escape maneuver of fish. The major hindlimb retractor muscle in lizards is located in the tail, so tail motions may be linked to limb force production. There may be dynamic advantages to the lizards' strategy as well. Shape change in the direction of the turn results in large rotation of the shoulder girdle, potentially pointing legs into the turn so that limb forces can be more effective; limbs may be able to generate their largest forces in the anterior direction. Perhaps most intriguingly, synergy between inertial reorientation and impulsive motion could greatly increase robustness. If limbs transiently lost traction, early body rotation in the direction of turn could be maintained. Likewise, body orientation can be stabilized at the end of the turn regardless of the ability to produce braking forces. Body flexibility may enable much greater control of orientation in the face of unreliable ground contacts.

The results of this chapter challenge the earlier hypotheses by Carrier and others that elongate body plans are necessarily detrimental to maneuverability. Even leaving aside the potential advantages to robustness and the turn-run transition hypothesized above, body flexibility enables agamas to turn at rates equivalent to an animal with roughly $1/3$ to $1/2$ of their body inertia – largely eliminating the deficits predicted by Walter and Carrier [61]. The effects of IR and shape change could be even more dramatic in theropod dinosaurs, whose tail effectiveness could be even higher [1] than found in lizards, and whose bipedal form is more sensitive to the force tradeoffs expressed by Jindrich's Leg Effectiveness Number. We hypothesize that long tails in these animals actually increase agility, rather than decrease it. Intriguingly, some agile ground birds (particularly roadrunners) have long, stiff tails (albeit made of feathers and therefore likely not as massive as those found in non-avian theropods) – it would be fascinating to see if tail function in these animals is similar to that found in lizards. Finally, we hypothesize that tails could further enhance turning in robots if inertial forces could be coordinated with limb forces (or if limb mechanics were tuned to eliminate the negative effects experienced by TaYLRoaCH). Most extant robots have very limited capability to control forces in the horizontal plane (particularly lateral forces), and this may be primary obstacle to achieving the performance exhibited by the agamas. Such a machine would also be a powerful physical model for exploring the strategic tradeoffs hypothesized earlier.

Chapter 3

Control of Planar Maneuverability in a Lizard

3.1 Introduction

A defining feature of animal locomotion is rhythmicity. Proximately speaking, rhythmic motion of appendages is necessary, since truly continuous rotation (e.g. wheels, axles) is vanishingly rare in animals. However, many observed behaviors are not only rhythmic but periodic in body shape space (e.g. the relative positions of appendages) and induced external forces. There is strong and growing evidence that the prevalence of locomotor periodicity may be the signature of self-stable neuromechanical oscillators [77, 78] that simplify the control of animals' notoriously complex, nonlinear, high-dimensional bodies through an equally-complex world [79]. This periodicity also aids the study of locomotor behavior, enabling the easy collection of multiple replicates (e.g. strides) per trial, and affording the application of a host of theory devised for periodic systems [77]. Steady locomotion typically features remarkably low variance in observed kinematics and forces between instances of movement across strides, trials, days, and even individuals [80–82].

On the other hand, locomotor behaviors are not typically steady and periodic for long. Critical behavioral tasks (e.g. prey capture, escape from predation) and real-world topological structure (e.g. surface roughness at scales below and above the size of the agent) preclude the sort of flat-ground, straight-line locomotion prevalent in lab studies; unsteady, non-periodic "maneuvers" are arguably the norm. Here we define maneuvers more specifically as "locomotor transitions," the interstitial behaviors between bouts of steady locomotion. For example, turning could be steady (i.e. running in a circle), but a "turn" (a redirection of straight-running velocity) is by definition unsteady – something about the animal's shape kinematics and/or external forces must change to perturb the body away from straight running. How drastic this change must be depends on the properties of the periodic behavior and the desired change. Reduced-order horizontal-plane mechanical models of locomotion predict that running direction is only neutrally stable (though angular velocity is asymptotically stable) [83], so small perturbations could induce a turn [84].

Effecting a change in a locomotor behavior with a stronger stability basin (e.g. speed) requires larger changes. How these behaviors are generated and stabilized remains an open question in both locomotor neuromechanics and robotics.

In this chapter, we will return to the planar maneuverability task of the previous chapter (a transition from standing, to turning, to straight running) with a new focus on how the lizards accomplish this dramatic, unsteady locomotor behavior (see Fig. 2.3 for illustration). Legged turning has been studied in biped, quadruped, and hexapod animals, as well as robots with as few as one [85] and as many as sixteen [86] legs. In almost all of these studies, animals and robots turned relatively slowly, rotating 10-30 degrees per step. In animals as diverse as cockroaches and ostriches, turning is accomplished by small variations in kinematics and forces from the steady running pattern [62]. Likewise, robots over a wide range of body mass, from under 100 *g* [70] to over 10 *kg* [87] accomplish turns through small, differential changes to steady running gaits. These observations are consistent with the predictions from LLS and other reduced-order models that transitions could be induced by small parametric changes. Larger turns of 60° [88] and 180° [89] have been studied in human running and walking, respectively. Even in the largest turns, humans retained some flexibility in locomotor behavior, with two distinct strategies identified in [89]. In all sizes of turns by bipeds, rotation appeared to be controlled by the braking forces that helped redirect COM motion [88]. The prey capture task studied here increases the difficulty of the maneuver because animals begin at rest, so that no braking forces are available. In addition to generating and completing a large turn, agamas must accelerate quickly to reach prey before it escapes. Here, the time pressure of the prey capture task and large (180°) rotation required should challenge the locomotor capabilities of lizards to their limit.

Success during the prey capture behavior is determined (at minimum) by the lizard's ability to get its head to the location of the prey as quickly as possible. Success of the capture itself depends on subtleties not related to the overall locomotor behavior (e.g. jaw and tongue mechanics, small movements of the head relative to the body). We therefore chose to represent the maneuvering task of interest as (1) rotation of the body to align with the prey target vector, and (2) acceleration of the COM along that vector. The resulting *task space* (the low-dimensional subspace of body movement relevant to task performance, [90]) is three-dimensional, defined by body heading, θ_b, and body position in the plane relative to the target, $(x_t,\ y_t)$. Since we could not always observe the prey capture event (see Sec. 2.3 for details), we considered instead the subtask of reorienting the body and accelerating towards the prey; the resulting task space being θ_b, body speed in the target direction, v_t, and body speed orthogonal to the target direction, v_o. If the target is relatively far away, and body speed is subject to some saturation $v_{t,\ max}$, this subtask will be completed on route to completing the overall prey capture.

Previous observations in animals and robots suggest many solutions to this task. One simple strategy would be to rotate in place until $\theta_b = 180°$, then accelerate in the target direction to maximize v_t. Alternatively, the agamas could accelerate anteriorly (away from the target) and then turn gradually as observed in running cockroaches. Both of these strategies intuitively seem likely to be slow. As extensively examined in Chapter 1, the time-optimal solution to a net reorientation with bounded actuator input is bang-bang. If turning and linear motion were completely decoupled, the time optimal solution would be to apply maximum turning torque and maximum force in the target direction simultaneously, and then switch to maximum braking torque while maintaining maximal linear acceleration. Since in real animals, some coupling is almost certain to apply to rotational and linear forces, this strategy may need to be modified to satisfy constraints on geometry and muscle function. However, we hypothesize that tasks with strong time pressure (e.g. prey capture) will push animals as close to the optimal solution as these constraints will allow. We therefore expect rhythmic motion, but not periodic forces, as agamas negotiate the changing constraints of applying task forces. We also expect low variability of gait and forces, not because of strong periodicity, but due to the demands of constrained time-optimality.

The multi-axial nature of the planar maneuver task requires the animals to generate turning torques and linear (accelerative) forces, generating further control challenges. Setting aside internal geometric constraints (limb geometry, muscle moment arms, etc.), a foot placed at any point around the center of mass can generate force to accelerate the body towards the objective and torque to turn the body towards the objective, but not necessarily both [62]. Since our experimental task places larger demands on rotational and linear impulse than those previously explored, we hypothesize a greater signature of the role of tradeoffs in limb function. To identify these tradeoffs and quantify their effect on leg function, we seek a generalization of Jindrich and Full's "Leg Effectiveness Number" (LEN) [64], which expressed limb tradeoffs as the ratio of body rotation to COM course correction induced by a ground reaction force. Since COM velocity in the prey capture task here starts at zero, LEN is undefined. Instead, we will look (in the same spirit of [64]) directly at the geometry that facilitates or precludes synergy in turning and deflection. The cross product of a unit vector $\mathbf{e}_t$ towards the target, and a unit vector $\mathbf{e}_\ell$ pointing from COM to foot, determines the extent of possible synergy between target-oriented acceleration (positive force along $\mathbf{e}_t$) and rotation (positive moment; i.e. positive planar cross products). We will call this product the "Task Moment Arm", $\Gamma := \mathbf{e}_\ell \times \mathbf{e}_t$. When $\Gamma = 1$, maximum task acceleration and rotation are perfectly synergistic (i.e. the same force accomplishes both). When $\Gamma = -1$, acceleration and rotation are mutually exclusive. When $\Gamma > 0$, task acceleration and rotation are synergistic in the sense that a bounded force producing maximum task acceleration exerts a positive moment and vice-versa. Negative gamma means the controller must choose between acceleration and torque, or that large forces perpendicular to the task direction must be exerted to cancel the negative moment exerted by positive task forces (see Fig. 8 in [64] for a graphical example of this case). In the case of the prey capture task described here, task-orthogonal impulses would take the animal off course and therefore must be avoided or compensated by other limbs. We will use Γ to predict limb function across two steps in Sec. 3.3.5.

Both roboticists and biologists are keenly interested in the interaction of body design and performance; in this work we will begin to test hypotheses of the functional morphology of planar maneuverability. Task performance depends (in a complex and dynamic way) on body mass, inertia, and the ability of limbs to exert forces in the horizontal plane. In Chapter 2, we found that lizards can largely escape the consequences of their relatively high body inertia by changing body shape while turning. Here we will examine whether lizards have other adaptations that enhance planar maneuverability. Internal constraints on limb forces due to posture (e.g. changing mechanical advantage of muscles with respect to joint motion) could exacerbate the tradeoffs enforced by external geometry. Legs with the capacity to exert maximum forces in any direction would enable the most flexibility in maximizing maneuvering performance. Since animals typically generate their largest forces along their limbs (thereby minimizing the internal moments about joints [91]), upright postures are disadvantageous with respect to horizontal plane force generation. The sprawled posture of lizards has been hypothesized to confer additional maneuverability in the plane [92]. By contrast, mammals all share a largely parasagittal posture; larger species are more upright, and smaller mammals more crouched [91]. These animals must step laterally to generate large lateral forces [88] or roll the body to one side [59]. Despite many robots described as sprawled-posture, few legged machines are capable of generating large lateral forces; most rely on differential left/right distribution of fore-aft forces to generate reorientation. Linear acceleration performance also places demands on morphology – generating large fore-aft forces without large pitching moments requires a low center of mass [93]. Hind limbs typically generate the most acceleration force [94]. Body design to enhance acceleration performance (long, strong hindlimbs) may reduce turning performance if functionally-reduced forelimbs lose the ability to generate large lateral forces. A better understanding of how limb morphology affects maneuverability would benefit both comparative biomechanics and robotic design. We hypothesize that sprawled, multi-legged body plans (as in *Agama*) should be least constrained in generating force/torque to accomplish planar maneuverability tasks, and thus may approach the predictions of the time-optimal control models discussed above.

3.2 Methods

Experimental animals, training, protocol, and models followed the approach of the previous chapter, Sec 2.3. We calculated kinematics and momenta using the rigid-body models and aligned trials temporally before resampling and averaging as in Sec 2.3.7. We calculated force and torque about the center of mass by numerically differentiating linear and angular momentum about the COM (these momenta were themselves calculated from differentiated kinematic measurements). We filtered forces estimated from kinematics with a lower cutoff frequency (20 Hz) than used to calculate velocities and filter signals from the forceplate (40 Hz).

3.2.1 Single-leg perturbations

In a subset of trials, we introduced a low-traction substrate to probe the functional role of individual limbs by removing their contribution to the maneuver. The low-traction substrate (slip plate) consisted of a 6.5 cm by 12 cm rectangle of sheet steel lubricated with vegetable oil. The plate was fixed to the acrylic platform near the force platform. The experimenter manipulated the agamas initial position so that one (and only one) of the agamas feet began the trial on the slip plate (and on the force platform as well, if possible). We validated the traction-reducing approach by placing animals on a larger plate of the same design (25 cm by 40 cm, so all limbs rested on the low-traction surface). Agamas on the large plate slipped with each step, and both turning and linear acceleration were greatly attenuated.

3.2.2 Measurements of variability

After temporal alignment, we resampled the trajectories (by linear interpolation at the same sample rate) and found the mean signal at each new time sample across all trials, along with a 95% confidence interval for the mean (± one standard error (SE), calculated at each sample). To evaluate the predictive power of the mean signal (and therefore the uniformity of performance across trials), we calculated the amount of variance remaining among all trials after subtracting the mean, relative to the variance in the original (aligned) data set, known as the Relative Remaining Variance, or RRV [95]. We also calculated Coefficients of Variation by normalizing standard deviation to an appropriate mean (e.g. see Sec 3.3.2).

3.3 Results

We observed 83 turns from three individuals. We used the same trial inclusion criteria described in Chapter 2, Sec. 2.3.6. We did not find significant differences in task performance across individual, so we lumped data from all trials together in the following. Agamas began at rest, with all limbs contacting the substrate. Shortly after prey stimulus presentation, they initiated turning by pushing laterally with the forelimbs and applying twisting forces with the hindlimbs. Agamas took 2-3 strides to complete the turn and transition to straight running. Animals typically took about 250 ms to complete the maneuver inclusion criterion (150° rotation and 70 cm/s) and 380 ms to complete the maneuver (i.e. to reach peak velocity). Body shape change played a large role in increasing task space reorientation (See Chapter 2 for a thorough treatment of the role of shape change).

3.3.1 Task space behavior

We estimated prey direction by calculating the direction of the COM at peak velocity before the end of each trial. The vector in this direction established the local task reference frame for that trial. The average angle between this vector and the initial orientation of the animal's body axis was $159 \pm 2.1°$, and was set by the accuracy of the experimenter's throw (since we lumped left and right turns, this number could never exceed 180°). Agamas reached an average angle of $167 \pm 2.1°$ on average (Fig. 3.1) maximum rotation, and 1.07 ± 0.1 m/s maximum speed as they maneuvered through task space.

The average task trajectory sharply accelerated to a maximum angular velocity of over $800°/s$ in the first 100 ms and rotated at a nearly constant rate until about 120°, where angular speed tapered off towards the end of the trial (Fig. 3.1). By contrast, linear velocity of the COM towards the target increased more slowly, with steady average acceleration throughout the task (Fig. 3.2). Agamas gave consistent performances – the average task trajectory explained 98% of variation in the angular and 85% of variation in the linear components of the task, respectively (e.g. $1-RRV$ after subtracting average).

Agamas did not separate reorientation and Cartesian motion. COM velocity was initially backwards on average (i.e. towards the prey), and then increased primarily in the lateral axis for the first half of the maneuver. Agamas experienced high lateral COM velocities – almost 40 cm/s on average and frequently over 70 cm/s (Fig. 3.3). Midway through the turn, this lateral velocity accounted for all the task-direction velocity (as the body axis was exactly perpendicular to the task direction); this point typically coincided closely with maximum lateral COM velocity. The angle of misalignment between heading and velocity (i.e. the angle of COM velocity in the body coordinates) remained larger than $90°$ for the first 100 ms, and exceeded $45°$ for the first $167ms$ of the behavior on average; heading and course did not align until nearly the end of the maneuver (over 350 ms from onset of movement). Agamas reached more than 50 cm/s before reaching $90°$, i.e. while pointed away from the direction of final motion. Because of the large lateral velocities, agamas were able to avoid generating motion in the direction perpendicular to the task direction – on average, less than 2 cm/s maximum. Turning continued at high rates during this linear acceleration. Heading angular velocity exceeded $600°/s$ midway through the turn while the lizards simultaneously ran over 50 cm/s on average.

3.3.2 Gait pattern

Agamas generally used trot-like gaits, but patterns varied widely from trial to trial in the sequence, synchronicity and number of contact events. We labeled limb contacts as (F)ront or (H)ind, and (I)nside or (O)utside of the turn, for example the front outside limb was labeled FO. All individuals in all trials started the maneuver with all limbs in contact. Limbs lifted shortly after the onset of motion; on average at least one limb lifted in the first 50 ms (Fig. 3.4). After one transition stride (which lasted from approximately $100-300$ ms after onset of motion), agamas typically adopted their preferred steady-running gait, the trot (see exemplar trials in Figs. 3.5, 3.6). The transition stride featured high variability. The most common pattern saw the FI and HO leg pair touch down first, followed by the HI limb, which often overlapped considerably with the HO limb. The most significant variation came in the form of deletions, where steps did not appear in the transition stride (the second step instead occurring with its diagonal trot partner in the third stride), insertions, where a limb took two steps in the period its trot partner took one, or extensions, where a limb remained in contact with the ground for much longer than usual, effectively fusing its first and second steps (see Fig. 3.6 for an example). Stepping frequency (defined as the time from liftoff to liftoff on consecutive steps) was not significantly different between the second (6.78 ± 1.4 Hz) and third (6.67 ± 1.2 Hz) steps; the frequency of the first step was undefined since animals start at rest.

We averaged the contact condition of all feet across all trials after alignment and resampling (Sec. 2.3.7) to produce an average gait pattern representing the probability of limb contact (Fig. 3.7). The average pattern revealed strong retention of the trot motor pattern throughout the maneuver. Swing and stance phases of the diagonal leg pairs were aligned in time and of similar

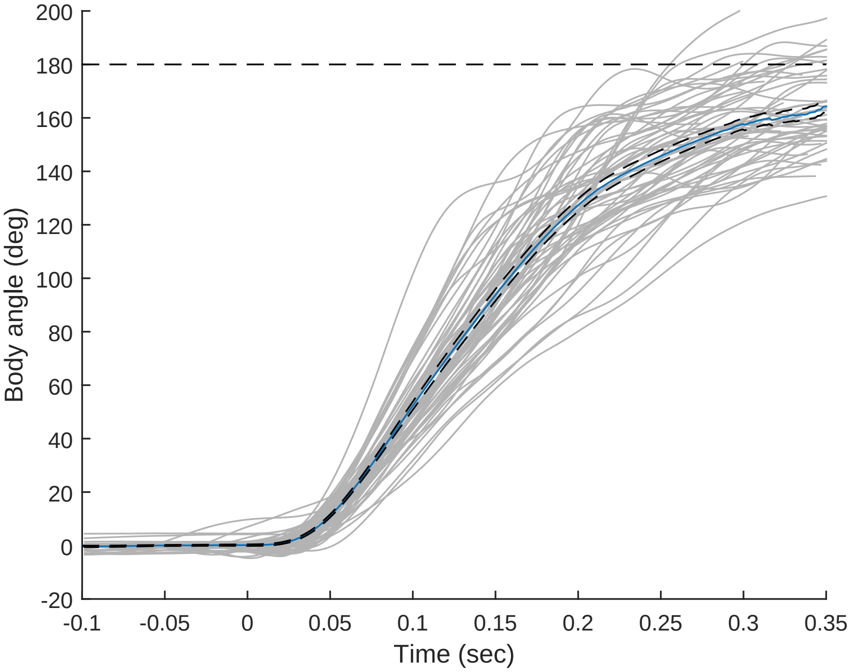

Figure 3.1: Task performance in rotation. Agamas turn almost 180° in about 400 *ms* on average. The mean turning time series (blue curve, ± one SE) accounts for about 98% of observed variance in turning kinematics.

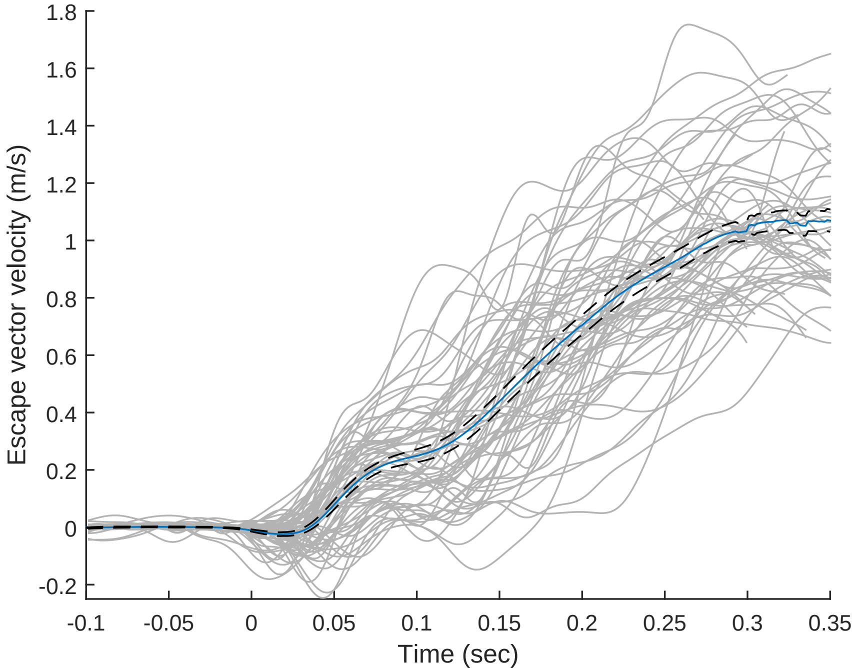

Figure 3.2: Task performance in linear progress towards target. Agamas accelerate to more than 1 m/s at an average acceleration of about 0.3 g. The mean speed time series accounts for 85% of observed variance in acceleration kinematics.

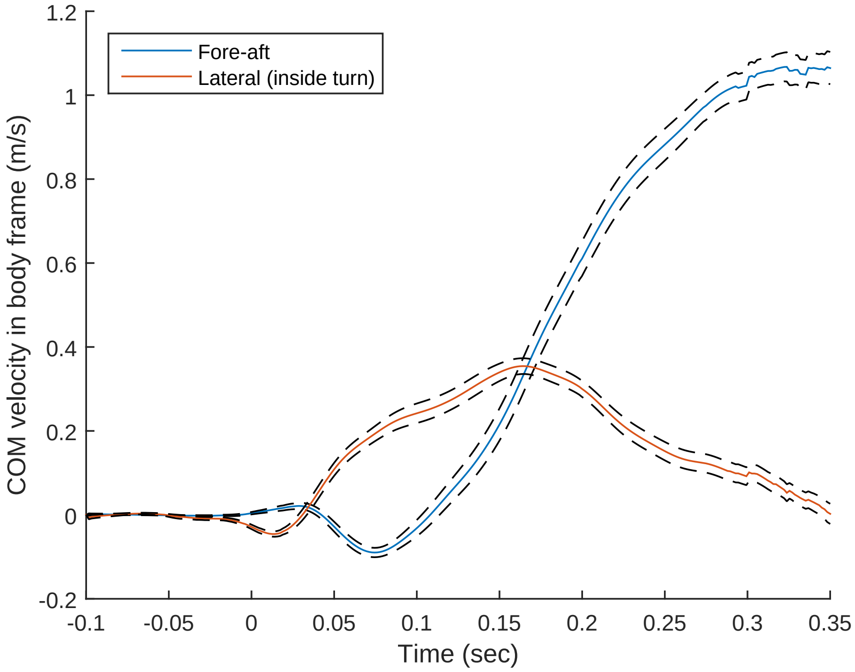

Figure 3.3: Center of mass velocity in the fore-aft and lateral body frame. Agamas ran sideways at relatively high speeds midway through the maneuver.

duration. The transition stride saw larger overlap (duty factor greater than 50%) than the third stride; aerial phases were common during the third stride. To better quantify the connection between the transition gait and the steady trot, we examined the "mutual duty factor" between limb pairs, defined as the fraction of shared contact between two legs during each step. Mutual duty factor in the third step was over 75% on average for trot limb pairs and less than 20% for the opposite pair, indicating strong synchronicity of touchdowns and liftoffs[1] and corroborating the average gait diagram's suggestion of a trot pattern in this step. The second, transition stride was more mixed. The trot partner shared the most overlap for each limb, but other limbs also had high overlap. The HI limb had the highest shared contact time with the HO limb (note the relatively lower mutual duty of the HO with respect to the HI, indicating that HI steps were often longer in duration).

Variation of limb contact timing was much higher than that of observed task performance. The average gait pattern explained only 53% of variation (e.g. 47% RRV) in the front outer limb, and 68% of variation in the hind outer limb (the most consistent of all limbs). We measured coefficients of variability (CVs) by taking the standard deviation in touchdown timing for a limb relative to its trot partner, divided by the mean step duration for that limb. CVs for the transition stride were 24% and 35% for the inner and outer front limbs, and 22% and 27% for the inner and outer hind limbs, respectively.

3.3.3 Maneuvering forces

Agamas generated planar maneuvers by exerting linear and angular impulses about the COM. In Chapter 2, we showed that turning agamas experience up to 30° inertial reorientation of body heading due to spine bending and tail swinging. However, this rotation was reversed before the end of the turn, and therefore angular impulse was necessary to produce the large rotations accomplished in this task. Based on our expectation of constrained, high-effort control inputs, and the strong stereotypy of task space kinematics, we expected that external forces and torques would be consistent and large relative to running forces. Instead, we found forces with similar overall trends (Figs. 3.9, 3.10) but large variability from trial to trial.

Averaging the force/torque patterns as with the body kinematics produced average force patterns that were capable of producing the average task; i.e. the time integral of the average force in Fig. 3.10 is the average momentum of the center of mass in the target direction, and the average torque produces the average angular impulse in Chapter 2, Fig. 2.4. However, these averaged force trajectories were not good models for what animals actually did to generate maneuvers. Relative remaining variance was high for both force (72%) and torque (60%). The peak task-direction force on average was just over 60% bodyweight, but only one trial had peak forces that low; the average peak force was 133% bodyweight, and forces above two bodyweights were common (gray curves in Fig. 3.10). Peak horizontal forces for running lizards are typically near bodyweight [92, 96]. Average turning torques were similarly low compared to peak observed values, and to peaks near

---

[1] We did not separate insertions from this set of steps, so some of these third steps actually occurred during the second (transition) stride; this figure thus represents a lower bound estimate of the synchronicity in the third stride.

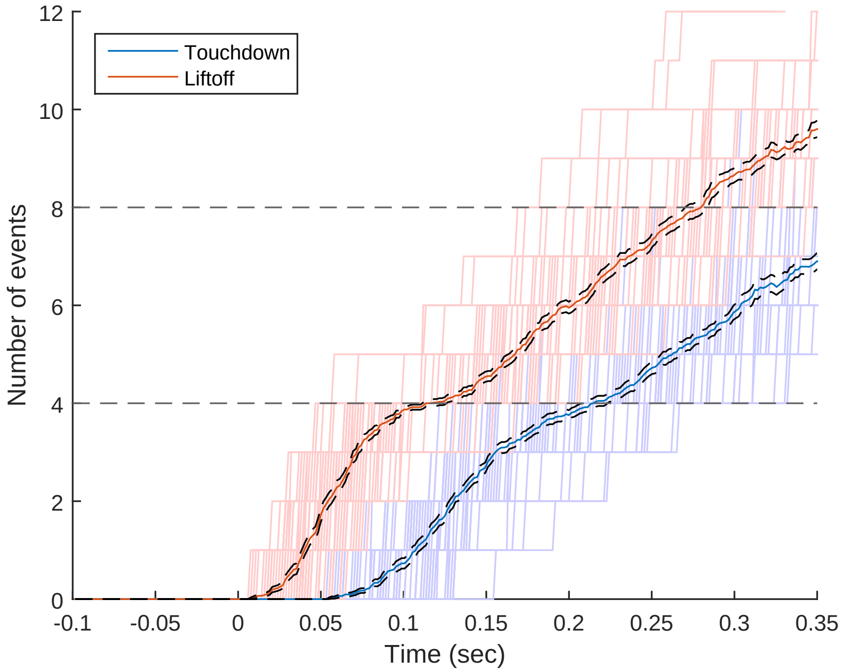

Figure 3.4: Number of touchdown (blue) and liftoff (red) events plotted across all legs against aligned time. Agamas took two full strides to complete the maneuver on average.

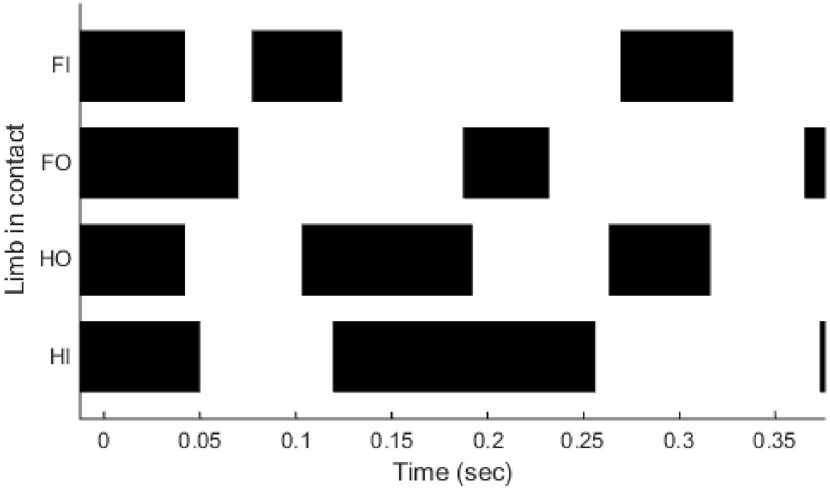

Figure 3.5: Gait diagram for a typical unperturbed maneuver. Dark bars represent limb contact for (F)ront and (H)ind limbs on the (I)nside or (O)utside of the turn. All limbs begin in stance and transition to a trot gait near the end of the trial.

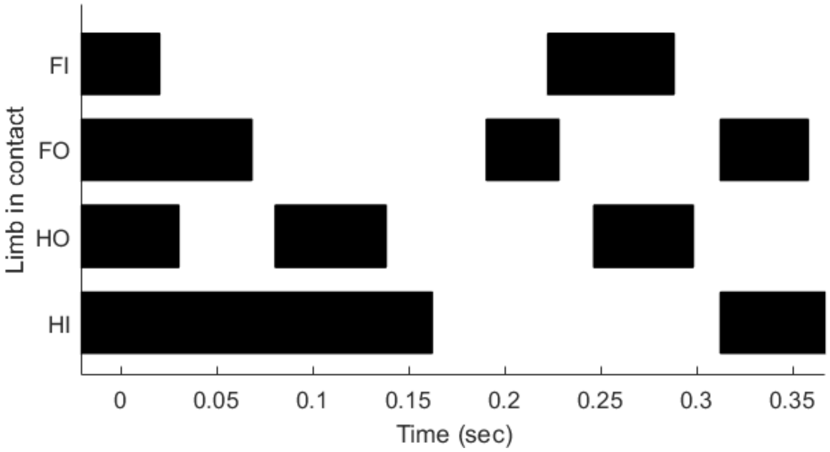

Figure 3.6: Gait diagram for a less typical unperturbed maneuver, showing extended hind inside step and delayed front steps.

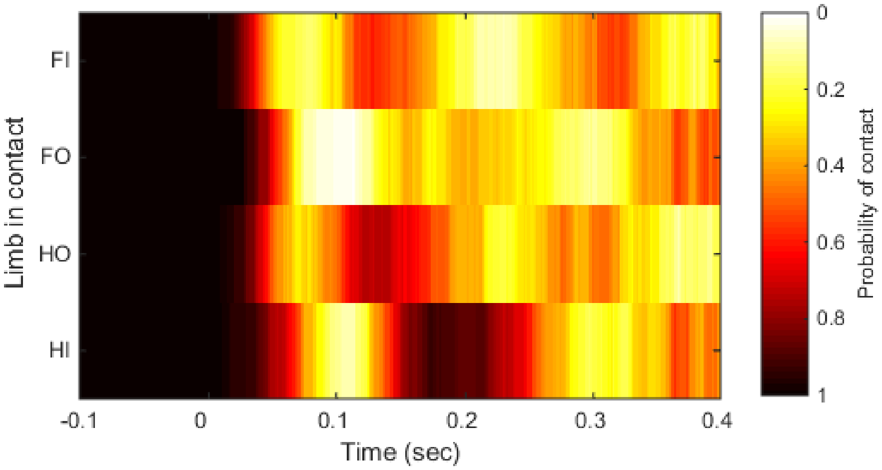

Figure 3.7: Averaged gait diagram for unperturbed maneuvers. If the limb were in contact in all trials at a particular time, the diagram would be black at that instant; this is true only for the beginning of the maneuver. Orange values show times when probability of contact is near 50-50 chance.

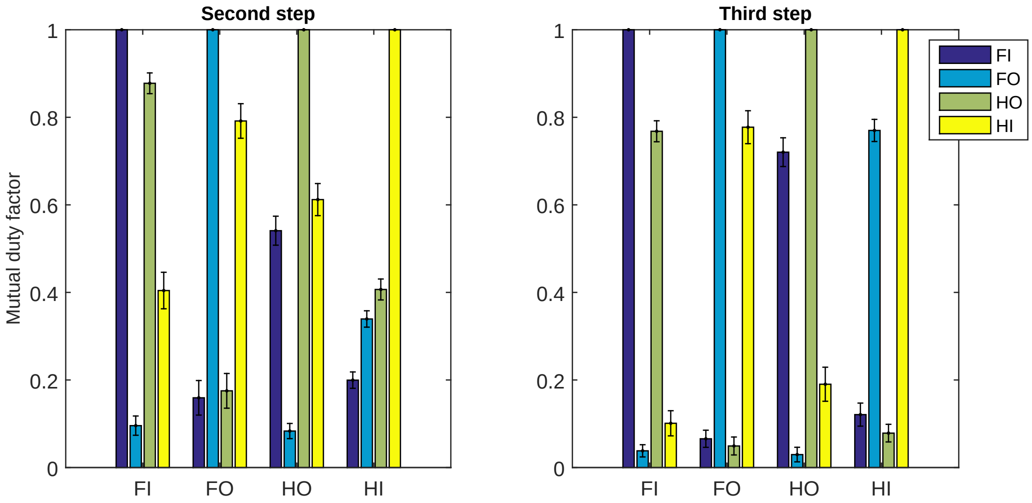

Figure 3.8: Mutual duty factor (the fraction of shared contact time for two limbs, mean ± one standard error) over the second and third steps (the first step is defined as starting with all limbs in contact); see Fig. 3.7). Each limb has 100% mutual duty factor with itself. Mutual duty factor in the third step was over 75% on average for trot pairs.

the end of the trial when animals neared steady running performance.

The discrepancy between individual trial forces and the averaged forces can be explained by two features of the agamas' behavior. First, observed forces/torques oscillated with time constants close to stepping frequency (much faster than the maneuver period); second, the phase of these fluctuations varied from trial to trial. As with the gait pattern, the variation in forces was not explained by constant shifts in phase or linear rescaling of time (e.g. by variations in stride frequency). We hypothesize instead that they are reflective of the high variation of contact timing and synchronicity, which itself may be a signature of active control.

While the averaged force/torque trajectories did not fully explain actual observed trajectories, they did reveal some shared behavior. The first stride featured the only period of sustained, high torques in the turning direction; thus angular momentum typically peaked in the first step (see Chapter 2, Fig. 2.4 for more details). Task-directed forces also peaked in the first step, although unlike torques, they continued to be positive in the transition and third steps. Both force and torque dipped significantly at the first-second stride transition, suggesting physical constraints due to the rest-to-run transition (in particular, all four limbs must lift off in relative time proximity). The presence of net task-direction forces in the first step (where essentially all angular impulse is generated) suggests that some turning performance is sacrificed for linear acceleration (since not all legs are positioned for positive Task Moment Arm, see Sec. 3.3.5).

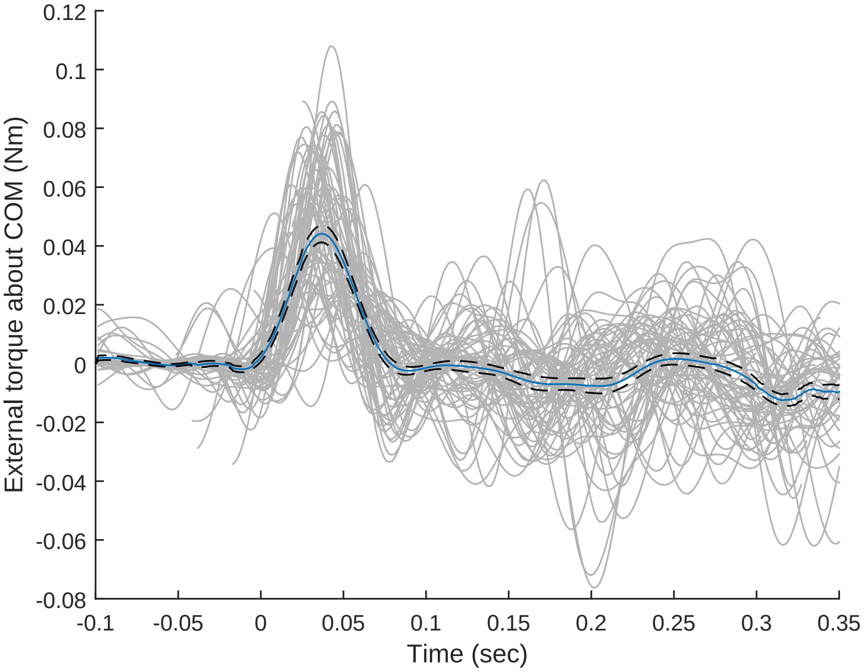

Figure 3.9: Task space torques. The mean time series accounts for 60% of observed variance in external torque.

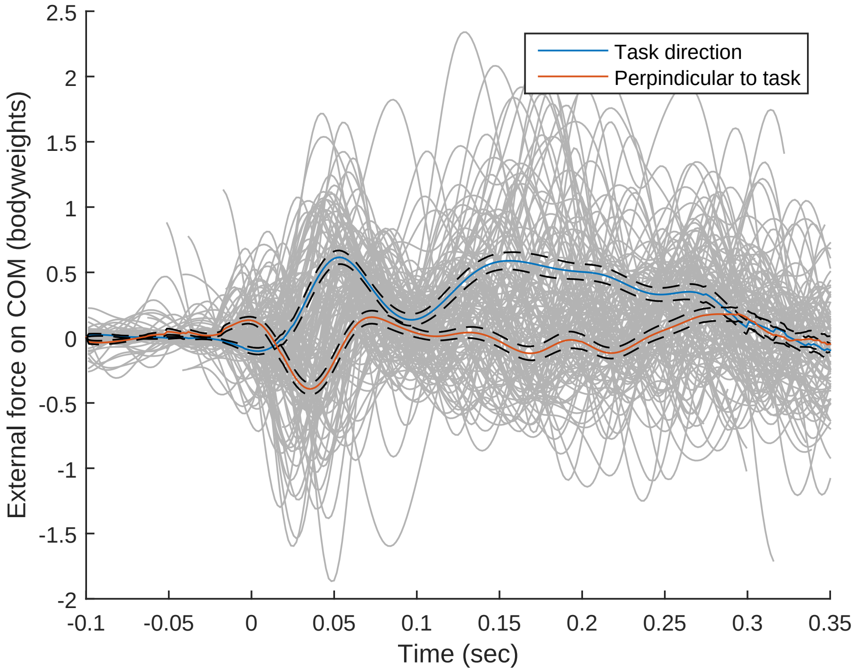

Figure 3.10: Task space forces. The mean time series accounts for 72% of observed variance in external force on the COM.

3.3.4 Function of individual limbs

We captured 98 single leg force events distributed across the four limbs, over the first three steps. Third step forces were both rare and generally insertions (see Sec. 3.3.2), so we limited analysis to the first two steps (63 and 30 events, respectively). The number of observed steps for each contact type is displayed in Fig. 3.11. To gauge the functional role of each limb during the observed steps, we numerically integrated over time to calculate its vertical impulse, angular impulse about the COM, and linear impulse in the direction of the prey. We averaged over all trials and normalized the impulse of each step by the maximum average impulse over all steps to generate a relative score of limb function, with zero being no impulse, and unity being the largest impulse measured for any foot in any step (Fig. 3.11). Vertical impulses were the most similar across limbs, with the highest impulse generated by the FO limb in the first stride and the HI limb in the second; these limbs also generated the highest positive (FO) and negative (HI) turning impulses. The largest linear impulses in the task direction were generated by the hind limbs in the second stride.

Each limb behaved differently, and most limbs changed roles from first to second stride. The front inside limb produced almost no task space maneuvering forces, but generated moderate support forces on both steps. The front outside limb generated the largest turning impulses in both steps and relatively small (but positive) linear acceleration in both steps. Both hind limbs saw similar function, with first steps generating moderate turning impulses and small positive (HI) or negative (HO) linear impulses. Both changed to a strongly propulsive role towards the target in the second stride. The hind limb functional shift from turning to linear acceleration gave the strongest hint of a functional tradeoff, especially given the large negative turning impulse in the second HI step.

Like limb kinematics and COM force/torque, limb impulses were subject to high variation on every step. Coefficients of variation were $50\% - 85\%$ for the significant turning impulses of the FO, HI, and HO first steps, and $20\% - 70\%$ for the linear impulses of the second steps. CVs for smaller (but significant) impulses were $100\% - 300\%$. Limbs that had high average impulses often had steps with no impulse, or impulse in the opposite direction.

To test the hypothesis that their sprawled posture gives agamas the ability to generate large forces in all directions, we examined the peak forces in the body frame for each limb over all steps and both inside and outside function (Fig. 3.12). Agamas exerted single leg forces anteriorly, posteriorly, and mediolaterally of up to one bodyweight. Hind limbs generated larger forces than forelimbs in the fore-aft axis, but all limbs generated similar medially-directed forces. Surprisingly, both front and hindlimbs also generated relatively large laterally-directed forces (e.g. the leg pulled the foot towards the midline, rather than pushing outwards) in addition to the medially-directed forces reported in steady running lizards (e.g. [92]). These pulling forces were largest when the hind limb was inside the turn, where they enabled the large task-direction linear impulses observed in Fig. 3.11, well before the animals' body heading aligned with the target direction.

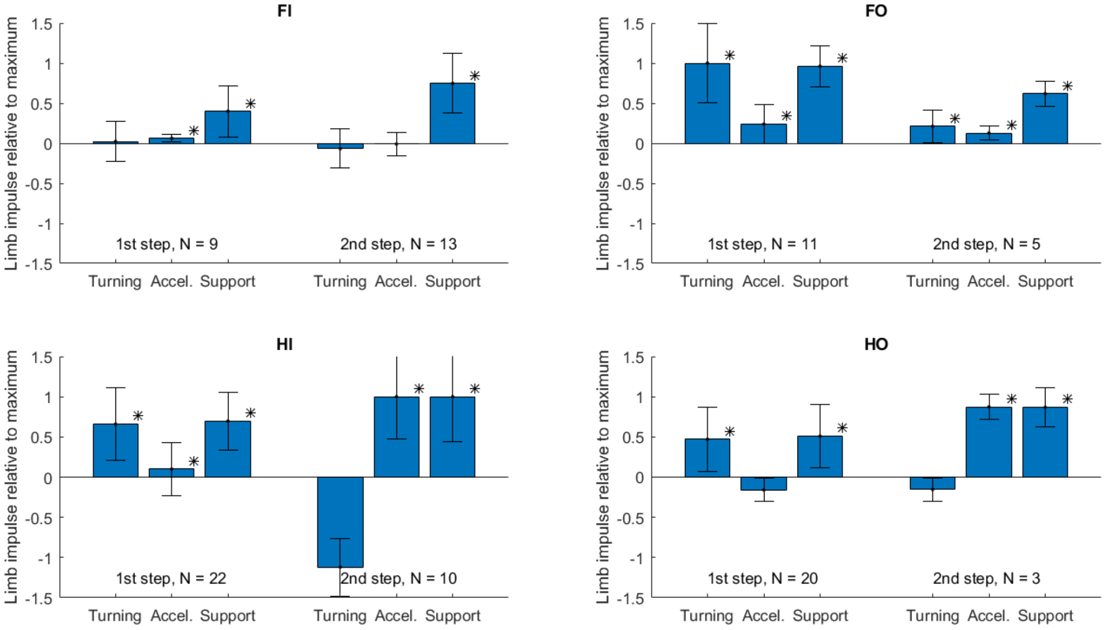

Figure 3.11: Relative limb function for each leg over the first and second steps. Error bars show variation in impulse (± one standard deviation). Impulses significantly greater than zero denoted by (*). The normalizations (maximum step impulses) for turning, acceleration, and support impulses were 0.72 $mN \cdot m \cdot s$, 25.6 $mN \cdot s$ and 31.5 $mN \cdot s$, respectively.

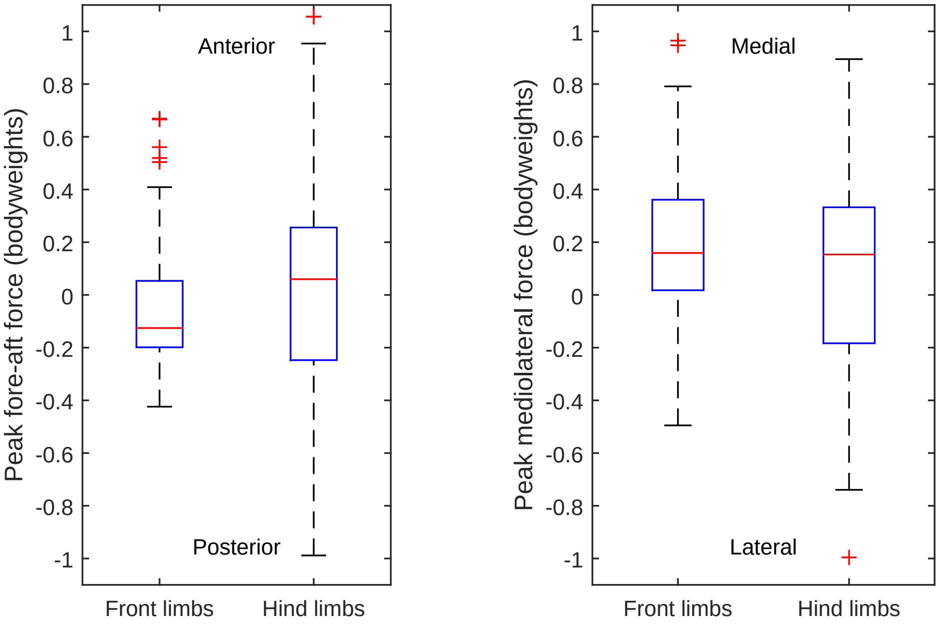

Figure 3.12: Peak ground reaction forces in body frame, along the fore-aft axis (left) and mediolateral axis (right). Labels indicate directions of positive and negative forces, e.g. positive mediolateral force is directed towards midline. Extent of box represents the 25th to 75th percentiles and whiskers represent most extreme values not considered outliers (red "+," defined as points outside of $\pm 2.7\sigma$) Hindlimbs generated larger fore-aft forces, but forelimbs generated largest lateral forces.

3.3.5 Moment arms and leg effectiveness

Limb geometry and posture, limb placement and body orientation with respect to task define a leg's ability to exert impulses that turn and accelerate the animal. Some touchdown positions may turn and accelerate in the task direction simultaneously, and others cannot. We examined the effect of these constraints on limb function by calculating the Task Moment Arm (TMA), the moment arm for a foot about the body COM of a unit force parallel to the prey target direction (i.e. the cross product of the vector from COM to foot at midstance with the unit task direction vector, plotted against orientation in Fig. 3.13). If agamas kept limb posture at mid-stance constant as they changed body orientation, then the moment arm of this force would vary as the sine of the body angle; deviations from a sine wave would reveal postural changes that modified moment arm. Limb positions with negative TMA force tradeoffs in limb function. Steps with positive TMA had positive correlation between linear and angular task impulses ($R = 0.58$ across all steps for all limbs), while steps with negative TMA had negative correlations ($R = -0.70$), indicating tradeoff between turning and linear impulse.

The hind outside limb had strongly negative moment arm during the first step, predicting the observed inverse relationship between rotational and linear task impulse (Fig. 3.11). The hind inside limb had the opposite relationship, but transitioned to negative moment arm in the second step, again predicting the tradeoff found in the second step for that limb. In both cases, the tradeoff revealed a strategic choice – preference for turning impulse in the first step and linear impulse in the second. It is especially interesting that the front outside limb was able to generate the largest turning forces while also generating some task-direction impulse, as its initial position should have forced a tradeoff given its position. The large body shape change observed in Chapter 1 may have allowed this limb to move into a synergistic posture earlier than a rigid body would have allowed.

3.3.6 Maneuvering with reduced traction

We collected 43 trials in which feet stepped on the reduced-traction surface and still met our trial inclusion guidelines. The mean trial experienced just over three perturbed steps, and slip lengths of 2.2 ± 0.2 *cm* on average (defined as the distance between touchdown and liftoff positions of the foot; see Sec. 2.3.3 for details and Fig 3.14 for an illustration). Unperturbed steps featured median slip distances of 0.38 *cm* (including digitization error and foot rotation). Feet slipped immediately upon touchdown on the low-traction surface and slipped without stopping over most of the limb's range of motion.

Despite numerous, apparently severe losses of foot traction (and therefore presumably large reductions in foot impulse), overall task performance was almost identical to that observed for unperturbed trials (Fig. 3.15). However, contact kinematics became even more variable – CVs for touchdown timing (see Sec. 3.3.2) were 55% and 39% for the inner and outer front limbs, and 60% and 29% for the inner and outer hind limbs, almost double the variance in unperturbed trials.

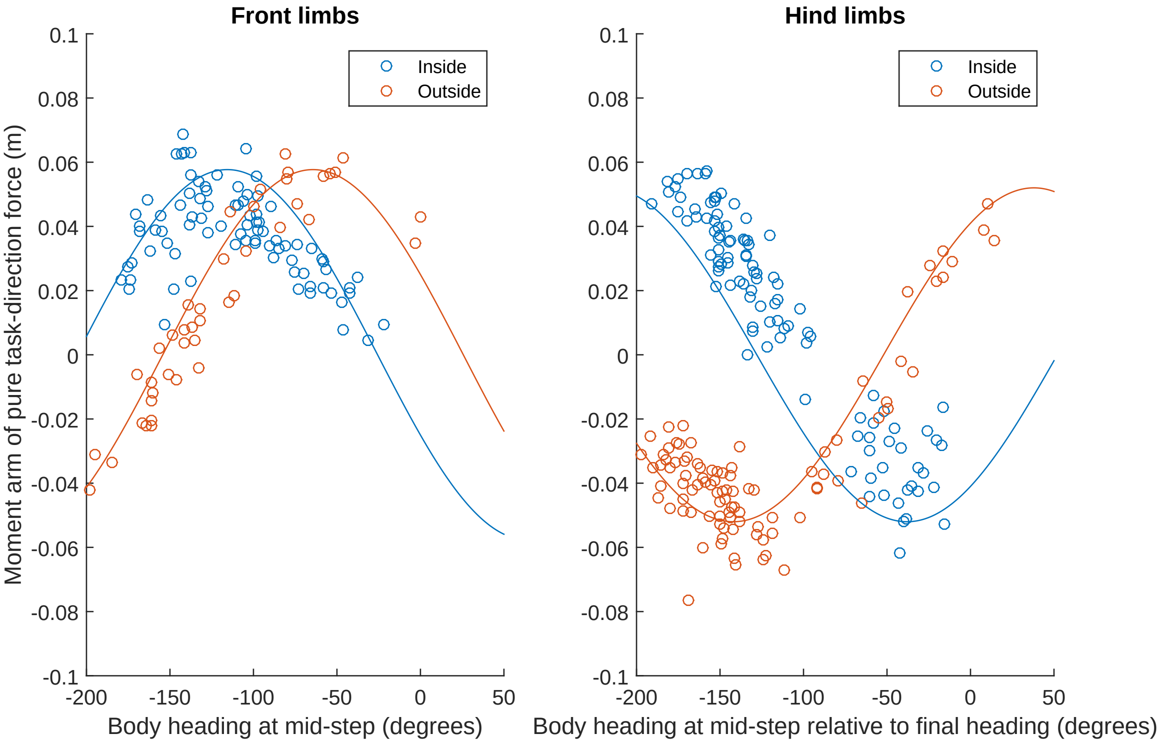

Figure 3.13: Moment arm of a unit force in the direction of final COM motion (TMA) plotted against body orientation midway through the step. Solid line represents prediction from rigid body using average posture. Negative values force tradeoffs between positive turning torque and target-oriented acceleration.

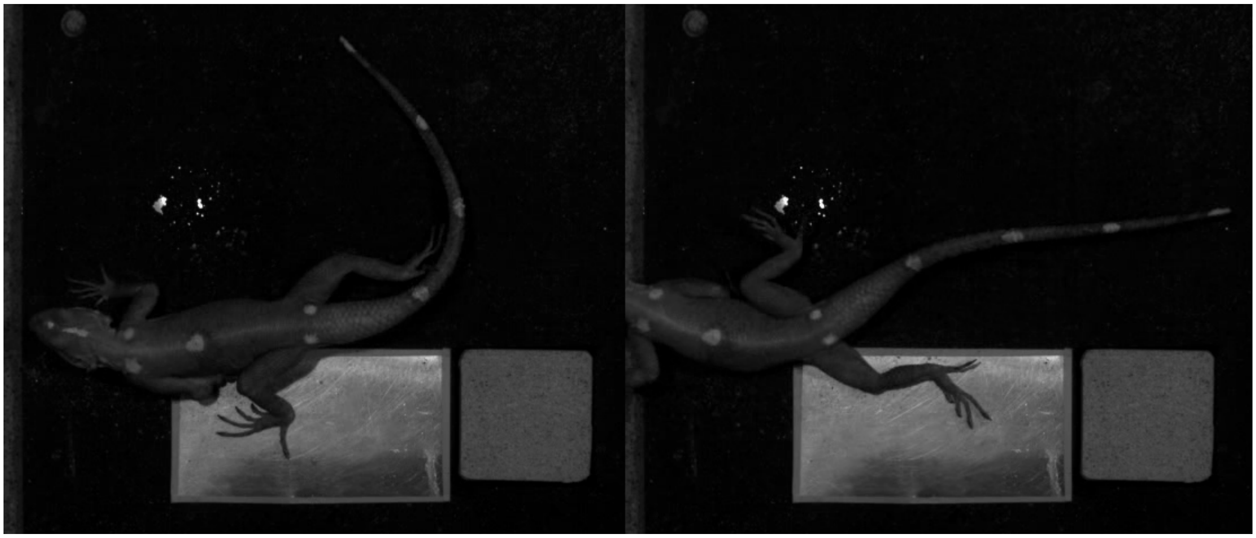

Figure 3.14: An agama experiencing a perturbation on the low-traction surface.

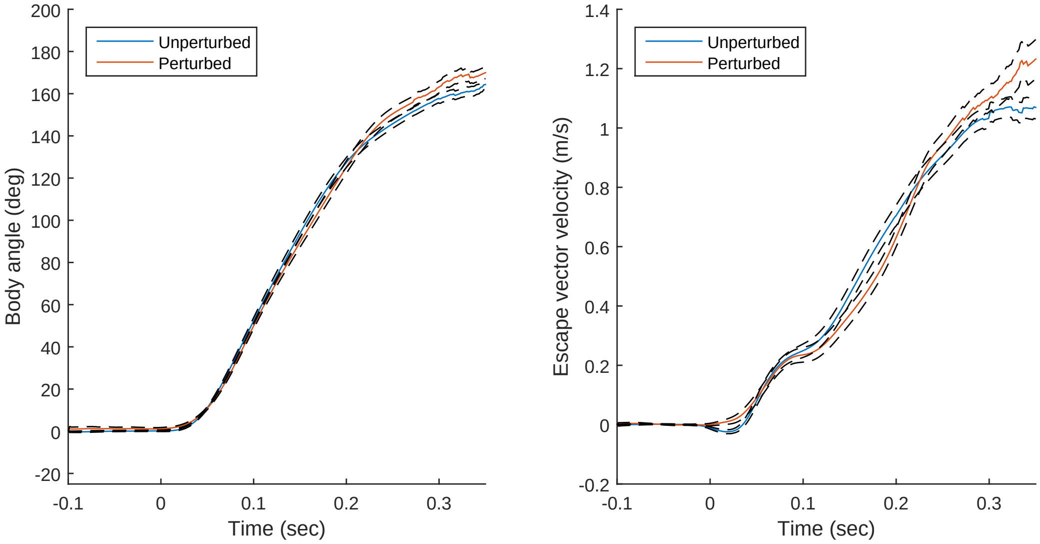

Figure 3.15: Robustness of task-space performance to traction perturbations. Differences in performance were small and typically insignificant (curves show means ± one SE).

3.4 Discussion

To our surprise, agamas performing a time-sensitive, high agility maneuver showed remarkable flexibility in gait and limb forces. While task-space behavior was fast and consistent, the average gait and COM force patterns were not representative of individual performances, which varied widely. Maneuvering agamas also defied our assumptions of the constraints on animals' planar maneuvers. Body heading mattered less than expected with respect to the lizards' ability to generate forces and maintain motion – agamas generated half of their goal-directed COM velocity while pointed in the wrong direction, and sustained lateral velocities of almost 0.4 m/s. We also found large planar forces that exerted large moments about joints (e.g. the force vector was not parallel to the limb). Limbs often "pulled" rather than pushed in the horizontal plane, even as they generated positive support (vertical ground reaction) force. While these forces (and particularly their variability) defied our expectations of constrained, near-optimal control, they may have aided robustness. Working in concert with the stabilizing effects of body/tail inertial forces due to shape change (see Chapter 2), these unusual locomotor features may explain how agamas maintained task performance in the presence of the large foot slips generated by our traction perturbation. Even during high-tempo, survival-critical behaviors like prey capture and escape, maintaining performance in the face of perturbations may be worth the sacrifice of all-out speed.

That sprawled posture has been associated with maneuverability [64, 92, 96] is intuitive – with limbs radiating outward from the body, these animals appear capable of directing forces in any direction simultaneously. However, this hypothesis is not yet strongly supported by empirical evidence; the parasagittal posture of mammals certainly does not preclude high maneuvering performance, and the evolution of the mammalian body form has even been hypothesized as an adaptation for agility [61]. Broad comparative studies are badly needed to establish whether such an advantage might actually exist. In this work, we found evidence that lizards are indeed capable of exerting large forces in all directions in the plane. Single-leg lateral forces and impulses were of similar magnitudes as fore-aft and vertical forces, and both fore and hind limbs generated comparable mediolateral forces (Fig. 3.12). To our surprise, we even found that medially-directed ("pulling") forces are common on the inside of the turn. Whole-body planar forces were typically up to around twice bodyweight, double the typical horizontal forces of steady-running lizards [92, 96]. Agamas did not typically use maneuvering forces that minimized joint moments when turning. Our results support the hypothesis that sprawled postures may increase maneuverability, and suggest that robots may benefit from the ability to generate large lateral forces.

While animals typically align their body heading to their COM velocity direction when running [62], we found that agamas experienced high lateral velocities throughout the maneuver. The angle of misalignment between heading and velocity exceeded 45° for the first 167 ms of the behavior on average, during which they achieved more than half of their peak COM velocity. Even the fastest turns we observed only reached 150° rotation during this time; if agamas had waited until their anterior axis pointed more into the direction of final movement, their acceleration would have been substantially delayed. Throughout this period, agamas maintained high body angular velocity – over 80% of peak, on average – so they continued to turn while dedicating motor output to accelerating towards their target. The ability of agamas to sustain lateral motion and generate large lateral forces may explain why turning impulse was largely limited to the first half step – once turning is initiated, effort can be directed to linear acceleration much earlier than if they had to complete the turn before accelerating. This strategy may help agamas negotiate the geometric tradeoffs that dominate turning strategy in bipeds [62], allowing the powerful hind limbs to switch from a turning function to a linear acceleration function as early as their second step (Fig. 3.11). Agamas also swing their tails to stabilize the trunk and delay the need for negative torques to stop the turn (Chapter 2), further freeing choice of leg function. By contrast, parasagittal runners (e.g. similarly-sized rodents [59, 63]) typically must roll their bodies [59] to generate large lateral forces (and presumably turning torques), thereby likely increasing tradeoffs between turning and linear acceleration. Agamas' ability to exert and sustain such a large misalignment between heading and course reduced the need to turn quickly, potentially mitigating the effects of their relatively large moment of inertia [61].

The high variability of limb contacts and ground reaction forces may be the signature of active sensorimotor control. In contrast to many fast locomotor behaviors, where feed-forward predictive control appears to dominate, and motor patterns remain constant in the face of perturbation [97], the limb kinematics and forces of turning agamas showed high variability. The insertions and deletions of steps that contributed to high variation in contact probability (Fig. 3.7) strongly suggest changes to the motor pattern. While the limb cycling frequencies might be high enough (above 6 Hz) to preclude within-stride control, stride-to-stride modification of steps is well within a reasonable sensorimotor bandwidth for animals of their size [71]. Stride-level control has been hypothesized as a critical stabilizer of running in humans, and may be present even in animals with high stepping frequencies such as cockroaches [98]. Despite high variation, we also found that the typical gait pattern of forward running (i.e. the trot) was largely preserved on average. Diagonal limb pairs had the highest mutual duty factor (Fig. 3.8), and the averaged gait diagram showed correlation of contact probability between these limbs. Rather than arising from loosely-coupled or decentralized feedback control [99], the agamas' gait appears modified from a clock-like architecture.

Literature on variability in the control of locomotion is relatively scarce. Coefficients of variation (CV) observed for kinematics during steady walking and running were low in humans [81] and horses [80] ($\leq 14\%$) and timing ($1-3\%$ of stride duration) from trial to trial. Ground reaction forces in human walking varied by less than 13% CV and as little as 3% [82]. Agamas performing planar maneuvers showed much higher CVs for kinematics (Sec. 3.3.2), particularly when negotiating traction perturbations (Sec. 3.3.6). Contrary to our expectations, we did not find high stereotypy resulting from mechanical or physiological constraints. Our results suggest that unsteady maneuvers simply may exhibit higher variability than expected based on steady running performance; rather than representing errors or anomalies, this variation may hold the key to understanding the control of legged maneuvering.

Somewhat paradoxically, high variability in contact timing and ground reaction forces produced highly robust task performance. Our attempt at probing limb function by perturbation utterly failed, as agamas maintained turning and acceleration performance regardless of the perturbed limb (Fig. 3.15). This robustness may be in part due to a feedforward change in strategy (e.g. agamas may sense the plate before movement and rework their turning strategy in anticipation), but even so, their ability to maintain performance with a lost contact opportunity is remarkable. A simple model of input-constrained time-optimal control would be highly sensitive to transient reduction of actuation. The mechanism by which agamas maintain performance remains a mystery for now, but ground reaction forces hint at one possibility: many steps do not provide task-level propulsion even in the absence of apparent perturbation (Sec. 3.3.4). These steps may be perturbed in ways that are imperceptible (tiny slips, low traction, motor noise), or due to high-dimensional posture changes that we did not discern. Alternatively, it simply may not be possible to exert maximal maneuvering forces in every step. Many observed steps provided vertical body support without turning or accelerating the body (Fig. 3.3.4); this is a critical function that could have catastrophic task performance consequences if not performed (e.g. the body crashes against the substrate generating substantial losses of momentum and/or energy). Limiting body pitch and roll is likely even more essential (as relatively small angle changes could result in impact of the head or complete inversion of the animal). These stability requirements place additional, high-dimensional limitations on ground reaction forces not captured by the TMA (Fig. 3.13), LEN [64], or other metrics of functional tradeoffs. Regardless of the origin of the high variance of ground reaction forces, we hypothesize that our perturbations were simply lost in the noise. Multi-legged animals have more opportunities to correct for perturbations. Consistent performance may thus arise from inconsistent forces when averaged over many contacts. The robustness provided by such a strategy may outweigh any loss of performance relative to a hypothetically time-optimal controller.

Chapter 4

Conclusion and Future Work

The work in this dissertation lays the foundation for a science of dynamic locomotion with an actuated body. Legged robots have long relied on rigid, boxy bodies and simple legs with few degrees of freedom. The nascent field of soft robotics [100, 101], while providing some exciting examples of the potential for flexible but tough frames and appendages, illustrates succinctly why the most agile and active machines still fit the older paradigm: soft robots are slow and difficult to control. Agility places high demands on actuation, which in turn requires structures capable of transmitting high loads across the body. Soft machines are intrinsically complex, with dynamics tending more towards continuum mechanics than rigid-body Newtonian physics; the natural dynamics of their compliant structures putatively replace the need for centralized control (i.e. Morphological Computation [102]), but thus far have sacrificed mobility for robustness. Soft machines take their inspiration from a diverse set of natural systems including cephalopod bodies and elephant trunks; this dissertation provides an alternative example of a flexible body, which may be more amenable to agile locomotion. Agile cursorial animals are not rigid boxes; the fastest land runner features an elongate, muscular spine [103] and rapid-running cockroaches have astonishingly deformable bodies [104]. The lizards that inspired Chapter 1 and performed the rapid maneuvers examined in Chapters 2 and 3 have features that could fit into either the rigid or soft mechanics paradigm.

4.1 Body flexibility and performance robustness

Performance robustness is an overarching theme of the maneuvers examined in this dissertation. The leaping and falling lizards that inspired the inertial reorientation template used their tails and spines to stabilize or recover from otherwise-catastrophic failures. Lateral flexibility is even greater than dorsoventral flexibility in many squamates, and it appears to give the agamas exquisite control authority in the horizontal plane over body posture and limb placement during terrestrial maneuvers as well as transient bouts of aerobatics (Chapter 2). The core actuation critical to these feats of agility allows lizards (and tailed robots) to trade away their reliance on external forces derived from interaction between distal actuators (i.e. limbs) and the notoriously messy, unpredictable environment in favor of inertial forces arising through internal body shape change. Inertial reorientation performance depends only on morphometric properties (Chapter 1), which should be constant or change over relatively long time scales (i.e. growth). However, dedication of actuator mass to core degrees of freedom need not rob a body of the ability to exert leg forces. The axial musculature has been implicated in ground reaction force production in taxa as diverse as lizards [105] and cats [103]. The caudofemoralis muscle is the dominant driver of lateral tail swings, but also the largest hindlimb power source [69]. Unlike the passive elastic structures of soft robots, the powerfully-actuated, flexible spines of animals may grant them the flexibility to move through complex environments without sacrificing the load-transmission advantages of a stiff body.

4.2 Design of bodies for maneuverability

The effects of shape change and inertial forces on lizard turning cast doubt on long-standing hypotheses of body design. The work presented in this dissertation suggests an urgent need for comparative performance studies across diverse body forms; we also provide a scaffold facilitating those studies, even across the animal-machine divide. The *operationalized* Templates and Anchors Framework (TAF) presented in Chapter 1 helps reveal the link between form and function by explicating the *Morphological Reduction* implicit when comparing diverse body plans engaged in the same physical behavior. This focus on parameter spaces helps show how diverse morphology embodies fundamental principles of locomotor behavior by writing down the relationships between physical properties of a real body (mass, length, inertia) and more abstract parameters that describe performance (e.g. inertial effectiveness). Importantly for comparative studies, this approach removes the need to simulate each body separately; investigators can simply measure morphometrics across a broad array of physical forms and use the morphological reduction to compare performance directly. Template-level parameters like inertial effectiveness may provide stronger phylogenetic characters and ecological correlates than direct morphometrics, which are subject to confounding tradespaces.

The TAF should not be limited to inertial reorientation; a host of other dynamic maneuvers should benefit from its application. The work in Chapters 2 and 3 raises several intriguing design questions that could be probed in the TAF. Anchoring a range of core- and/or distal-actuated models to the same locomotor template (e.g. the Single-Leg Inverted Pendulum (SLIP) [106]) could provide an apples-to-apples comparison of performance as total actuator power is shifted from spine to legs or vice-versa. Horizontal plane locomotion templates (e.g. variants of LLS [84]) with varying degrees of coupling between linear and rotational state sensitivity could anchor more detailed lizard models to test our hypotheses of the strategic tradeoffs displayed by agamas (i.e. turning forces limited to the first half stride, compromises towards early linear acceleration). The example of Chapter 1 anchored multiple bodies to the same template, but reducing a single anchor to multiple templates could expose tradeoffs with respect to different behaviors (e.g. the same multi-link body anchored to a running template vs. a turning template).

The results of these comparative TAF studies should work in concert with a new generation of physical robotic platforms. Whereas the low-DOF, spring-legged robotic paradigm exemplified in RHex and Velociroach was not conducive (e.g. [70]) to the sort of core-distal synergies found in maneuvering agamas, new machines with highly-backdrivable actuators may find more success. These machines might more readily benefit from active, lateral degrees of freedom analogous to the sprawling limbs of lizards. To our knowledge, the capability of the agamas for maintaining high lateral and angular velocities across several steps while simultaneously generating linear accelerations is unmatched in any robot. While several machines have directly explored the potential advantages of core actuation (notably [4]), no agile machine has explored lateral body actuation. Such a machine (particularly with lateral legged degrees of freedom) would be the ideal testbed to advance the hypotheses of inertial and impulsive force coordination and sprawled posture robustness raised in the second half of this dissertation.

The TAF provides a powerful platform for design insight across multiple body candidates for the same task. Just as the comparative method is one of the foundational methods for revealing operational principles in biology, we propose that a new field of comparative robotics could aid in design synthesis. Our examination of extant inertial reorientation designs generated a wealth of useful insights (see Chapter 1, Sec. 1.5). Equally ripe for exploration is the animal-machine divide, where runners feature not only different morphology but fundamentally different materials, actuators, and sensorimotor limitations. We speculate that a comparative science of animals and robots performing the same tasks could shed new light on the constraints and tradeoffs inherent to natural systems as well as help explain the persistent performance gap between animals and machines.

Bibliography

[1] T. Libby, T. Y. Moore, E. Chang-Siu, D. Li, D. J. Cohen, A. Jusufi, and R. J. Full, "Tail-assisted pitch control in lizards, robots and dinosaurs," *Nature*, vol. 481, no. 7380, pp. 181–184, 2012.

[2] E. Chang-Siu, T. Libby, M. Tomizuka, and R. J. Full, "A lizard-inspired active tail enables rapid maneuvers and dynamic stabilization in a terrestrial robot," in *IEEE/RSJ Int. Conf. Intelligent Robots and Systems*, San Fransisco, CA, USA, Sept. 2011.

[3] R. Altendorfer, N. Moore, H. Komsuoglu, M. Buehler, H. B. Brown Jr., D. McMordie, U. Saranli, R. Full, and D. E. Koditschek, "RHex: A biologically inspired hexapod runner," *Autonomous Robots*, vol. 11, no. 3, pp. 207–213, 2001.

[4] G. C. Haynes, J. Pusey, R. Knopf, A. M. Johnson, and D. E. Koditschek, "Laboratory on legs: an architecture for adjustable morphology with legged robots," in *Unmanned Systems Technology XIV*, vol. 8387, no. 1. SPIE, 2012, p. 83870W.

[5] T. Libby, A. M. Johnson, E. Chang-Siu, R. J. Full, and D. E. Koditschek, "Comparative design, scaling, and control of appendages for inertial reorientation," *IEEE Transactions on Robotics*, vol. PP, no. 99, pp. 1380–1398, 2016.

[6] A. M. Johnson, T. Libby, E. Chang-Siu, M. Tomizuka, R. J. Full, and D. E. Koditschek, "Tail assisted dynamic self righting," in *Int. Conf. Climbing and Walking Robots*, Baltimore, USA, July 2012, pp. 611–620.

[7] J. Zhao, T. Zhao, N. Xi, M. Mutka, and L. Xiao, "MSU Tailbot: Controlling aerial maneuver of a miniature-tailed jumping robot," *IEEE/ASME Trans. Mechatronics*, vol. PP, no. 99, pp. 1–12, 2015.

[8] N. Kohut, A. Pullin, D. Haldane, D. Zarrouk, and R. Fearing, "Precise dynamic turning of a 10 cm legged robot on a low friction surface using a tail," in *IEEE Int. Conf. Robotics and Automation*, 2013, pp. 3299–3306.

[9] C. Casarez, I. Penskiy, and S. Bergbreiter, "Using an inertial tail for rapid turns on a miniature legged robot," in *IEEE Int. Conf. Robotics and Automation*, 2013, pp. 5469–5474.

[10] A. Patel and M. Braae, “Rapid turning at high-speed: Inspirations from the cheetah’s tail,” in *IEEE/RSJ Int. Conf. Intelligent Robots and Systems*, 2013, pp. 5506–5511.

[11] R. Briggs, J. Lee, M. Haberland, and S. Kim, “Tails in biomimetic design: Analysis, simulation, and experiment,” in *IEEE/RSJ Int. Conf. Intelligent Robots and Systems*, 2012, pp. 1473–1480.

[12] J. Ackerman and J. Seipel, “Energy efficiency of legged robot locomotion with elastically suspended loads,” *IEEE Trans. Robotics*, vol. 29, no. 2, pp. 321–330, 2013.

[13] G.-H. Liu, H.-Y. Lin, H.-Y. Lin, S.-T. Chen, and P.-C. Lin, “A bio-inspired hopping kangaroo robot with an active tail,” *J. Bionic Engineering*, vol. 11, no. 4, pp. 541–555, 2014.

[14] M. Pijnappels, I. Kingma, D. Wezenberg, G. Reurink, and J. H. van Dieën, “Armed against falls: the contribution of arm movements to balance recovery after tripping,” *Experimental Brain Research*, vol. 201, no. 4, pp. 689–699, 2010.

[15] L. S. Crawford and S. S. Sastry, “Biological motor control approaches for a planar diver,” in *IEEE Conf. Decision and Control*, vol. 4, 1995, pp. 3881–3886.

[16] T. L. Hedrick, J. R. Usherwood, and a. a. Biewener, “Low speed maneuvering flight of the rose-breasted cockatoo (Eolophus roseicapillus). II. Inertial and aerodynamic reorientation.” *The Journal of experimental biology*, vol. 210, no. Pt 11, pp. 1912–1924, 2007.

[17] T. Kane and M. Scher, “A dynamical explanation of the falling cat phenomenon,” *Int. J. Solids and Structures*, vol. 5, no. 7, pp. 663–666, 1969.

[18] M. Brearley, “Motor cycle long jump,” *Mathematical Gazette*, pp. 167–171, 1981.

[19] A. Jusufi, D. I. Goldman, S. Revzen, and R. J. Full, “Active tails enhance arboreal acrobatics in geckos,” *Proc. National Academy of Sciences*, vol. 105, no. 11, pp. 4215–4219, 2008.

[20] A. Jusufi, D. T. Kawano, T. Libby, and R. J. Full, “Righting and turning in mid-air using appendage inertia: reptile tails, analytical models and bio-inspired robots,” *Bioinspiration & Biomimetics*, vol. 5, no. 4, p. 045001, 2010.

[21] G. J. Zeglin, “Uniroo–a one legged dynamic hopping robot,” B.S. Thesis, Massachusetts Institute of Technology, 1991.

[22] K. Autumn, M. Buehler, M. Cutkosky, R. Fearing, R. J. Full, D. Goldman, R. Groff, W. Provancher, A. A. Rizzi, U. Saranli *et al.*, “Robotics in scansorial environments,” in *SPIE Defense and Security*, 2005, pp. 291–302.

[23] S. Kim, A. T. Asbeck, M. R. Cutkosky, and W. R. Provancher, “SpinybotII: climbing hard walls with compliant microspines,” in *IEEE Int. Conf. Advanced Robotics*, 2005, pp. 601–606.

[24] R. Balasubramanian, A. Rizzi, and M. T. Mason, “Legless locomotion: A novel locomotion technique for legged robots,” *Int. J. Robotics Research*, vol. 27, no. 5, pp. 575–594, May 2008.

[25] A. Demir, M. M. Ankarali, J. P. Dyhr, K. A. Morgansen, T. L. Daniel, and N. J. Cowan, “Inertial redirection of thrust forces for flight stabilization,” in *Int. Conf. Climbing and Walking Robots*, Baltimore, USA, July 2012.

[26] A. De and D. E. Koditschek, “The Penn Jerboa: A platform for exploring parallel composition of templates,” Tech. Rep., Feb 2015, arXiv:1502.05347.

[27] S. W. Heim, M. Ajallooeian, P. Eckert, M. Vespignani, and A. Ijspeert, “On designing an active tail for body-pitch control in legged robots via decoupling of control objectives,” in *Int. Conf. Climbing and Walking Robots*, Hangzhou, China, September 2015.

[28] A. Crespi, K. Karakasiliotis, A. Guignard, and A. J. Ijspeert, “Salamandra robotica II: An amphibious robot to study salamander-like swimming and walking gaits,” *IEEE Trans. Robotics*, vol. 29, no. 2, pp. 308–320, 2013.

[29] M. Estrada, E. W. Hawkes, D. L. Christensen, and M. R. Cutkosky, “Perching and vertical climbing: Design of a multimodal robot,” in *IEEE Int. Conf. Robotics and Automation*, 2014, pp. 4215–4221.

[30] C. Kessens and C. T. Lennon, “Robotic uses of tails: Self-righting,” in *Robotics: Science and Systems Workshop on “Robotic Uses for Tails”*, Rome, Italy, July 2015.

[31] A. Jusufi, Y. Zeng, R. J. Full, and R. Dudley, “Aerial righting reflexes in flightless animals,” *Integrative and Comparative Biology*, vol. 51, no. 6, pp. 937–943, 2011.

[32] A. Patel and E. Boje, “On the conical motion and aerodynamics of the cheetah tail,” in *Robotics: Science and Systems Workshop on “Robotic Uses for Tails”*, Rome, Italy, July 2015.

[33] E. Chang-Siu, T. Libby, M. Brown, R. Full, and M. Tomizuka, “A nonlinear feedback controller for aerial self-righting by a tailed robot,” in *IEEE Int. Conf. Robotics and Automation*, May 2013, pp. 32–39.

[34] A. M. Johnson and D. E. Koditschek, “Legged self-manipulation,” *IEEE Access*, vol. 1, pp. 310–334, May 2013.

[35] J. P. Dyhr, N. J. Cowan, D. J. Colmenares, K. Morgansen, T. L. Daniel *et al.*, “Autostabilizing airframe articulation: Animal inspired air vehicle control,” in *IEEE Conf. Decision and Control*, 2012, pp. 3715–3720.

[36] M. M. Porter, D. Adriaens, R. L. Hatton, M. A. Meyers, and J. McKittrick, "Why the seahorse tail is square," *Science*, vol. 349, no. 6243, 2015.

[37] B. Grossi, J. Iriarte-Díaz, O. Larach, M. Canals, and R. A. Vásquez, "Walking like dinosaurs: Chickens with artificial tails provide clues about non-avian theropod locomotion," *PloS one*, vol. 9, no. 2, p. e88458, 2014.

[38] R. Full and D. Koditschek, "Templates and anchors: neuromechanical hypotheses of legged locomotion on land," *J. Experimental Biology*, vol. 202, no. 23, pp. 3325–3332, 1999.

[39] A. Rizzi and D. Koditschek, *Further progress in robot juggling: solvable mirror laws*. IEEE Comput. Soc. Press, 1994, pp. 2935–2940.

[40] J. Nakanishi, T. Fukuda, and D. E. Koditschek, "A brachiating robot controller," *IEEE Trans. Robotics and Automation*, vol. 16, no. 2, pp. 109–123, 2000.

[41] T. Libby, A. M. Johnson, E. Chang-Siu, R. J. Full, and D. E. Koditschek, "Technical report on: Comparative desing, scaling, and control of appendages for inertial reorientation," University of Pennsylvania, Tech. Rep., 2015. [Online]. Available: http://kodlab.seas.upenn.edu/Aaron/TailsTR

[42] R. L. Hatton and H. Choset, "Geometric motion planning: The local connection, stokes' theorem, and the importance of coordinate choice," *Int. J. Robotics Research*, vol. 30, no. 8, pp. 988–1014, 2011.

[43] P. Gregorio, M. Ahmadi, and M. Buehler, "Design, control, and energetics of an electrically actuated legged robot," *IEEE Trans. Systems, Man, and Cybernetics, Part B*, vol. 27, no. 4, pp. 626–634, 1997.

[44] B. Hannaford and J. Winters, "Actuator properties and movement control: biological and technological models," in *Multiple Muscle Systems*. Springer, 1990, pp. 101–120.

[45] J. E. Bobrow, S. Dubowsky, and J. Gibson, "Time-optimal control of robotic manipulators along specified paths," *Int. J. Robotics Research*, vol. 4, no. 3, pp. 3–17, 1985.

[46] M. Tarkiainen and Z. Shiller, "Time optimal motions of manipulators with actuator dynamics," in *IEEE Int. Conf. Robotics and Automation*, 1993, pp. 725–730.

[47] V. G. Rao and D. S. Bernstein, "Naive control of the double integrator," *IEEE Control Systems*, vol. 21, no. 5, pp. 86–97, 2001.

[48] T. W. Mather and M. Yim, "Modular configuration design for a controlled fall," in *IEEE/RSJ Int. Conf. Intelligent Robots and Systems*, St. Louis, USA, Oct. 2009.

[49] Y. Umetani and K. Yoshida, “Resolved motion rate control of space manipulators with generalized jacobian matrix,” *IEEE Trans. Robotics and Automation*, vol. 5, no. 3, pp. 303–314, 1989.

[50] S. Seok, A. Wang, M. Y. Chuah, D. Otten, J. Lang, and S. Kim, “Design principles for highly efficient quadrupeds and implementation on the mit cheetah robot,” in *IEEE Int. Conf. Robotics and Automation*, 2013, pp. 3307–3312.

[51] T. Blackburn and K. Gaston, “Animal body size distributions: patterns, mechanisms and implications,” *Trends in Ecology & Evolution*, vol. 9, no. 12, pp. 471–474, 1994.

[52] R. Alexander and A. Jayes, “A dynamic similarity hypothesis for the gaits of quadrupedal mammals,” *J. Zoology*, vol. 201, no. 1, pp. 135–152, 1983.

[53] A. M. Johnson, “Gait design using self–manipulation,” in *Robotics: Science and Systems Workshop on “Dynamic Locomotion”*, Berkeley, CA, July 2014.

[54] R. Altendorfer, D. E. Koditschek, and P. Holmes, “Stability analysis of legged locomotion models by symmetry-factored return maps,” *Int. J. Robotics Research*, vol. 23, no. 10–11, pp. 979–999, 2004.

[55] J. W. Wilson, M. G. Mills, R. P. Wilson, G. Peters, M. E. Mills, J. R. Speakman, S. M. Durant, N. C. Bennett, N. J. Marks, and M. Scantlebury, “Cheetahs, Acinonyx jubatus, balance turn capacity with pace when chasing prey,” *Biology Letters*, vol. 9, no. 5, p. 20130620, 2013. [Online]. Available: http://dx.doi.org/10.1098/rsbl.2013.0620{%}5Cnhttp://rsbl.royalsocietypublishing.org.{%}5Cnhttp://www.ncbi.nlm.nih.gov/pubmed/24004493

[56] A. Hedenstrom and M. Rosen, “Predator versus prey: on aerial hunting and escape strategies in birds,” *Behavioral Ecology*, vol. 12, no. 2, pp. 150–156, 2001. [Online]. Available: http://beheco.oxfordjournals.org/content/12/2/150.short

[57] P. W. Webb, “Fast-start Performance and Body Form in Seven Species of Teleost Fish,” *Journal of Experimental Biology*, vol. 74, no. 1, pp. 211–226, 1978. [Online]. Available: http://jeb.biologists.org/content/74/1/211.short

[58] A. J. Wirsing, K. E. Cameron, and M. R. Heithaus, “Spatial responses to predators vary with prey escape mode,” *Animal Behaviour*, vol. 79, no. 3, pp. 531–537, 2010.

[59] A. R. Lammers and K. M. Sufka, “Turning the Corner in Quadrupedal Arboreal Locomotion: Kinetics of Changing Direction While Running in the Siberian Chipmunk (Tamias sibiricus),” *Journal of Experimental Zoology Part A: Ecological Genetics and Physiology*, vol. 319, no. 2, pp. 99–112, 2013.

[60] T. E. Higham, M. S. Davenport, and B. C. Jayne, "Maneuvering in an arboreal habitat: the effects of turning angle on the locomotion of three sympatric ecomorphs of Anolis lizards," *J Exp Biol*, vol. 204, no. 23, pp. 4141–4155, 2001. [Online]. Available: http://jeb.biologists.org/cgi/content/abstract/204/23/4141

[61] R. M. Walter and D. R. Carrier, "Scaling of rotational inertia in murine rodents and two species of lizard," *Journal of Experimental Biology*, vol. 205, no. 14, pp. 2135–2141, 2002.

[62] D. L. Jindrich and M. Qiao, "Maneuvers during legged locomotion." *Chaos (Woodbury, N.Y.)*, vol. 19, no. 2, p. 026105, jun 2009. [Online]. Available: http://www.ncbi.nlm.nih.gov/pubmed/19566265

[63] R. M. Walter, "Kinematics of 90 degrees running turns in wild mice." *The Journal of experimental biology*, vol. 206, no. Pt 10, pp. 1739–1749, may 2003. [Online]. Available: http://jeb.biologists.org/cgi/doi/10.1242/jeb.00349

[64] D. Jindrich and R. Full, "Many-legged maneuverability: dynamics of turning in hexapods," *The Journal of Experimental Biology*, vol. 202, pp. 1603–1623, 1999. [Online]. Available: http://www.ncbi.nlm.nih.gov/pubmed/10333507

[65] J. A. Walker, C. M. Breder, P. Domenici, R. W. Blake, P. Domenici, R. W. Blake, C. L. Gerstner, H. C. Howland, U. Norberg, J. M. V. Rayner, J. E. Randall, A. J. Schrank, P. W. Webb, S. Mayberry, D. A. Thompson, and J. C. Tyler, "Does a rigid body limit maneuverability?" *The Journal of experimental biology*, vol. 203, no. Pt 22, pp. 3391–6, 2000. [Online]. Available: http://www.ncbi.nlm.nih.gov/pubmed/11044378

[66] B. Cheng, B. W. Tobalske, D. R. Powers, T. L. Hedrick, S. M. Wethington, G. T. C. Chiu, and X. Deng, "Flight mechanics and control of escape manoeuvres in hummingbirds I. Flight kinematics." *Journal of Experimental Biology*, pp. 3518–3531, 2016.

[67] D. R. Carrier, R. M. Walter, and D. V. Lee, "Influence of rotational inertia on turning performance of theropod dinosaurs: clues from humans with increased rotational inertia," *Journal of Experimental Biology*, vol. 204, no. 22, pp. 3917–3926, 2001.

[68] M. A. Daley, A. Voloshina, and A. A. Biewener, "The role of intrinsic muscle mechanics in the neuromuscular control of stable running in the guinea fowl." *The Journal of physiology*, vol. 587, no. Pt 11, pp. 2693–707, jun 2009. [Online]. Available: http://www.pubmedcentral.nih.gov/articlerender.fcgi?artid=2714031{&}tool=pmcentrez{&}rendertype=abstract

[69] F. E. Nelson and B. C. Jayne, "The effects of speed on the in vivo activity and length of a limb muscle during the locomotion of the iguanian lizard Dipsosaurus dorsalis," *Journal of Experimental Biology*, vol. 204, no. 20, pp. 3507–3522, 2001.

[70] A. O. Pullin, N. J. Kohut, D. Zarrouk, and R. S. Fearing, “Dynamic turning of 13 cm robot comparing tail and differential drive,” *Proceedings - IEEE International Conference on Robotics and Automation*, pp. 5086–5093, 2012.

[71] H. L. More, J. R. Hutchinson, D. F. Collins, D. J. Weber, S. K. H. Aung, and J. M. Donelan, “Scaling of sensorimotor control in terrestrial mammals.” *Proceedings. Biological sciences / The Royal Society*, vol. 277, no. 1700, pp. 3563–8, 2010. [Online]. Available: http://rspb.royalsocietypublishing.org/content/277/1700/3563.abstract

[72] H. Knuesel, H. Geyer, and A. Seyfarth, “Influence of swing leg movement on running stability.” *Human movement science*, vol. 24, no. 4, pp. 532–43, aug 2005. [Online]. Available: http://www.ncbi.nlm.nih.gov/pubmed/16213046

[73] Y.-H. Kwon, “Body segment parameter equations,” 1998. [Online]. Available: http://www.kwon3d.com/theory/bspeq/bspeq.html{#}es

[74] D. M. Henderson, “Estimating the masses and centers of mass of extinct animals by 3-D mathematical slicing,” *Paleobiology*, vol. 25, no. 1, pp. 88–106, 1999.

[75] J. J. Dowling, J. L. Durkin, and D. M. Andrews, “The uncertainty of the pendulum method for the determination of the moment of inertia,” *Medical Engineering \& Physics*, vol. 28, no. 8, pp. 837–841, 2006. [Online]. Available: http://www.sciencedirect.com/science/article/B6T9K-4J440F5-1/2/386aaea3cbbab9bf4554d263dc4b5043

[76] M. Hara, A. Shibayama, D. Takeshita, and S. Fukashiro, “The effect of arm swing on lower extremities in vertical jumping.” *Journal of biomechanics*, vol. 39, no. 13, pp. 2503–11, jan 2006. [Online]. Available: http://www.ncbi.nlm.nih.gov/pubmed/16168998

[77] S. Revzen and J. Guckenheimer, “Estimating the phase of synchronized oscillators,” *Physical Review E*, vol. 78, no. 5, p. 051907, nov 2008. [Online]. Available: http://link.aps.org/doi/10.1103/PhysRevE.78.051907

[78] K. Nishikawa, A. a. Biewener, P. Aerts, A. N. Ahn, H. J. Chiel, M. a. Daley, T. L. Daniel, R. J. Full, M. E. Hale, T. L. Hedrick, a. K. Lappin, T. R. Nichols, R. D. Quinn, R. a. Satterlie, and B. Szymik, “Neuromechanics: An integrative approach for understanding motor control,” *Integrative and Comparative Biology*, vol. 47, no. 1, pp. 16–54, 2007.

[79] C. Li, T. Zhang, and D. I. Goldman, “A Terradynamics of Legged Locomotion on Granular Media,” *Science*, vol. 339, no. 6126, pp. 1408–1412, 2013. [Online]. Available: http://www.sciencemag.org/content/339/6126/1408{%}5Cnhttp://www.sciencemag.org/content/339/6126/1408.full.pdf

[80] M. Faber, C. Johnston, P. R. van Weeren, and A. Barneveld, “Repeatability of back kinematics in horses during treadmill locomotion.” *Equine veterinary journal*, vol. 34, pp. 235–241, 2002.

[81] J. B. Dingwell, J. P. Cusumano, P. R. Cavanagh, and D. Sternad, “Local Dynamic Stability Versus Kinematic Variability of Continuous Overground and Treadmill Walking,” *Journal of Biomechanical Engineering*, vol. 123, no. 1, p. 27, 2001. [Online]. Available: http://www.ncbi.nlm.nih.gov/pubmed/11277298{%}5Cnhttp://biomechanical.asmedigitalcollection.asme.org/article.aspx?articleid=1404775

[82] K. Masani, M. Kouzaki, and T. Fukunaga, “Variability of ground reaction forces during treadmill walking.” *Journal of Applied Physiology*, vol. 92, no. 5, pp. 1885–90, 2002.

[83] T. M. Kubow, “The role of the mechanical system in control: a hypothesis of self-stabilization in hexapedal runners,” *Philosophical Transactions of the Royal Society B: Biological Sciences*, vol. 354, pp. 849–861, 1999.

[84] J. Proctor and P. Holmes, “Steering by transient destabilization in piecewise-holonomic models of legged locomotion,” *Regular and Chaotic Dynamics*, vol. 13, no. 4, pp. 267–282, 2008. [Online]. Available: http://dx.doi.org/10.1134/S1560354708040047

[85] M. Raibert, “Legged Robots,” *Communications of the ACM*, vol. 29, no. 6, pp. 499–514, 1986. [Online]. Available: http://doi.acm.org/10.1145/5948.5950

[86] K. L. Hoffman and R. J. Wood, “Turning gaits and optimal undulatory gaits for a modular centipede-inspired millirobot,” *2012 4th IEEE RAS & EMBS International Conference on Biomedical Robotics and Biomechatronics (BioRob)*, pp. 1052–1059, jun 2012. [Online]. Available: http://ieeexplore.ieee.org/lpdocs/epic03/wrapper.htm?arnumber=6290288

[87] K. C. Galloway, G. C. Haynes, B. D. Ilhan, A. M. Johnson, R. Knopf, G. Lynch, B. Plotnick, M. White, and D. E. Koditschek, “X-RHex: A highly mobile hexapedal robot for sensorimotor tasks,” University of Pennsylvania, Tech. Rep., 2010.

[88] D. L. Jindrich, T. F. Besier, and D. G. Lloyd, “A hypothesis for the function of braking forces during running turns.” *Journal of biomechanics*, vol. 39, no. 9, pp. 1611–20, jan 2006. [Online]. Available: http://www.ncbi.nlm.nih.gov/pubmed/16038914

[89] K. Hase and R. B. Stein, “Turning strategies during human walking.” *Journal of neurophysiology*, vol. 81, no. 6, pp. 2914–2922, 1999.

[90] J. Nakanishi, R. Cory, M. Mistry, J. Peters, and S. Schaal, “Operational Space Control: A Theoretical and Empirical Comparison,” *The International Journal of Robotics Research*, vol. 27, no. 6, pp. 737 –757, 2008. [Online]. Available: http://ijr.sagepub.com/content/27/6/737.abstract{%}5Cnhttp://ijr.sagepub.com/content/27/6/737.full.pdf

[91] A. A. Biewener, “Biomechanics of mammalian terrestrial locomotion.” *Science (New York, N.Y.)*, vol. 250, no. 4984, pp. 1097–1103, 1990.

[92] J. J. Chen, a. M. Peattie, K. Autumn, and R. J. Full, “Differential leg function in a sprawled-posture quadrupedal trotter.” *The Journal of experimental biology*, vol. 209, no. Pt 2, pp. 249–59, jan 2006. [Online]. Available: http://www.ncbi.nlm.nih.gov/pubmed/16391347

[93] P. Aerts, R. Van Damme, K. D’Août, B. Van Hooydonck, R. V. Damme, K. D. Aou, and B. V. Hooydonck, “Bipedalism in lizards: whole-body modelling reveals a possible spandrel.” *Philosophical transactions of the Royal Society of London. Series B, Biological sciences*, vol. 358, no. 1437, pp. 1525–33, sep 2003. [Online]. Available: http://www.pubmedcentral.nih.gov/articlerender.fcgi?artid=1693243{&}tool=pmcentrez{&}rendertype=abstract

[94] D. V. Lee, J. E. A. Bertram, and R. J. Todhunter, “Acceleration and balance in trotting dogs.” *The Journal of experimental biology*, vol. 202, no. Pt 24, pp. 3565–3573, 1999.

[95] H.-M. Maus, S. Revzen, J. Guckenheimer, C. Ludwig, J. Reger, and A. Seyfarth, “Constructing predictive models of human running,” *Journal of the Royal Society Interface*, vol. 12, no. 103, p. 20140899, 2015. [Online]. Available: http://dx.doi.org/10.1098/rsif.2014.0899

[96] E. J. McElroy, R. Wilson, A. R. Biknevicius, and S. M. Reilly, “A comparative study of single-leg ground reaction forces in running lizards.” *The Journal of experimental biology*, vol. 217, no. Pt 5, pp. 735–42, mar 2014. [Online]. Available: http://www.ncbi.nlm.nih.gov/pubmed/24198262

[97] S. Sponberg and R. J. Full, “Neuromechanical response of musculo-skeletal structures in cockroaches during rapid running on rough terrain.” *The Journal of experimental biology*, vol. 211, no. Pt 3, pp. 433–46, feb 2008. [Online]. Available: http://www.ncbi.nlm.nih.gov/pubmed/18203999

[98] S. Revzen, S. a. Burden, T. Y. Moore, J.-M. Mongeau, and R. J. Full, “Instantaneous kinematic phase reflects neuromechanical response to lateral perturbations of running cockroaches.” *Biological cybernetics*, vol. 107, no. 2, pp. 179–200, apr 2013. [Online]. Available: http://www.ncbi.nlm.nih.gov/pubmed/23371006

[99] H. Cruse, T. Kindermann, M. Schumm, J. Dean, and J. Schmitz, “Walknet - A biologically inspired network to control six-legged walking,” pp. 1435–1447, 1998. [Online]. Available: http://www.sciencedirect.com/science/article/pii/S0893608098000677

[100] C. Majidi, “Soft Robotics : A Perspective – Current Trends and Prospects for the Future,” vol. 1, no. 1, 2014.

[101] D. Trivedi, C. D. Rahn, W. M. Kier, and I. D. Walker, “Soft robotics: Biological inspiration, state of the art, and future research,” *Applied Bionics and Biomechanics*, vol. 5, no. 3, pp. 99–117, 2008.

[102] H. Hauser, A. J. Ijspeert, R. M. Füchslin, R. Pfeifer, and W. Maass, "Towards a theoretical foundation for morphological computation with compliant bodies." *Biological cybernetics*, no. 2011, pp. 355–370, jan 2012. [Online]. Available: http://www.ncbi.nlm.nih.gov/pubmed/22290137

[103] B. M. Boszczyk, A. A. Boszczyk, and R. Putz, "Comparative and functional anatomy of the mammalian lumbar spine." *The Anatomical record*, vol. 264, no. 2, pp. 157–68, oct 2001. [Online]. Available: http://www.ncbi.nlm.nih.gov/pubmed/11590593

[104] K. Jayaram and R. J. Full, "Cockroaches traverse crevices, crawl rapidly in confined spaces, and inspire a soft, legged robot," *Proceedings of the National Academy of Sciences*, vol. 113, no. 8, pp. 1–8, 2016. [Online]. Available: http://www.pnas.org/lookup/doi/10.1073/pnas.1514591113{%}5Cnhttp://www.pnas.org/cgi/doi/10.1073/pnas.0912427107

[105] D. Ritter, "Axial muscle function during lizard locomotion," *The Journal of experimental biology*, vol. 199, no. Pt 11, pp. 2499–510, jan 1996. [Online]. Available: http://www.ncbi.nlm.nih.gov/pubmed/9320426

[106] D. V. Lee and S. G. Meek, "Directionally compliant legs influence the intrinsic pitch behaviour of a trotting quadruped." *Proceedings. Biological sciences / The Royal Society*, vol. 272, no. March, pp. 567–572, 2005.